β-Catenin Phosphorylation Dynamics in Differentiating Human Pluripotent Stem Cells

By

Amritava Das

A dissertation submitted in partial fulfillment of

the requirements for the degree of

Doctor of Philosophy

(Chemical Engineering)

at the

UNIVERSITY OF WISCONSIN-MADISON

2015

Date of final oral examination: 6/29/2015

This dissertation is submitted to the following members of the Final Oral Committee

Sean P. Palecek, Professor, Chemical and Biological Engineering
Eric V. Shusta, Professor, Chemical and Biological Engineering
Jennifer L. Reed, Associate Professor, Chemical and Biological Engineering
Brian F. Pfleger, Associate Professor, Chemical and Biological Engineering
Susan Thibeault, Associate Professor, Surgery

β-Catenin Phosphorylation Dynamics in Differentiating Human Pluripotent Stem Cells

Amritava Das

Under the supervision of Professor Sean P. Palecek

At the University of Wisconsin-Madison

Abstract

Human pluripotent stem cells (hPSCs) were utilized to gain insight into the Wnt pathway, a developmentally important signaling pathway and to generate vocal fold epithelia, a hard to derive tissue for *in vitro* barrier characterization studies. Additionally, phenotypic changes occurring within epithelial cancer cells on culture on a superhydrophobic surface were characterized.

hPSCs treated with a Wnt agonist (CHIR) differentiated into mesendodermal precursors completely within 50 hours of treatment, but primarily between 20 and 30 hours of treatment. Significant differences in the levels of phosphorylated β-catenin were observed throughout the differentiation process. PKA phosphorylated β-catenin increased significantly after 20 hours of CHIR treatment and was spatially and temporally correlated with Brachyury expression. Inhibition of PKA along with CHIR led to the attenuation of Brachyury expression. These insights

were used to develop a new layout for the Wnt pathway focused on site-specific β-catenin phosphorylation. A mathematical framework for this differentiation was also developed.

Vocal fold epithelial barrier characterization has historically been difficult due to the limited viability of *ex vivo* tissue. Previous hPSC derived tissues were unable to create a confluent cell layer for the accurate characterization of barrier properties. To address these challenges a vocal fold epithelia differentiation protocol was developed for the scalable differentiation on Transwell® inserts and for barrier characterization. The trans-epithelial electrical resistance of the differentiated tissue observed on these inserts was 2556 ± 126 Ω cm^2 and the minimum permeability of Sodium Fluorescein through the differentiated tissue was 8.14 ± 1.95 nm/s. The electrical resistance of 4.5 cm^2 and 1.12 cm^2 inserts were statistically insignificant from each other (p-value=0.83), indicating the scalability of the protocol.

It was observed that epithelial cancer cells grown on a water resistant superhydrophobic substrate were up to 80% viable at high densities. Cells grown on this substrate for 12 hours or longer did not adhere to polystyrene unlike cells grown on adherent surfaces or surfaces functionalized to have low cellular attachment. This phenotypic change was also observed with cells grown on a shaken superhydrophobic surface.

Acknowledgements

As I spend my birthday collating data for this document, I've had a chance to reflect and realize that these past few years have been deeply satisfying. There are a lot of people to thank for that, and I am sure that many will not be listed in this acknowledgement section. To being with I would like to thank my committee for their time and consideration to go through my work. I've had the opportunity of interacting with them in various meetings through the years and I've learned tremendously from each one. Prof. Shusta through Friday lab sub-group meetings, Prof. Pfleger served on my preliminary examination committee, Prof. Reed served during my fifth year update talk and Prof. Thibeault for allowing me to work on a very fun project. I like talking, so vocal cord work seems completely in place.

Through these years I have had fantastic collaborators outside of the lab. Uttam Manna, thank you for pushing me to get data on our project. Ciara Leydon and Vlasta Lungova for enlightening discussions on vocal fold epithelia and histology. The staff of WiCell in particular Marybeth, Jennie and Steve for being forgiving a very large number of times for late core order submissions.

The undergraduate students that I have had an opportunity to work with and get to know have allowed me to enjoy life outside the lab. In purely reverse chronological order Michaela Rekow and Adam Mischler for help through the semesters for doing a majority of my Western blots. Amy Zhao, Luis Rivera-Hiraldo and Adriana Rodriguez for working with me through the summers and being as independent as they were.

The Palecek lab has been a phenomenal workplace courtesy the amazing labmates. Samira Azarin, thank you for correcting my prelim and offering me a post-doc once I defend. Chet and Josh for getting me interested in football. Lance and Alicia for kind words and support. Laurie for the amazing thank you brownies. I also would like to mention Scott Canfield, Namrata Ram and Matt Stebbins for discussions, and Xiaoping and Kaitlin for their company.

Speaking of people in the Palecek lab, thank you Sean. I came to this campus to work on viscoelastic fluids, but decided to work on stem cell related stuff once we met to discuss courses. The amount of freedom that I've had these past years has been truly incredible and would not have been enjoyable had it not been for your patience. I also want to thank Sean for showing me what true impartiality looks like – regardless of research progress, I've never seen favoritism from him. It is one his qualities that I hope to emulate over time.

Prof Linda Hogle and Kris Saha for their infinite patience in listening to my crazy ideas and for their mentorship and guidance.

I want to acknowledge family and friends in Madison. Roommates past and present, Jayneel Gandhi, Kushal Sinha and Vikram Adhikarla and other chemical engineers who have been down this path, Abhijeet Joshi, Rishabh Jain and Andres Merchan, thank you for your help and company.

Finally, I want to thank my parents, Kaveri and Goutam Das for their support, guidance, and reality checks through graduate school.

Contents

Acknowledgements iv
List of Figures ix
List of Tables xiv
List of Equations xvi
1 Introduction 1
1.1 Outline of the thesis 6
1.2 References 7
2 Modulation of Wnt induced human pluripotent stem cell differentiation by Protein Kinase A 11
2.1 Introduction 11
2.1.1 Human Pluripotent Stem Cells 11
2.1.2 Maintenance of hPSC pluripotency 13
2.1.3 Differentiation of hPSCs 14
2.1.4 The Wnt pathway 15
2.1.5 Site-specific phosphorylation of β-catenin 16
2.1.6 Wnt signaling in hPSC regulation 17
2.1.7 Aim of the current study 19
2.2 Results 20
2.2.1 GSK3 inhibition leads to differentiation of hPSCs in 50 hours 20
2.2.2 Levels of β-catenin upon CHIR treatment 23
2.2.3 Destruction complex dynamics change throughout differentiation 24
2.2.4 Transcriptionally active β-catenin dynamics show differences 25
2.2.5 Phospho-Ser675 β-catenin is correlated to differentiating cells 27
2.2.6 PKA inhibition reduces Brachyury and total β-catenin levels 27
2.2.7 PKA inhibition reduces transcriptionally active β-catenin 29
2.2.8 PKA inhibition attenuates differentiation 29
2.2.9 Mechanism proposed to explain trends 30
2.2.10 Mathematical modeling of hPSC Wnt differentiation 31
2.3 Conclusion 36
2.3.1 Qualitative improvement of the study 37
2.3.2 Quantitative improvement of the study 38

2.4 Materials and methods 39
2.4.1 hPSC culture and differentiation 39
2.4.2 Immunostaining 39
2.4.3 Flow Cytometry 40
2.4.4 Western Blotting 40
2.4.5 Figures 41
2.5 Tables 62
2.6 Equations 70
2.7 References 73
3 Vocal Fold Epithelia Differentiation on Transwell® Inserts 80
3.1 Introduction 80
3.1.1 Vocal Fold Epithelial Tissue 80
3.1.2 Vocal Fold Epithelial Differentiation 82
3.1.3 Aim of the current study 84
3.2 Results 85
3.2.1 Stepwise differentiation scheme adapted from collagen-matrix system 85
3.2.2 Initial Seeding Density 86
3.2.3 Porosity 87
3.2.4 Insert Material 87
3.2.5 Scalability 87
3.2.6 Histology 88
3.2.7 Barrier Permeability 88
3.3 Conclusions and Future directions 88
3.4 Materials and Methods 90
3.4.1 hPSC Maintenance and differentiation 90
3.4.2 Barrier Electrical Resistance Measurement 91
3.4.3 Barrier permeability measurement 91
3.5 Figures 93
3.6 References 100
4 Phenotypic changes in cells cultured on a superhydrophobic surface 104
4.1 Introduction 104
4.1.1 Interplay between surface topography and cellular behavior 104
4.1.2 Generation of superhydrophobic surfaces 105

4.1.3 Cell culture on superhydrophobic surfaces 106
4.1.4 Aim of the current study 108
4.2 Results 108
4.2.1 Serum content affects the superhydrophobicity of the PVDMA/PEI substrate 108
4.2.2 Viability 109
4.2.3 Morphology 110
4.2.4 Replating behavior 110
4.3 Discussion 112
4.4 Conclusion 113
4.5 Material and Methods 114
4.5.1 Substrate manufacture 114
4.5.2 Cell Culture 115
4.5.3 Viability measurements 116
4.5.4 Immunostaining 116
4.6 Figures 117
4.7 References 129
5 Conclusions 133
5.1 Summary of findings 133
5.2 Future Recommendations 137
5.2.1 Wnt and Protein Kinase A interaction 137
5.2.2 Vocal fold epithelia differentiation on Transwell® inserts 141
5.2.3 Cell culture on superhydrophobic surfaces 142
5.3 Conclusions 143
5.4 Equations 144
5.5 References 145

List of Figures

Figure 2.1: Schematic showing the variety of sources for hPSCs [78]..... 41

Figure 2.2: Waddington's epigenetic hypothesis. The green ball is a more multipotent state than the blue ball, which has already rolled down the epigenetic landscape to form somatic tissue. It is unlikely that the blue ball will roll up and back down to occupy any of the other slots at the bottom of the landscape [22]. 42

Figure 2.3: A schematic of the canonical Wnt pathway in its off and on state, adapted from Logan and Nusse [25]. 43

Figure 2.4: Schematic showing the terminal fates of Brachyury positive mesendodermal progenitors indicating the important role of Wnt signaling in development and differentiation[4]. 44

Figure 2.5: Immunostaining showing the differentiation of hPSCs on the addition of 2 µM of CHIR to cells in E8 over 0 hours, 30 hours and 50 hours. There is beginning Brachyury expression at 30 hours, along with residual Nanog expression, however this disappears in the next 20 hours. Left panel indicates Hoechst staining of DNA, middle panel indicates Brachyury, stained with Alexa-488 and right panel indicates Nanog stained with Alexa-594. Scale bar is 25 µm..... 45

Figure 2.6: Immunostaining image showing cells 20 hours after addition of CHIR, (A) without CHIR and (B) with CHIR and 30 hours after addition of CHIR (C) without CHIR, and (D) with CHIR. Hoechst staining of DNA, middle panel indicates Brachyury, stained with Alexa-488 and right panel indicates Nanog stained with Alexa-594. Scale bar is 25 µm. 46

Figure 2.7: Flow cytometric analysis showing that the differentiation to Brachyury occurs uniformly and not sporadically, the entire population of cells migrates from a Brachyury negative to a Brachyury positive state. Similar changes are not observed for the –CHIR conditions. Brachyury-Alexa-633:FL4 is on the vertical axis. 47

Figure 2.8: Flow cytometric analysis showing percentage of cells that are either Nanog positive or Brachyury positive over time during the CHIR treatment duration..... 48

Figure 2.9: Western blotting data for Brachyury (A) and Nanog (B) during 50 hours with CHIR (gray) and without CHIR(black). n=3..... 49

Figure 2.10: Panel showing western blotting quantification for total β-catenin throughout the differentiation process. n=3..... 50

Figure 2.11: Panels showing the quantified amount of (A) Phospho-Ser33/Ser37/Thr41 β-catenin and (B) Phospho-Thr41/Ser45 β-catenin throughout 50 hours of culture and differentiation. N=3 51

Figure 2.12: Panels showing western blotting data for (A) Phospho-Ser675 β-catenin and (B) Phospho-Ser552 β-catenin over 50 hours of differentiation. n=3 52

Figure 2.13: Colocalization of Phospho-Ser675 β-catenin and Brachyury in samples (A) treated with CHIR for 30 hours. Control (B) DMSO treatment have limited Phospho-Ser675 β-catenin expression, only in areas of high density. Scale bar is 100 µm. 53

Figure 2.14: Western blotting results on treatment of cells with CHIR and PKA inhibitors for (A) Brachyury and (B) β-catenin 54

Figure 2.15: Western blotting results on treatment of cells with CHIR and PKA inhibitors for (A) Phospho-Ser552 β-catenin and (B) Phospho-Ser675-β-catenin 55

Figure 2.16: Immunostaining results showing cells 30 hours after the addition of KT5720, with and without CHIR. In both cases Brachyury is not seen and many of the cells are Nanog positive. Scale bar is 100 µm. 56

Figure 2.17: Schematic created highlighting the mechanism proposed to explain the results discovered 57

Figure 2.18: Reaction scheme created in CellDesigner to model the mechanism of Wnt signaling in hPSCs 58

Figure 2.19: Parameter fit results for Nanog and total β-catenin for the DMSO control condition 59

Figure 2.20: Parameter estimation fitting for Phospho-Thr41/Ser45 β-catenin and Phospho-Ser33/Ser37/Thr41 β-catenin for the DMSO control condition 60

Figure 2.21: Parameter estimation fitting for Phospho-Ser675 β-catenin and Phospho-Ser552 β-catenin for the DMSO control condition 61

Figure 3.1: A diagram showing the challenges of performing barrier studies with the collagen gel system. When the gel is seeded on the apical side, it covers the entire apical surface. On further growth of the fibroblasts in the gel, it contracts into a roughly trapezoidal shape exposing gaps on the surface of the insert. Ions and dyes may thus flow freely in the apical and baso-lateral side disrupting barrier measurements. 93

Figure 3.2: Schematic showing the differentiation scheme, based on the collagen gel scheme. Instead of performing RA treatment and then subculturing on a collagen-fibroblast gel, in this scheme, the RA differentiated cells are simply transferred over the vocal fold fibroblasts. The remaining steps of FAD for 2 days following the rise to the air liquid interface remains the same. 94

Figure 3.3: Transepithelial electrical resistance expressed in Ω cm^2 for cultures in which (A) 50k cells/cm^2 were seeded and (B) 100k cells/cm^2 were seeded and expanded for 4 days. The mean TEER is higher for the denser seeding condition. 95

Figure 3.4: Transepithelial electrical resistance expressed in Ω cm^2 for cultures in which (A)3 µm pore size inserts were used and (B) 0.4 µm pore size inserts were used. The mean TEER is higher for the larger pore size condition. 96

Figure 3.5: Transepithelial electrical resistance expressed in Ω cm^2 for cultures in which (A) polycarbonate 3 µm pore size inserts were used and (B) polyester 3 µm pore size inserts were used. The mean TEER is higher for the polycarbonate condition. 97

Figure 3.6: Transepithelial electrical resistance expressed in Ω cm2 for cultures in which (A) 1.2 cm diameter (12 well plate) polycarbonate 3 µm pore size inserts were used and (B) 4.5 cm diameter (6 well plate) polycarbonate 3 µm pore size inserts were used. The mean TEER are very similar indicating scalability. 98

Figure 3.7: Histology and hematoxylin and eosin staining for cells differentiated on 3 µm pore size polycarbonate insert, after stratification for 14 days. Scale bar is 200 µm. 99

Figure 4.1: (A) Structures of branched poly(ethyleneimine) (PEI) and the azlactone-containing polymer poly(2-vinly-4,4-dimethyl azlactone)(PVMDA) used for the covalent/reactive assembly of the polymer multilayers in this study. (B) Reaction of the azlactone ring of PVDMA with primary amine functionality results in the formation of an amide/amide-type linkage. (C) Schematic showing functionalization of an azlactone-containing PEI/PVDMA film by post-fabrication treatment with a primary amine-containing nucleophile. Adapted from Broderick and Manna et al[16]. 117

Figure 4.2: Droplets maintained for 24 hours at high humidity at 37 °C. Top droplet is DMEM + 1% FBS, while bottom droplet is DMEM + 10% FBS. The top droplet shows the spherical property expected from aqueous droplets on a superhydrophobic surface, while the bottom droplet shows degradation of the superhydrophobicity of the substrate..... 118

Figure 4.3: Bar graphs showing the viability of MCF-7 cells suspended on (A) superhydrophobic surfaces and (B) low attachment surfaces for 12 hours without shaking. 119

Figure 4.4: Bar graphs showing the viability of MCF-7 cells suspended on (A) superhydrophobic surfaces and (B) low attachment surfaces for 24 hours without shaking. 120

Figure 4.5: Bar graphs showing the viability of MCF-7 cells suspended on (A) superhydrophobic surfaces and (B) low attachment surfaces for 48 hours without shaking. 121

Figure 4.6: Bar graphs showing the viability of MCF-7 cells suspended on (A) superhydrophobic surfaces and (B) low attachment surfaces for 24 hours while being shaken at 130 rpm. 122

Figure 4.7: Phalloidin-Alexa 594 stained cells grown on (A) superhydrophobic surface and (B) low attachment surface for 24 hours, showing diffuse actin presentation and a lack of stress fibres. Cells in panel (C) were cultured on adherent tissue culture polystyrene and show distinct stress fibres and localized actin. Nuclei indicated in blue, phalloidin in red, scale bars are 50 µm..... 123

Figure 4.8: Schematic showing the setup of the replating experiments. Cells are maintained both on superhydrophobic surfaces and low attachment surfaces for 6, 12 or 24 hours, followed by replating onto polystyrene for 24 hours after which images are taken and replating characteristics are studied 124

Figure 4.9: Images showing adherent cells after 24 hours of growth on polystyrene surfaces (A) before and (B) after removal of media showing the adherence of cells on the surface. Scale bar is 250 µm. 125

Figure 4.10: Images showing cells after 24 hours of culture on tissue culture polystyrene following 6 hours of treatment on superhydrophobic surfaces with shaking at 130 rpm with media (A) and (B) after media removal. (C) & (D) are on superhydrophobic surface without shaking, (E) & (F) are on low attachment surfaces with shaking at 130 rpm and (G) and (H) are on low attachment surfaces without shaking. Scale bar is 250 µm. 126

Figure 4.11: Images showing cells after 24 hours of culture on tissue culture polystyrene following 12 hours of treatment on superhydrophobic surfaces with shaking at 130 rpm with media (A) and (B) after media removal. (C) & (D) are on superhydrophobic surface without shaking, (E) & (F) are on low attachment surfaces with shaking at 130 rpm and (G) and (H) are on low attachment surfaces without shaking. Scale bar is 250 µm. 127

Figure 4.12: Images showing cells after 24 hours of culture on tissue culture polystyrene following 12 hours of treatment on superhydrophobic surfaces with shaking at 130 rpm with media (A) and (B) after media removal. (C) & (D) are on superhydrophobic surface without shaking, (E) & (F)

are on low attachment surfaces with shaking at 130 rpm and (G) and (H) are on low attachment surfaces without shaking. Scale bar is 250 μm. 128

List of Tables

Table 1: Results of two-way ANOVA test of Brachyury western blotting values between CHIR treated conditions and DMSO treated conditions for each time point 62

Table 2: Results of two-way ANOVA test of Brachyury western blotting values between CHIR treated conditions across different time points. The column and row title indicate the time points being compared 62

Table 3: Results of two-way ANOVA test of Nanog western blotting values between CHIR treated conditions and DMSO treated conditions for each time point 62

Table 4: Results of two-way ANOVA test of Nanog western blotting values between DMSO treated conditions across different time points. The column and row title indicate the time points being compared 63

Table 5: Results of two-way ANOVA test of Nanog western blotting values between CHIR treated conditions across different time points. The column and row title indicate the time points being compared 63

Table 6: Results of two-way ANOVA test of β-Catenin western blotting values between CHIR treated conditions and DMSO treated conditions for each time point 63

Table 7: Results of two-way ANOVA test of β-Catenin western blotting values between DMSO treated conditions across different time points. The column and row title indicate the time points being compared 64

Table 8: Results of two-way ANOVA test of β-Catenin western blotting values between CHIR treated conditions across different time points. The column and row title indicate the time points being compared 64

Table 9: Results of two-way ANOVA test of Phospho-β-Catenin Thr41/Ser45 western blotting values between CHIR treated conditions and DMSO treated conditions for each time point 64

Table 10: Results of two-way ANOVA test of Phospho-β-Catenin Thr41/Ser45 western blotting values between DMSO treated conditions across different time points. The column and row title indicate the time points being compared..... 65

Table 11: Results of two-way ANOVA test of Phospho-β-Catenin Thr41/Ser45 western blotting values between CHIR treated conditions across different time points. The column and row title indicate the time points being compared..... 65

Table 12: Results of two-way ANOVA test of Phospho-β-Catenin Ser33/Ser37/Thr41 western blotting values between CHIR treated conditions and DMSO treated conditions for each time point 65

Table 13: Results of two-way ANOVA test of Phospho-β-Catenin Ser33/Ser37/Thr41 western blotting values between DMSO treated conditions across different time points. The column and row title indicate the time points being compared 66

Table 14: Results of two-way ANOVA test of Phospho-β-Catenin Ser33/Ser37/Thr41 western blotting values between CHIR treated conditions across different time points. The column and row title indicate the time points being compared 66

Table 15: Results of two-way ANOVA test of Phospho-β-Catenin Ser675 western blotting values between CHIR treated conditions and DMSO treated conditions for each time point 66

Table 16: Results of two-way ANOVA test of Phospho-β-Catenin Ser675 western blotting values between DMSO treated conditions across different time points. The column and row title indicate the time points being compared 67

Table 17: Results of two-way ANOVA test of Phospho-β-Catenin Ser675 western blotting values between CHIR treated conditions across different time points. The column and row title indicate the time points being compared 67

Table 18: Results of two-way ANOVA test of Phospho-β-Catenin Ser552 western blotting values between CHIR treated conditions and DMSO treated conditions for each time point 67

Table 19: Results of two-way ANOVA test of Phospho-β-Catenin Ser552 western blotting values between DMSO treated conditions across different time points. The column and row title indicate the time points being compared 68

Table 20: Results of two-way ANOVA test of Phospho-β-Catenin Ser552 western blotting values between CHIR treated conditions across different time points. The column and row title indicate the time points being compared 68

Table 21: Parameters used for initial run for the Wnt signaling pathway in hPSC model 69

List of Equations

Equation 1: Michealis-Menten reaction equation 70

Equation 2: Change in K_m with inhibitor added 70

Equation 3: Calculation of K_i from IC50 using expression by Brandt et al[79] 70

Equation 4: Equation for reaction re1 indicating the zeroth order synthesis of β-catenin 70

Equation 5: Equation for reaction re2, indicating the phosphorylation of β-catenin at Thr41/Ser45 by CK1α. $V_{CK1\alpha}$ and $K_{CK1\alpha}$, are the maximum velocity and Michaelis Menten constant for CK1α, the species s2 represents β-catenin 70

Equation 6: Equation for reaction re3, indicating the phosphorylation of β-catenin at Ser33/Ser37/Thr41 by GSK3β. $V_{GSK3\beta}$ and $K_{GSK3\beta}$, are the maximum velocity and Michaelis Menten constant for GSK3β, the species s8 represents Phospho-β-catenin Thr41/Ser45 70

Equation 7: Equation for re4, the first order ubiquitination and destruction of Phospho-β-catenin Ser33/Ser37/Thr41, the species s11 represents Phospho-β-catenin Ser33/Ser37/Thr41 71

Equation 8: Equation for re5, the formation of Phospho-β-catenin Ser552 through phosphorylation of β-catenin by both Akt and PKA. V_{PKA} and K_{PKA}, are the maximum velocity and Michaelis Menten constant for PKA, V_{Akt} and K_{Akt}, are the maximum velocity and Michaelis Menten constant for Akt, and the term x_{PKA} represents the proportion of PKA phosophorylated β-catenin phosphorylated at Ser675 71

Equation 9: Equation for re6, the formation of Phospho-β-catenin Ser552 through phosphorylation of β-catenin by both Akt and PKA. V_{PKA} and K_{PKA}, are the maximum velocity and Michaelis Menten constant for PKA. The term x_{PKA} represents the proportion of PKA phosophorylated β-catenin phosphorylated at Ser675. 71

Equation 10: Equation for re7, the transcription of Brachyury through the action of Phospho-β-catenin Ser675. The species s14 represents Phospho-β-catenin Ser675 71

Equation 11: Equation for re11, the transcription of Nanog through the action of Phospho-β-catenin Ser675. The species s14 represents Phospho-β-catenin Ser675 72

Equation 12: Equation for re10, the transcription of Brachyury through the action of Phospho-β-catenin Ser552. The species s13 represents Phospho-β-catenin Ser552 72

Equation 13: Equation for re12, the transcription of Nanog through the action of Phospho-β-catenin Ser552. The species s13 represents Phospho-β-catenin Ser552 72

Equation 14: Equation for re13, representing the destruction of Brachyury. The species s15 represents Brachyury 72

Equation 15: Equation for re15 representing the zeroth order synthesis of Nanog 72

Equation 16: Equation for re14, representing the destruction of Nanog. The species s16 represents Nanog 72

Equation 17: Equation for re4, the first order ubiquitination and destruction of Phospho-β-catenin Ser33/Ser37/Thr41, the species s11 represents Phospho-β-catenin Ser33/Ser37/Thr41 144

Equation 18: Equation for re4, the first order ubiquitination and destruction of Phospho-β-catenin Ser33/Ser37/Thr41, the species s11 represents Phospho-β-catenin Ser33/Ser37/Thr41, modified by the density dependent term with $k_{4\rho}$ indicating the density dependent rate constant, and ρ and ρ_0 representing current and initial density respectively 144

1 Introduction

The advent of embryonic stem cell technology, first in mice in 1981[1], and later in human systems [2] opened up new areas for research. Embryonic stem cell lines are developed through the harvest of the inner cell mass of the blastocyst followed by culture in controlled conditions. The fertilized egg or zygote, starts division soon after formation, to form a structure called the morula, which is a densely packed ball consisting of about 100 cells. The cells in the morula further divide into the trophectoderm, a hollow spherical layer of cells and the inner cell mass. The trophectoderm forms extra-embryonic tissue like the placenta, while the inner cell mass, post implantation forms the human body. Embryonic stem cell lines are derivatives of the inner cell mass, and are capable of differentiating into any cell type in the human body and unlimited self-renewal *in vitro* [3]. They are maintained in the pluripotent state (defined as being capable of forming any cell type in the human body) through the use of specific media and extracellular matrix [4-7].

Once the inner cell mass is extracted, the blastocyst from which it came from no longer remains viable for implantation and cannot be carried out to term. This imbues human embryonic stem research with several ethical challenges [8-10]. Further investigation into the mechanisms regarding the maintenance of pluripotency led to the development of embryonic stem cell like cells (that are pluripotent) from autologous (non-embryonic) sources, and do not involve the destruction of the embryo. These cells are called human induced pluripotent stem cells[11]. These cells along with human embryonic stem cells are classified as human pluripotent stem cells (hPSCs).

hPSCs can be differentiated *in vitro* into many therapeutically relevant cell types by mimicking chemical cues and certain mechanical cues present during *in vivo* development[12]. Typically hPSC derived therapy for regenerative medicine is suggested for certain slow growing or non-proliferative tissues like heart muscle or cells of the nervous system [13, 14]. However, lately hPSCs have been used as model systems to study development [15] and their pluripotency can be harnessed to study tissues that are hard to access, like the blood brain barrier [16]. Harnessing the potential of hPSC technology, however requires the understanding of *in vivo* development.

After the formation of the inner cell mass and trophectoderm, the blastocyst begins the process of implantation. The trophectoderm begins implanting onto the uterine wall, and the inner cell mass begins to form a disc like structure called the blastula. The blastula has three layers, which eventually differentiate from each other forming three types of tissue, the outer ectoderm, the inner endoderm and the mesoderm sandwiched between the ectoderm and endoderm. The ectoderm gives rise to derivatives of the skin and the nervous system, the endoderm gives rise to the digestive, respiratory, excretory and reproductive systems, while the mesoderm differentiates into bone, cartilage, muscle, fat and blood (connective tissues). A gradient in Wnt signaling across the blastula begins the differentiation of its layers into ectoderm, mesoderm and endoderm [17-19].

Similarly, *in vitro*, it has been observed that on the activation of Wnt signaling in hPSCs there is differentiation towards mesodermal fates [20-22]. Previous work done in the Palecek lab has also indicated that Wnt signaling activation leads to cardiac progenitor differentiation [23]. However, none of these studies look at the components of the Wnt signaling pathway within hPSCs.

Activation methods that have shown to be active in cancer cells are used on hPSCs, without investigating the components of the Wnt pathway [24]. In chapter 2 of this thesis, I investigate the components of Wnt pathway in hPSCs during pluripotency and differentiation.

The Wnt pathway is a highly conserved protein signaling pathway present in cells and implicated in both differentiation and cancer phenotypes of mammalian cells [25]. The protein β-catenin is produced at a high rate and moves to the cell membrane to form a structure called an adherens junction with E-cadherin. It then dissociates from this structure to enter the cytoplasm. Here, in the inactive state of Wnt signaling, β-catenin is phosphorylated by (Caesin Kinase) CK1α at Thr41/Ser45 and tagged for entry into the destruction complex. The destruction complex consists of several proteins, among which (Glycogen Synthase Kinase) GSK3β phosphorylates the Phospho-β-catenin Thr41/Ser45 at Ser33/Ser37/Thr41. This Phospho-β-catenin Ser33/Ser37/Thr41 is degraded by the cell, hence the β-catenin is destroyed by the destruction complex [26]. In the active state of the Wnt pathway, the destruction complex does not form, leading to cytoplasmic and then nuclear accumulation of β-catenin, and eventually, the transcription of Wnt responsive genes. Transcriptional activation of β-catenin occurs through phosphorylation at Ser552 and Ser675 by Akt and (Protein Kinase) PKA, and PKA only.

The dynamics of all of these phosphorylation states of β-catenin are not known through pluripotency and differentiation of hPSCs. Furthermore, the presence of several kinases implies that there may be additional control points for the Wnt pathway in hPSC differentiation through chemical inhibition. hPSCs are a unique system for evaluating these dynamics and control strategies due to their binary response to Wnt signaling (activation leads to differentiation and

inhibition can be used to maintain pluripotency[27]). Chapter 2 harnesses these properties to investigate the dynamics of β-catenin phosphorylation in hPSCs and uncover a new point of control of the Wnt pathway in hPSCs. In addition chapter 2 provides a new layout and mathematical framework for analyzing the Wnt pathway.

In addition to providing a source of tissues for replacement therapy in regenerative medicine, hPSCs can also be used to generate tissues that are hard to access and study *in vitro*. Tissues forming tight barriers within the body are difficult to study *ex vivo*. The barrier properties of these tissues are maintained through energy dependent mechanisms [28-31]. On isolation of these tissue from animal cadavers, there is some loss of energy-dependent barrier properties [32]. The use of hPSCs to generate these tissues entirely *in vitro* can provide a better system for studying barrier characteristics, as there is no cell death due to isolation techniques. The vocal fold epithelium is one such system that can be more easily studied using hPSC technology [28].

The vocal fold epithelium consists of four to six layers of tightly packed cells that lie over the muscular tissue of the vocal cords and over a collagen layer that provides structural integrity to the vocal folds called the lamina propria. This stratified layer of cells provide a barrier against chemical injury of the vocal fold muscle [28]. Given the constant exposure of the vocal folds to chemical agents present in air, an impairment to the vocal fold epithelial barrier leads to loss of vocal function [33]. However, extraction of vocal fold epithelium from animals leads to some destruction of the epithelia and only limited information can be obtained through the study of *ex vivo* human vocal folds [28].

In order to study this system, Thibeault and coworkers had developed a system for the *in vitro* differentiation for vocal fold epithelia [34]. In this model hPSC derived epithelial progenitors are seeded onto a collagen gel enmeshed with vocal fold fibroblast cells and grown at an air liquid interface to initiate stratification. The hPSC derived vocal fold epithelia thus formed resemble *in vivo* vocal fold epithelia with respect to morphology and protein marker expression.

Barrier measurement *in vitro* typically involves placing the barrier forming tissue on an insert and using it to separate two chambers containing media [35]. In the absence of a cellular barrier, ions can flow freely between the two chambers (leading to low electrical resistance), and dyes can flow easily between the chambers (leading to high permeability). However, when attempting to perform these assays on the collagen gel based hPSC derived vocal fold epithelial tissue it was observed that due to the shrinking nature of the collagen gel, the tissue does not form a confluent layer on the inserts that they are cultivated on. This impedes barrier measurement as ions and dyes can pass through the segments of the inserts lacking cells and make the system appear to have a reduced barrier phenotype. Differentiating the vocal fold epithelial tissue on the insert was thought to be able to tackle these problems. Chapter 3 outlines the development of a strategy for vocal fold epithelia differentiation on inserts and barrier characterization of these tissues.

Vocal fold epithelia are barrier forming cells, whose adherence to a surface defines their properties. Many other cell types have these properties, including several types of cancer cells [36]. In chapter 4, an investigation is performed into the change in adherence characteristics of epithelial cancer cells when placed on a superhydrophobic surface. A superhydrophobic surface

is one in which the contact angle of water exceeds 150°, this implies that water forms spherical beads on the surface rather than spreading onto it [37]. On these surfaces, a combination of micro and nano scale topography, along with surface functionalization creates a surface that causes the stabilization of an air layer between the water droplet and the surface [38]. Therefore, cells that are within a media droplet are unable to access a surface for attachment and spreading. Chapter 4 summarizes some of the changes that occur due to this form of cell culture of epithelial cancer cells.

1.1 Outline of the thesis

Chapter 1 introduces the three projects documented in this thesis. It introduces the key gaps in knowledge addressed in each of the chapters.

Chapter 2 is an investigation linking the components of the Wnt signaling pathway in hPSCs to the process of hPSC differentiation. It introduces a new control point for the Wnt pathway and a new layout and framework for mathematical analysis of the pathway.

Chapter 3 documents the development of a protocol for the differentiation of vocal fold epithelia on to Transwell® inserts. It further characterizes the carrier phenotype of these differentiated cells.

Chapter 4 charts phenotypic changes observed in epithelial cancer cells when placed on a superhydrophobic substrate. It documents the viability of the plated cells, their morphology and phenotypic differences in behavior between these cells and those grown on low attachment surfaces.

Chapter 5 summarizes results and future recommendations of these works.

1.2 References

1. Evans MJ, Kaufman MH. Establishment in culture of pluripotent stem cells in mouse embryos. Nature. 1981;292(5819):154-6. doi: 10.1038/292154a0. PubMed PMID: WOS:A1981LW55000043.

2. Thomson JA, Itskovitz-Eldor J, Shapiro SS, Waknitz MA, Swiergiel JJ, Marshall VS, et al. Embryonic stem cell lines derived from human blastocysts. Science. 1998;282(5391):1145-7. doi: 10.1126/science.282.5391.1145. PubMed PMID: WOS:000076887700056.

3. Odorico JS, Kaufman DS, Thomson JA. Multilineage differentiation from human embryonic stem cell lines. Stem Cells. 2001;19(3):193-204. doi: 10.1634/stemcells.19-3-193. PubMed PMID: WOS:000168989700003.

4. Yu JY, Thomson JA. Pluripotent stem cell lines. Genes & Development. 2008;22(15):1987-97. doi: 10.1101/gad.1689808. PubMed PMID: WOS:000258117500001.

5. Yu JY, Vodyanik MA, Smuga-Otto K, Antosiewicz-Bourget J, Frane JL, Tian S, et al. Induced pluripotent stem cell lines derived from human somatic cells. Science. 2007;318(5858):1917-20. doi: 10.1126/science.1151526. PubMed PMID: WOS:000251786600057.

6. Ludwig TE, Levenstein ME, Jones JM, Berggren WT, Mitchen ER, Frane JL, et al. Derivation of human embryonic stem cells in defined conditions. Nature Biotechnology. 2006;24(2):185-7. doi: 10.1038/nbt1177. PubMed PMID: WOS:000235232300034.

7. Chen GK, Gulbranson DR, Hou ZG, Bolin JM, Ruotti V, Probasco MD, et al. Chemically defined conditions for human iPSC derivation and culture. Nature Methods. 2011;8(5):424-U76. doi: 10.1038/nmeth.1593. PubMed PMID: WOS:000289987100021.

8. Daley GQ, Ahrlund-Richter L, Auerbach JM, Benvenisty N, Charo RA, Chen G, et al. The ISSCR guidelines for human embryonic stem cell research. Science. 2007;315(5812):603-4. doi: 10.1126/science.1139337. PubMed PMID: WOS:000243909400027.

9. Streiffer R. Chimeras, Moral Status, and Public Policy: Implications of the Abortion Debate for Public Policy on Human/Nonhuman Chimera Research. Journal of Law Medicine & Ethics. 2010;38(2):238-+. PubMed PMID: WOS:000279534400008.

10. Scott R, Williams C, Ehrich K, Farsides B. Donation of 'spare' fresh or frozen embryos to research: Who decides than an embryo is spare and how can we enhance the quality and protect the validity of consent? Medical Law Review. 2012;20(3):255-303. doi: 10.1093/medlaw/fws013. PubMed PMID: WOS:000307500000001.

11. Takahashi K, Tanabe K, Ohnuki M, Narita M, Ichisaka T, Tomoda K, et al. Induction of pluripotent stem cells from adult human fibroblasts by defined factors. Cell. 2007;131(5):861-72. doi: 10.1016/j.cell.2007.11.019. PubMed PMID: WOS:000251800900010.

12. Murry CE, Keller G. Differentiation of embryonic stem cells to clinically relevant populations: Lessons from embryonic development. Cell. 2008;132(4):661-80. doi: 10.1016/j.cell.2008.02.008. PubMed PMID: WOS:000253817900024.

13. Laflamme MA, Chen KY, Naumova AV, Muskheli V, Fugate JA, Dupras SK, et al. Cardiomyocytes derived from human embryonic stem cells in pro-survival factors enhance function of infarcted rat hearts. Nature Biotechnology. 2007;25(9):1015-24. doi: 10.1038/nbt1327. PubMed PMID: WOS:000249444200025.

14. Lindvall O, Kokaia Z, Martinez-Serrano A. Stem cell therapy for human neurodegenerative disorders - how to make it work. Nature Medicine. 2004;10(7):S42-S50. doi: 10.1038/nm1064. PubMed PMID: WOS:000223202100007.

15. Vodyanik MA, Yu J, Zhang X, Tian S, Stewart R, Thomson JA, et al. A Mesoderm-Derived Precursor for Mesenchymal Stem and Endothelial Cells. Cell Stem Cell. 2010;7(6):718-29. doi: 10.1016/j.stem.2010.11.011. PubMed PMID: WOS:000285537700013.

16. Lippmann ES, Azarin SM, Kay JE, Nessler RA, Wilson HK, Al-Ahmad A, et al. Derivation of blood-brain barrier endothelial cells from human pluripotent stem cells. Nature Biotechnology. 2012;30(8):783-91. doi: 10.1038/nbt.2247. PubMed PMID: WOS:000307416900022.

17. Dequeant M-L, Glynn E, Gaudenz K, Wahl M, Chen J, Mushegian A, et al. A complex oscillating network of signaling genes underlies the mouse segmentation clock. Science. 2006;314(5805):1595-8. doi: 10.1126/science.1133141. PubMed PMID: WOS:000242624600041.

18. Rodriguez-Gonzalez JG, Santillan M, Fowler AC, Mackey C. The segmentation clock in mice: Interaction between the Wnt and Notch signalling pathways. Journal of Theoretical Biology. 2007;248(1):37-47. doi: 10.1016/j.jtbi.2007.05.003. PubMed PMID: WOS:000249469300004.

19. Goldbeter A, Pourquie O. Modeling the segmentation clock as a network of coupled oscillations in the Notch, Wnt and FGF signaling pathways. Journal of Theoretical Biology. 2008;252(3):574-85. doi: 10.1016/j.jtbi.2008.01.006. PubMed PMID: WOS:000256771500026.

20. Davidson KC, Adams AM, Goodson JM, McDonald CE, Potter JC, Berndt JD, et al. Wnt/beta-catenin signaling promotes differentiation, not self-renewal, of human embryonic stem cells and is repressed by Oct4. Proceedings of the National Academy of Sciences of the United States of America. 2012;109(12):4485-90. doi: 10.1073/pnas.1118777109. PubMed PMID: WOS:000301712600033.

21. Tran TH, Wang XR, Browne C, Zhang Y, Schinke M, Izumo S, et al. Wnt3a-Induced Mesoderm Formation and Cardiomyogenesis in Human Embryonic Stem Cells. Stem Cells. 2009;27(8):1869-78. doi: 10.1002/stem.95. PubMed PMID: WOS:000270050900018.

22. Ueno S, Weidinger G, Osugi T, Kohn AD, Golob JL, Pabon L, et al. Biphasic role for Wnt/beta-catenin signaling in cardiac specification in zebrafish and embryonic stem cells. Proceedings of the National Academy of Sciences of the United States of America. 2007;104(23):9685-90. doi: 10.1073/pnas.0702859104. PubMed PMID: WOS:000247114100027.

23. Lian XJ, Hsiao C, Wilson G, Zhu KX, Hazeltine LB, Azarin SM, et al. Robust cardiomyocyte differentiation from human pluripotent stem cells via temporal modulation of canonical Wnt signaling. Proceedings of the National Academy of Sciences of the United States of America. 2012;109(27):E1848-E57. doi: 10.1073/pnas.1200250109. PubMed PMID: WOS:000306641100009.

24. Sato N, Meijer L, Skaltsounis L, Greengard P, Brivanlou AH. Maintenance of pluripotency in human and mouse embryonic stem cells through activation of Wnt signaling by a pharmacological GSK-3-specific inhibitor. Nature Medicine. 2004;10(1):55-63. doi: 10.1038/nm979. PubMed PMID: WOS:000187743600039.

25. Klaus A, Birchmeier W. Wnt signalling and its impact on development and cancer. Nature Reviews Cancer. 2008;8(5):387-98. doi: 10.1038/nrc2389. PubMed PMID: WOS:000255264700018.

26. Logan CY, Nusse R. The Wnt signaling pathway in development and disease. Annual Review of Cell and Developmental Biology. 2004;20:781-810. doi: 10.1146/annurev.cellbio.20.010403.113126. PubMed PMID: WOS:000225318200029.

27. Dravid G, Ye ZH, Hammond H, Chen GB, Pyle A, Donovan P, et al. Defining the role of Wnt/beta-catenin signaling in the survival, proliferation, and self-renewal of human embryonic stem cells. Stem Cells. 2005;23(10):1489-501. doi: 10.1634/stemcells.2005-0034. PubMed PMID: WOS:000233708700008.

28. Levendoski EE, Leydon C, Thibeault SL. Vocal Fold Epithelial Barrier in Health and Injury: A Research Review. Journal of Speech Language and Hearing Research. 2014;57(5):1679-91. doi: 10.1044/2014_jslhr-s-13-0283. PubMed PMID: WOS:000348200500008.

29. Petrova A, Celli A, Jacquet L, Dafou D, Crumrine D, Hupe M, et al. 3D In vitro model of a functional epidermal permeability barrier from human embryonic stem cells and induced pluripotent stem cells. Stem Cell Reports. 2014;2(5):675-89. doi: 10.1016/j.stemcr.2014.03.009. PubMed PMID: 24936454; PubMed Central PMCID: PMCPMC4050479.

30. Morita K, Miyachi Y, Furuse M. Tight junctions in epidermis: from barrier to keratinization. European Journal of Dermatology. 2011;21(1):12-7. doi: 10.1684/ejd.2010.1192. PubMed PMID: WOS:000289677500002.

31. Niessen CM. Tight junctions/adherens junctions: Basic structure and function. Journal of Investigative Dermatology. 2007;127(11):2525-32. doi: 10.1038/sj.jid.5700865. PubMed PMID: WOS:000250226800007.

32. Knight DA, Holgate ST. The airway epithelium: Structural and functional properties in health and disease. Respirology. 2003;8(4):432-46. doi: 10.1046/j.1440-1843.2003.00493.x. PubMed PMID: WOS:000187227600003.

33. Sataloff RT. THE IMPACT OF POLLUTION ON THE VOICE. Otolaryngology-Head and Neck Surgery. 1992;106(6):701-5. PubMed PMID: WOS:A1992JA31600015.

34. Leydon C, Selekman JA, Palecek S, Thibeault SL. Human Embryonic Stem Cell-Derived Epithelial Cells in a Novel In Vitro Model of Vocal Mucosa. Tissue Engineering Part A. 2013;19(19-20):2233-41. doi: 10.1089/ten.tea.2012.0744. PubMed PMID: WOS:000323933400015.

35. Balda MS, Whitney JA, Flores C, Gonzalez S, Cereijido M, Matter K. Functional dissociation of paracellular permeability and transepithelial electrical resistance and disruption of the apical-basolateral intramembrane diffusion barrier by expression of a mutant tight junction membrane protein. Journal of Cell Biology. 1996;134(4):1031-49. doi: 10.1083/jcb.134.4.1031. PubMed PMID: WOS:A1996VD43100018.

36. Brabletz S, Schmalhofer O, Brabletz T. Gastrointestinal stem cells in development and cancer. Journal of Pathology. 2009;217(2):307-17. doi: 10.1002/path.2475. PubMed PMID: WOS:000262390500016.

37. Feng XJ, Jiang L. Design and creation of superwetting/antiwetting surfaces. Advanced Materials. 2006;18(23):3063-78. doi: 10.1002/adma.200501961. PubMed PMID: WOS:000243183700001.

38. Lafuma A, Quere D. Superhydrophobic states. Nature Materials. 2003;2(7):457-60. doi: 10.1038/nmat924. PubMed PMID: WOS:000183892200018.

2 Modulation of Wnt induced human pluripotent stem cell differentiation by Protein Kinase A

2.1 Introduction

2.1.1 Human Pluripotent Stem Cells

Human pluripotent stem cells or hPSCs consist of two distinct cell types, human embryonic stem cells (hESCs) and human induced pluripotent stem cells (hiPSCs). hPSCs are pluripotent cells that are capable of forming any cell type in the human body. Human embryonic stem cells are derived from the pre-implantation embryo and are capable of unlimited proliferation *in vitro* while remaining undifferentiated. Cells with these properties were first derived by Thomson et al [1] from human embryos. Since their derivation, these cells have been used to model diseases [2, 3] and form viable tissue for transplantation *in vitro* [4]. However, the derivation of these cells results in the destruction of an embryo, thus prompting several bioethical concerns [5].

Embryonic stem cells come from a limited number of embryos and therapeutically cannot be autologous (non-foreign) to a transplantation recipient. This implies that there is a high probability of immune rejection in cases where hESCs are used to generate transplantable tissue. However, hiPSCs can be derived from cells from a patient's own body, thus reducing the risk of immune rejection. This technology makes development of transplantable tissue from hiPSCs a clinically viable alternative to hESCs. Additionally, there are fewer ethical considerations when harvesting adult body tissues than when harvesting pre-implantation embryos.

Induced pluripotent stem cells were first created by integrating four transcription factors (Oct4, Sox2, Klf4 and c-Myc) [6] into somatic cells to generate cells having an embryonic stem cell-like phenotype[6]. The transcription factors were packaged into a lentiviral vector which integrated into the chromosomes of the recipient somatic cells [7]. The major limitation of hiPSCs then was the need for chromosomal alteration and the use of lentivirus. However, both of these limitations have been overcome.

hiPSCs have now been derived without chromosomal integration[8] and viral vectors[9]. Hence tissues developed through the use of hiPSCs are viable for transplantation [10-12]. Jacob et al [12] have already demonstrated the potential for disease treatment by using autologous induced pluripotent stem cells to cure a mouse model for sickle cell anemia. These cells have also been used in the modeling of human diseases.

In cardiovascular medicine, for example, hiPSC technology has also been used to create several disease models for cardiac arrhythmic diseases [13, 14]. Moretti et al [13] collected dermal fibroblasts from Long QT syndrome patients, derived hiPSCs from these fibroblasts and then differentiated them into cardiomyocytes and captured action potentials characteristic to Long QT syndrome from these differentiated cells. This study demonstrated the possibility of creating viable functional tissue from an autologous source in humans. A similar study generated smooth muscle cells by differentiating hiPSCs derived from human aortic smooth muscle cells [15]. Thus functional cardiomyocytes and vascular cells (smooth muscle) can be derived from hiPSCs. The principle behind the use of hiPSC technology is that differentiation into cardiovascular lineages *in vitro* closely mimics the *in vivo* development of the heart. The potential underlying hiPSC

technology has been outlined in Figure 2.1[16]. However, the maintenance of pluripotency is a key requirement for the realization of the therapeutic potential of hPSCs.

2.1.2 Maintenance of hPSC pluripotency

Mouse pluripotent stem cells were first established by Martin et al [17] through isolation of the inner cell mass of the blastocyst and culture along with mouse embryonic fibroblast feeder layers. The media used in this case was DMEM/F12 supplemented with 20% fetal bovine serum (FBS). Thomson, about 17 years later attempted an analogous process in Wisconsin with human embryos and succeeded in creating human embryonic stem cell lines. Since then, the Thomson group has been dedicated towards the development of simpler and defined systems for stem cell maintenance.

The hPSC culture medium was then made defined by the use of KnockOut Serum replacer in place of fetal bovine serum for the maintenance of cells [18]. This system was later improved through the invention of mTeSR1 [19], a 64 component medium capable of maintaining hPSCs on Matrigel, a extracellular basement protein secreted by mouse sarcoma cells. More importantly, the development of mTeSR1 implied that there was no requirement for fresh mouse embryonic fibroblasts for the maintenance of hPSCs. However, mTeSR1 contained albumin, an animal derived component, which was susceptible to batch to batch variability.

Finally, through a pair-wise elimination of components in mTeSR1 to test elucidate components required for the maintenance of pluripotency, a new medium, termed E8, consisting of 8 components was developed [20]. In addition, it was shown that E8 and vitronectin, as an

extracellular matrix protein, are fully sufficient to derive and maintain hPSCs. It is this medium that I use in this study to maintain hPSCs.

Furthering the cause of simple, defined systems for the maintenance of pluripotency, the dissociation of hPSCs into single cells for the purpose of defined cell seeding was difficult for several years due to the epithelial nature of hPSCs [21]. Disruption of the epithelial structures caused programmed cell death. By inhibiting this disruption, hPSCs can be dissociated into single cells and plated in a defined manner. This disruption is inhibited using an inhibitor of the ROCK (Rho associated coiled-coil containing protein kinase) pathway, Y27632, which prevents the phosphorylation of phosphomyosin and thus prevents cell death due to cytoskeletal structure disruption. This compound was used in both this study and to develop precise conditions for vocal fold epithelia differentiation.

2.1.3 Differentiation of hPSCs

Adult or somatic cells are stable; they are capable of undergoing multiple divisions without any change in their phenotype. This helps maintain the structure and function of the tissues of the human body. However, stem cells are defined by their pluripotency, i.e. their ability to differentiate into any cell type in the body. Given this difference, Waddington [22] created the analogy of an epigenetic landscape shown in Figure 2.2[22].

The hPSC state is represented by the green ball, and the terminally differentiated somatic cell state is represented by the blue ball. While the green ball is free to roll down any of the grooves on the landscape and acquire any terminally differentiated phenotype, represented by the notches in the foreground; the blue ball cannot easily go over the hills in the foreground and

occupy another notch. hiPSC technology represents the blue ball backtracking its path and occupying the spot occupied by the green ball.

hPSCs can be directed to differentiate into a particular lineage or type of somatic cell. The differentiation is achieved through the activation of cellular signaling pathways through the addition of signaling proteins and small chemical activators [23, 24]. The control of these signaling pathways can be used to optimally control the differentiation fate of the hPSCs. The timed activation and deactivation of these signaling pathways *in vivo* leads to the embryonic development of specific organs and tissues within the mammalian body. Differentiation of hPSCs is achieved *in vitro* in many systems through mimicking of *in vivo* development events. The Wnt signaling pathway is an important signaling pathway in several developmental events.

2.1.4 The Wnt pathway

Canonical Wnt signaling is an evolutionarily conserved signaling pathway that is responsible for directing many developmental events, including heart formation and segmentation of the embryo, the first step leading to the development of vertebrae [25-27]. The signaling pathway is controlled by the location of β-catenin within the cell. In the absence of Wnt signaling, β-catenin is found in the cell membrane rather than the cytoplasm or the nucleus of the cell. A destruction complex consisting of the proteins, Axin, GSK3 and APC, tag the β-catenin present for degradation within the cytoplasm. This prevents β-catenin from entering the nucleus and transcribing Wnt responsive genes. However when Wnt signaling is active, the destruction complex cannot be formed and β-catenin is stabilized within the cytoplasm and can migrate to the nucleus. Within the nucleus, β-catenin forms a complex with TCF/LEF transcription factors and starts transcribing

Wnt responsive genes [28, 29]. Wnt activation may be achieved through the addition of a canonical Wnt ligand, Wnt-3a or through the addition of a GSK3 inhibitor, CHIR99021 [30]. The addition of the GSK3 inhibitor prevents the destruction complex from tagging β-catenin to be destroyed. This causes the accumulation of β-catenin within the cytoplasm, creating a situation analogous to the activation of Wnt signaling. A schematic of the pathway is shown in Figure 2.3. The regulation of β-catenin between the membrane cytoplasm and the nucleus occurs through several site-specific phosphorylation events.

2.1.5 Site-specific phosphorylation of β-catenin

The protein β-catenin is produced by the cell at high rate compared to other proteins in the cell [31]. This rate of production is correlated with a high degradation rate. After translation, β-catenin migrates towards the cell membrane to form an adherence junction complex with E-cadherin [32-34]. However some of the β-catenin may be phosphorylated at Thr41 and Ser45 by CK1α [35] as a precursor to phosphorylation by GSK3β. This phosphorylation tags β-catenin for entry into the destruction complex. A prominent cancer cell line SW480, was discovered to have a base pair deletion that removed Ser45, consequently, in this cell line, there is limited destruction of β-catenin and a high proliferative capacity (due to the continuous activation of Wnt responsive genes) generating a cancerous phenotype [25, 29, 35].

Once phosphorylated at Thr41/Ser45, the β-catenin interacts with the destruction complex, a protein agglomerate consisting of CK1α, GSK3β, Axin and APC as components. Here Axin and APC act as scaffolds for the kinases CK1α and GSK3β [25]. The Thr41/Ser45 phosphorylated β-catenin is primed for phosphorylation by GSK3β at Ser33, Ser37 and Thr41 [34]. This phosphorylated state

of β-catenin, Phospho-Ser33/Ser37/Thr41 β-catenin is tagged for ubiquitination and destruction within the cell.

However, β-catenin can also be phosphorylated nearer the C-terminus into two transcriptionally active states. Protein kinase A (PKA) phosphorylates β-catenin at Ser675 and at Ser552 [36, 37], while Akt1 phosphorylates β-catenin solely at Ser552 38]. Both of these phosphorylated states, Phospho-Ser552 β-catenin and Phospho-Ser675 β-catenin are capable of entering the nucleus and binding with transcription factor scaffolding proteins. In addition, mutating these sites has shown not to affect the destruction complex dynamics of β-catenin [4, 36]. Through this study I considered the two phosphorylation states differently and monitored their effects on hPSC differentiation.

2.1.6 Wnt signaling in hPSC regulation

Studies involving hPSCs and Wnt signaling have identified a role for Wnt signaling in both self-renewal [37] and differentiation [38] *in vitro*. Since *in vitro* differentiation is a recapitulation of *in vivo* development [4], the first few steps of development are described.

The zygote starts dividing post fertilization, and eventually forms a multicellular spherical structure called the morula. The cells in the morula then differentiate to form the blastocyst consisting of an outer hollow spherical cell layer called the trophectoderm and the inner cell mass from which human embryonic stem cells are derived. Implantation into the uterine wall happens at this stage. The trophectoderm attaches onto the uterine wall and the inner cell mass forms a disc like structure called the blastula.

The process of gastrulation which is the next step in development begins with the middle layer of the blastula forming a streak and migrating through this streak to penetrate the outer layer of cells. This streak is the primitive streak and defines the body axis for the developing animal, the spinal column develops along this streak. The three cell layers now start the process of differentiation into the three germ layers, called ectoderm, mesoderm and endoderm. The ectoderm differentiates into components of skin and nervous tissue; the mesoderm differentiates into components of the musculoskeletal system and the circulatory system; and the endoderm differentiates into components of the digestive, respiratory and endocrine systems. This structure consisting of the three germ layers is called the gastrula.

In multiple animal models, Wnt signaling via β-catenin has been shown to induce mesoderm formation through body axis duplication in the primitive streak stage [39-43]. The detection of primitive streak cells is accomplished by testing for the presence of the marker Brachyury [44-47]. A diagram indicating the developmental potential of Brachyury positive mesoderm and endoderm precursor cells highlights the importance of Wnt signaling in development and differentiation. Figure 2.4 indicates that Brachyury positive cells are a precursor for all cell types not derived from the ectoderm.

Wnt signaling activation had been used to maintain hPSC pluripotency in several studies [48-50]. The assumption that Wnt signaling promotes pluripotency in hPSCs is based on its unambiguous role in the maintenance of pluripotency in mouse embryonic stem cells [50, 51]. However, this analogy has not been fully applicable to human pluripotent stem cells. Cheng and coworkers [52] reported that Wnt proteins are not sufficient for maintenance of pluripotency of hPSCs.

Furthermore, Dalton and coworkers [53] established that Wnt inhibition is required for hPSC pluripotency and that interplay between the PI3K/Akt pathway and the Smad pathway determines the maintenance of pluripotency of hPSCs. Moon and coworkers [54] have shown that the downregulation of the pluripotency marker Oct4 and the increase in β-catenin and canonical Wnt signaling are correlated. They also show that the inhibition of the Wnt pathway shows no detrimental effects on the maintenance of pluripotency in hPSCs. Finally work done in our lab by Lance Lian [55] showed that continuous treatment of hPSCs with a specific GSK3 inhibitor caused the hPSCs to show elevated Wnt activity correlated with the expression of Isl1, a cardiac progenitor marker. This study details the processes by which Wnt signaling leads to hPSC differentiation.

2.1.7 Aim of the current study

The current study correlated the phosphorylation states of β-catenin during the process of mesendodermal (precursors of mesoderm and endoderm) differentiation of human pluripotent stem cells. Treating hPSCs with a Wnt agonist, a GSK3 inhibitor, causes the differentiation of hPSCs. However, it was not known how the phosphorylation of β-catenin is affected during this process. Wnt reporter studies indicated the upregulation of Wnt signaling, but direct measurements of β-catenin have not been done. In addition, little was known about the dynamics of β-catenin during the maintenance of a pluripotent state. This study addressed these gaps in knowledge. In addition, we discovered the effects of altering Wnt signaling, in conjunction with PKA signaling. We defined a mechanism for the changes observed and formulated a mathematical modeling framework for the Wnt induced differentiation of hPSCs.

2.2 Results

2.2.1 GSK3 inhibition leads to differentiation of hPSCs in 50 hours

In order to measure the kinetics of hPSC differentiation in the presence of GSK3 inhibitor CHIR99021, hPSCs cultured in E8 were seeded at 40,000 cells/cm^2 with ROCK inhibitor Y27632 and allowed to expand for 60 hours, after removal of ROCK inhibitor 24 hours after seeding. In 60 hours the density approached 150k cells/cm^2. At this time the cells were treated with either 4 µM CHIR or DMSO and allowed to grow for 50 hours. Cells were analyzed every 10 hours of growth.

Figure 2.5 shows immunostaining results for 0 hours, 30 hours and 50 hours after the addition of CHIR to E8 media. At the zero hour time point, top row, there was no Brachyury present, and all of the cells were Nanog positive indicating that the cells were pluripotent after 3 days of expansion. At the 30 hour time point, a majority of the cells expressed both Brachyury and Nanog, indicating that the process of differentiation was taking place during this time. However, by 50 hours, it was evident that all of the cells had differentiated, leading to a Brachyury positive population and no Nanog positive cells.

Since the differentiation had fully initiated by 30 hours of culture, we focused on the transition between 20 and 30 hours with both DMSO and CHIR treatment. Figure 2.6 shows the immunostaining images of the cells between 20 hours post CHIR addition and 30 hours post CHIR addition. Images indicating the control, DMSO condition are also included. In both panels A and B (20 hours after CHIR addition, A being DMSO treated and B being CHIR treated), it was observed that the cells stained positively for Nanog. In panel B, it was evident that there was lower staining

for Nanog, since the nuclear stain was also visible. However, in panel C (30 hours after DMSO addition) and panel D (30 hours after CHIR addition), the stark difference between the two states was plainly evident. DMSO treated cells continued to stain positively for Nanog, but CHIR treated cells stained sporadically for Nanog, and much more strongly for Brachyury, indicating that the differentiation occured between 20 and 30 hours. Figure 2.7 shows flow cytometry dot plots for Brachyury for all conditions tested, indicating the differentiation occurred between 20 and 30 hours after CHIR addition.

Looking through the top row in Figure 2.7, at 20 hours there was elevation in the Brachyury staining strength, but by 30 hours all of the cells stained positively for Brachyury. There was little change in the median intensity for the CHIR treated cells from 30 through 50 hours. What was also evident in this figure, was that the differentiation was not sporadic in nature. There was no separation of Brachyury positive and Brachyury negative populations through the differentiation process. The presence of the DMSO control flow plots indicated that the lack of separate Brachyury positive and negative populations was not due to staining characteristics of the antibody. Had it been due to non-specific staining, then the DMSO population would also have shown a shift in intensity (y-axis). Through the differentiation, there was a loss of Nanog positive cells, predictably between 20 and 40 hours as seen from Figure 2.8. There was an increase in Brachyury positive cells and a correlated decrease in Nanog positive cells during the same time.

This was also evident in the quantitative western blotting results shown in Figure 2.9. In panel (A), there was predictably only Brachyury seen in the CHIR treated samples, shown in grey. There was one blot showing Brachyury present at 30 hours in the DMSO control, but this was attributed

to being a staining artifact, rather than a true signal, the overwhelming data from flow cytometry presented in Figure 2.7 supported the low expression of Brachyury in the DMSO control.

Figure 2.9B shows the results of Nanog western blotting. A modest increase in Nanog could be expected as low activation of Wnt signaling could increase the expression of pluripotency markers in hPSCs. However, no significant changes were seen in Nanog expression, based on the two tailed t-test data presented in Table 4. Predictably, there was no expression of Nanog after 40 hours of CHIR treatment, while the DMSO control continued to express Nanog throughout the duration of the experiment. Since these phenotypic changes were solely brought about through treatment with a Wnt agonist, the dynamics of β-catenin and phosphorylated states of β-catenin were explored.

Two way ANOVA tests for both Brachyury and Nanog were performed comparing the CHIR and DMSO treated conditions at each time point, and across time points for each condition. Table 1 shows the p-value for Brachyury comparing the CHIR and DMSO treated cells. After 30 hours of treatment with CHIR, the cells showed significant Brachyury expression.

Table 2 compared the CHIR treated condition across each of the time points. There was significant elevation after 10 hours of treatment. For Nanog, Table 5 indicated that significant reduction occurred 40 hours after the addition of CHIR, while Table 4 indicated that no significant changes occurred on DMSO treatment.

2.2.2 Levels of β-catenin upon CHIR treatment

It was expected that there would be an elevation in total β-catenin on the addition of CHIR, shown in Figure 2.10. The inhibition of destruction of β-catenin by GSK3β was expected to cause lower amount of β-catenin to be ubiquitinated and therefore raise the level of total β-catenin. However, quantitative western blotting showed no significant changes with CHIR or DMSO. Two way ANOVA tests for β-catenin were performed comparing the CHIR and DMSO treated conditions at each time point, and across time points for each condition. No statistically significant changes were observed on either CHIR or DMSO addition. Table 6, Table 7 and Table 8 indicated these results. For all conditions, the p-value was greater than 0.2 comparing CHIR treatment to DMSO treatment, and the p-value was greater than 0.05 across all time points for DMSO treated cells and, the p-value was greater than 0.1 for all CHIR treated cells. This result, while unexpected, could be inferred from similar studies investigating density and β-catenin relationships.

Oesch and coworkers [56] reported that there was increased sub-cellular localization of β-catenin in confluent cells, as opposed to sub-confluent cells. Their study also reported an increase in total β-catenin in the confluent cell system. Similar density-β-catenin relationships were also observed in rat bronchial cells by Steele et al [57]. Given that the experiment was initiated near the point of confluence, the levels of total β-catenin observed are more indicative of the high area density of the cells. However the insignificant differences between the total β-catenin level observed between the CHIR and DMSO control mask the more significant differences in the phosphorylated β-catenin dynamics.

2.2.3 Destruction complex dynamics change throughout differentiation

Figure 2.11(A) shows the quantitative western blotting results for Phospho-Ser33/Ser37/Thr41 β-catenin and panel (B) shows the results for Phospho-Thr41/Ser45 β-catenin. Two way ANOVA tests were performed on the Phospho-β-catenin Thr41/Ser45 and the Phosho-β-catenin Ser3/Ser37/Thr41 data comparing both the CHIR and the DMSO condition at each time point and across time points. Table 9 indicates that Phospho-β-catenin Thr41/Ser45 showed significant elevation after 20 hours of CHIR treatment. Table 12 indicates that Phosho-β-catenin Ser3/Ser37/Thr41 showed significant elevation after 10 hours of DMSO treatment, but on CHIR treatment there was no increase from the low level present at the beginning of the experiment.

In the DMSO control, the levels of the Phospho-Ser33/Ser37/Thr41 β-catenin were significantly higher than the zero hour time point ($p<0.01$ for 40 and 50 hours post DMSO addition, Table 13). The GSK3β inhibitor was expected to inhibit this phosphorylation and reduce the amount of Phospho-Ser33/Ser37/Thr41 β-catenin being ubiquitinated. The insignificant changes observed on CHIR addition, p-value greater than 0.1 for all time points (Table 14) confirmed this hypothesis. However, the significantly (p-value less than 0.05, Table 9) elevated amounts of Phospho-Thr41/Ser45 β-catenin were interesting as well.

CHIR addition caused significant increase in Phospho-Thr41/Ser45 β-catenin over the DMSO control. Higher amounts of Phospho-Thr41/Ser45 β-catenin indicated that there was higher tagging of β-catenin for phosphorylation by GSK3β, therefore, upon the addition of CHIR, there was increased tagging of Phospho-Thr41/Ser45 β-catenin for phosphorylation, but as was evident

from panel (A), lesser phosphorylation itself. This surprising result could be rationalized through the analysis of the equilibrium dynamics of the β-catenin destruction pathway.

In an elucidation of the scheme involved in β-catenin homeostasis, Kirschner and coworkers [31] demonstrated that a simple set of three equilibria could be used to explain the behavior of the destruction complex. Unphosphorylated β-catenin is in equilibrium with Phospho-Thr41/Ser45 β-catenin which is in equilibrium with Phospho-Ser33/Ser37/Thr41 β-catenin, which is in equilibrium with ubiquitin tagged β-catenin. On the inhibition of GSK3β, the Phospho-Ser33/Ser37/Thr41 β-catenin level decreases and thus pushes the Phospho-Ser33/Ser37/Thr41 β-catenin – Phospho-Thr41/Ser45 β-catenin equilibrium in the backward direction, this causes the elevation of the Phospho-Thr41/Ser45 β-catenin species.

Through both panels in Figure 2.11, it was seen that the fundamental changes in the destruction complex β-catenin levels were established qualitatively within the first 10 hours. This was in agreement with other studies of destruction loop dynamics. Outside of the destruction complex there were notable differences in phosphorylated β-catenin dynamics as well.

2.2.4 Transcriptionally active β-catenin dynamics show differences

Figure 2.12 shows the dynamics of Phospho-Ser675 β-catenin in panel (A) and Phospho-Ser552 β-catenin in panel B. Phospho-Ser675 β-catenin indicates β-catenin phosphorylated by PKA, while Phospho-Ser552 β-catenin indicates β-catenin phosphorylated by both PKA and Akt. Two way ANOVA tests were performed on the western blotting data for both Phospho-β-catenin Ser675 and Phospho-β-catenin Ser552 comparing the CHIR and DMSO treated conditions at each time point and across time points respectively. Table 15 and Table 17 both indicated that the elevation

in Phospho-β-catenin Ser675 was statistically significant after 20 hours of treatment with CHIR (p-value less than 0.05, Table 17). For Phospho-β-catenin Ser552, Table 20 indicated statistically significant reduction (p-value less than 0.1, Table 20) following 30 hours of CHIR treatment. While the CHIR treated data sets for Phospho-β-catenin Ser552 were not significantly different from the 0 or 10 hour condition, comparing 20 hour, 30 hour, 40 hour and 50 hour CHIR treated conditions(Table 20) indicated statistically significant reduction happening across these time points. Changes in the DMSO treated condition were insignificant, as indicated in Table 19.

Previous studies had indicated a role for PI3K signaling in the maintenance of pluripotency of hPSCs [53]. PI3K, or phosphoinositide-3-kinase is the principle kinase responsible for Akt activation. It was therefore expected that this kinase would not be correlated with the differentiation of hPSCs. The correlation of Phospho-Ser675 β-catenin to Brachyury was unexpected.

The timing of the correlation indicated a transcriptional mechanism for the Phospho-Ser675 β-catenin induced transcription of Brachyury (we hypothesized that phosphorylation at Ser675 was correlated to Brachyury transcription). Significant Phospho-Ser675 β-catenin elevation occurred within the first 20 hours of treatment, while significant ($p<0.01$, Table 1) Brachyury elevation was observed 30 hours post CHIR addition. This 10 hour time gap in elevation seemed to suggest that PKA induced phosphorylation of β-catenin was responsible for the differentiation of hPSCs.

However, prior to testing that hypothesis, the correlation of Brachyury and Phospho-Ser675 β-catenin was tested via immunostaining.

2.2.5 Phospho-Ser675 β-catenin is correlated to differentiating cells

Figure 2.13 shows immunostaining results for cells that have been treated with CHIR for 30 hours, panel (A) and cells that were treated with DMSO for 30 hours, panel (B). Brachyury is represented on the red channel, Phospho-Ser675 β-catenin is represented on the green channel, and nuclei are represented on the blue channel. On the inspection of panel (A), it was evident that there was co-localization of Phospho-Ser675 β-catenin and Brachyury, while Phospho-Ser675 β-catenin levels were low, and present only in the densest parts of the DMSO control.

This co-localization appeared to confirm that there was correlation between Phospho-Ser675 β-catenin and Brachyury and indicated a role for PKA in the differentiation of hPSCs. We have shown that PKA phosphorylated β-catenin is correlated with differentiated cells. However, if it was responsible for the differentiation, inhibition of PKA should inhibit the formation of Brachyury positive cells, and Brachyury levels measured via western blotting. To test this hypothesis, hPSCs were treated with several PKA inhibitors, in conjunction with CHIR, at several doses to check for Brachyury, Phospho-Ser675 β-catenin, Phospho-Ser552 β-catenin and total β-catenin levels.

2.2.6 PKA inhibition reduces Brachyury and total β-catenin levels

The three PKA inhibitors used for this experiment were KT5720, Rp-CAMPs and H89 [58]. Three inhibitors were used as all three have cross reactivity with other cyclic-AMP kinases, including Akt. KT5720 is considered to be the most specific, having a PKA K_i about 30 times lower than the nearest interfering kinase. Whereas H89 is considered the most promiscuous amongst the protein kinase inhibitors used [59]. The concentrations of the kinase used were based on

preliminary testing to indicate what concentration was required to cause significant cell death. The maximum concentrations of KT5720, Rp-CAMPs and H89 used were 1 µM, 20 µM and 20 µM. The low, medium and high concentrations used were 20%, 50% and 100% of the maximum concentration represented.

In addition, three other controls were used in this experiment. The first was the no CHIR, no inhibitor control, the second was the CHIR, no inhibitor control, and the third was the no CHIR, maximum inhibitor concentration control. The latter control was required to ascertain that the inhibitors were not causing significant cell death leading to density induced changes, and that the inhibitors themselves were not differentiating the hPSCs.

Figure 2.14(A) shows the results of the western blot for Brachyury on the addition of the PKA inhibitors in conjunction with CHIR, after 30 hours of culture. The controls lacking CHIR treatment predictably showed no Brachyury, indicating that the PKA inhibitor by itself was not causing mesendodermal differentiation. The last control, with CHIR and without any inhibitors showed maximum Brachyury expression, indicating a positive control. At a high concentration, both KT5720 and H89 were capable of inhibiting differentiation. With Rp-CAMPs, there was some inhibition but not complete inhibition. Through this panel, qualitatively, it was evident that the H89, gray bar is most effective at inhibition of differentiation. KT5720 was also effective, but less so at lower concentrations.

Figure 2.14(A) shows the results of the western blots for total β-catenin on the addition of the PKA inhibitors in conjunction with CHIR, after 30 hours of culture. Through the investigation of the first two groups of bars, it was evident that PKA inhibition was causing a decrease in β-catenin

levels. This could be due to some cell death occurring during inhibitor treatment, or could be due to the inhibition of other phosphorylated forms of β-catenin.

2.2.7 PKA inhibition reduces transcriptionally active β-catenin

Figure 2.15 shows the western blotting results for Phospho-Ser552 β-catenin in panel (A) and Phospho-Ser675 β-catenin in panel (B). In both KT5720 had the most drastic effect on their concentrations and Rp-CAMPs has the least drastic effect. PKA is responsible for both the phosphorylation at Ser552 and Ser675, therefore it was expected that there is a reduction in both these species upon PKA inhibition.

What was noteworthy was that there seemed to be concentration dependence for Phospho-Ser552 β-catenin inhibition but limited concentration dependence for Phospho-Ser675 β-catenin inhibition. This trend, however, could not be spoken to with certainty, as the experiments were not performed with replicates that could provide an accurate estimate of the results. Moving forward, using just the high concentration used in these experiments could help elucidate the true effects of using these inhibitors to inhibit PKA.

2.2.8 PKA inhibition attenuates differentiation

hPSCs were treated with 1μM KT5720 along with either CHIR or DMSO for 50 hours and the cells analyzed via immunostaining. Figure 2.16 shows that in either condition, there was no formation of Brachyury, which was expected on the addition of CHIR. For the DMSO + KT condition, Brachyury formation was not expected.

Therefore, the inhibition of PKA with the most specific inhibitor indicates that there was a reduction in the differentiated cells post CHIR addition. Hence, we have identified a control point for Wnt signaling in hPSCs downstream of GSK3β. In both cases, there are some cells that are not Nanog positive or Brachyury positive, there is a possibility that these cells either stained weakly for Nanog or were differentiating into non-mesendodermal cell types.

2.2.9 Mechanism proposed to explain trends

Through the previous data, we established that the loss of Nanog, and gain of Brachyury expression occured over 50 hours after inducing differentiation with CHIR. The differentiation process was not stochastic, affecting almost all of the cells equally. The main differentiation appeared to occur 20 – 30 hours post CHIR addition. Phosphorylated β-catenin analysis indicated that Phospho-Ser675 β-catenin was correlated with Brachyury expression. This indicated a role for PKA in the differentiation of hPSCs, which was confirmed by inhibiting PKA, and then observing the loss of Brachyury expression. A model was constructed to explain these changes, shown as a schematic in Figure 2.17.

Briefly β-catenin is synthesized by the cell and can then be phosphorylated by one of three kinases. CK1α phosphorylating it reversibly to Phospho-Thr41/Ser45 β-catenin, PKA phosphorylating it to Phospho-Ser675 β-catenin and both PKA and Akt phosphorylating it to Phospho-Ser552 β-catenin. The Phospho-Thr41/Ser45 β-catenin is then further reversibly phosphorylated by GSK3β to Phospho-Ser33/Ser37/Thr41 β-catenin, which is then ubiquitinated and destroyed.

However, with regards to Phospho-Ser675 β-catenin and Phospho-Ser552 β-catenin, there are several transcriptional events that can be triggered. Both were modeled to transcribe Brachyury and Nanog. In addition, there is synthesis of Nanog in hPSCs. A detailed mathematical model based on this reaction scheme could reveal greater insight into the phosphorylation dynamics of β-catenin in hPSCs.

2.2.10 Mathematical modeling of hPSC Wnt differentiation

2.2.10.1 Review of mathematical modeling of Wnt pathway

The first model of the Wnt pathway, based on data from *Xenopus laevis* egg extracts was published in 2003 by Lee and Salic et al [60]. This model was used to verify the trend of β-catenin in egg extracts under conditions of no synthesis of β-catenin and addition of exogenous Axin. The biological data generated from this model was used in many other models of the Wnt pathway, reviewed by Wolf and coworkers [61]. This model described the core pathway and its reactions. Various other models investigated the characteristics and feedback loops of the pathway, without the addition of further biological data [62-68]. However the first models to integrate new biological data into the Wnt mathematical models came after 2010.

Work by Tan et al [69] sought to measure the concentration of Wnt signaling components in mammalian cells. Lee and Salic [60] used their model to indicate that the low cytosolic concentration of Axin implied minimal destruction of β-catenin within the destruction complex. However, Tan et al [69] found that Axin concentrations in mammalian cells was high, and that findings from the original model needed to be reevaluated in the context of mammalian cells. Mazmondet et al [70] sought to answer the question what was the extent of stochastic

fluctuation in β-catenin in neural cells. Using a simple 3 equation system, they established that the Wnt pathway dynamics were more deterministic, rather than stochastic in nature.

A major breakthrough in Wnt modeling came from the work of Kirschner and coworkers [31] showing that a simple 3 equilibrium system could explain β-catenin homeostasis dynamics in a variety of cancer cells under various conditions. Their experiments covered a duration lasting up to two hours of treatment with Wnt ligands and global phosphatases.

Finally, reporting in PNAS, MacLean et al [71] analyzed several mathematical models of the Wnt pathway and adapted them to their own model. They used Bayesian methods to infer predictions without parameter estimation. Finally they used the model to indicate the presence of two possible steady states of cells, a stem state and a steady state. Their model however, did not support any new biological data apart from that provided by Lee and Salic[60], and while it explained the switching of states, it did not cover the dynamics during the switching itself.

Therefore using the layout established in Figure 2.18 could provide a new method of analyzing the Wnt pathway focusing on the dynamics of the Wnt pathway parameters over an extended time period. By associating the Phospho-Ser552 β-catenin and Phospho-Ser675 β-catenin with Wnt transcriptional outputs, the model could also be adapted to different systems and cell types.

2.2.10.2 Structure of the model

The model consists of two synthesis and three degradation reactions along with 4 enzymatic reactions and 4 transcription events. The synthesis reactions indicates are the synthesis of β-catenin and the synthesis of Nanog, both of which are constant rate, zero order reactions. The

degradation reactions are degradation of β-catenin, first order with respect to Phospho-Ser33/Ser37/Thr41 β-catenin, degradation of Nanog, first order with respect to Nanog, and degradation of Brachyury, first order with respect to Brachyury. The four enzymatic reactions are catalyzed by CK1α, GSK3β, PKA and PKA and Akt; all of which were modeled on Michaelis-Menten kinetic reactions.

The argument for modeling these reactions as Michaelis-Menten reactions, as opposed to mass action kinetics is to facilitate the use of inhibitors within the model. Site-specific inhibitors have not as yet been modeled as part of the Wnt pathway. Using inhibitors causes a reduction in the K_m of the reaction and thus alters the kinetics. Equation 1 represents the standard Michaelis-Menten kinetics equation, Equation 2 shows the alteration of the Michaelis-Menten constant on the addition of an inhibitor, and Equation 3, the Cheng-Prusoff equation shows a method for calculating the inhibitor association constant from the equivalent IC_{50}. This structure allowed for using enzyme kinetics to model the Wnt pathway.

The model was constructed in Cell Designer software [72], including the design of all of the rate expressions involved in the model. The output schematic from CellDesigner is shown in Figure 2.17. Reaction re 1 whose rate expression is Equation 4 represents the synthesis of β-catenin within the cell. It is then phosphorylated by CK1α at Thr41/Ser45 in reaction re2 whose rate expression is Equation 5. The Phospho-β-catenin Thr41/Ser45 is then phosphorylated by GSK3β at Ser33/Ser37/Thr41 in re3 whose rate expression is Equation 6. The Phospho-β-catenin Ser33/Ser37/Thr41 is then destroyed in re4, whose rate expression is Equation 7.

The transcriptionally active phosphorylation events, are represented by re5 and re6 whose rate expressions are Equation 8 and Equation 9 respectively indicating the formation of Phospho-β-catenin Ser552 and Phospho-β-catenin Ser675. The proportion of PKA phosphorylated β-catenin phosphorylated at Ser675 is indicated using a ratio term x_{PKA} that varies between 0 and 1. The transcription of Brachyury through Phospho-β-catenin Ser675 and Phospho-β-catenin Ser552 is shown in re7 and re 10 whose rate expressions are Equation 10 and Equation 12. The transcription of Nanog through Phospho-β-catenin Ser675 and Phospho-β-catenin Ser552 is shown in re11 and re12, whose rate expressions are Equation 11 and Equation 13. Nanog synthesis is shown in re15 whose rate expression is Equation 15, and the destruction of Brachyury and Nanog happen in re13 and re14, whose rate expressions are Equation 14 and Equation 16.

Parameter estimation and fitting was performed using the SloppyCell tool [73, 74]. SloppyCell tackles the problem that many biological models typically involve free parameters, which are poorly constrained. These parameters have sensitivities distributed across several decades. Using collective fits, the tool aims to make predictions based on the model data, rather than estimating parameters. However, when applied to this model of the Wnt pathway, even basic model fits for the DMSO control condition were lacking.

2.2.10.3 Parameterization Challenges

The parameters used in the model were adapted from Hernandez et al [31] for the destruction loop dynamics. Guesses were made for the remaining parameters from other literature sources [68, 69, 75].

Table 21 shows the parameters used for the initial guesses. Figure 2.19 shows the fit of the experimental simulation to the data for Nanog and β-catenin. The fit for Nanog was adequate, as it showed little to no variation in Nanog across the growth time. The fit for β-catenin showed a slight increase over baseline. The large error bars of the experimental data set made the fits difficult to evaluate. However, when analyzing the fits for Phospho-Thr41/Ser45 β-catenin and Phospho-Ser33/Ser37/Thr41 β-catenin, as shown in Figure 2.20, it was evident that the model was solely equilibrating over the simulation time, rather than reacting to the data set provided.

In the fit for Phospho-Thr41/Ser45 β-catenin, labelled as Catenin-TS in the figure, it was seen that there was a general rise in the species, until it approached a new equilibrium value of about 1.5 nM. Were the model initially equilibrated, and the species concentration adjusted to 1.5 nM, rather than the initial guess value of 0.4 nM, the SloppyCell tool would not have adjusted parameters to enable the trend to match experimental data. In the model fit graph for Phospho-Ser33/Ser37/Thr41 β-catenin, labelled Catenin-SST in the figure, this was plainly evident. The initial set value for this concentration is about 0.3 nM, however, there was rapid equilibration in the first few time steps giving it an almost zero value.

Figure 2.21 shows the parameter fit for Phospho-Ser675 β-catenin and Phospho-Ser552 β-catenin. While the Phospho-Ser675 β-catenin agreed with experimental values, again the model failed entirely to fit Phospho-Ser552 β-catenin. Thus on the first run, the model fitting seemed to only work for certain species.

In order to improve the simulation results, the model should be rewritten to parametrize the relative values, rather than the guessed absolute concentrations in this case. In addition density

changes must be integrated into the model, due to the effect that density has on the Wnt pathway. Without the density changes incorporated, the four enzymatic equilibria of the model all have equilibration times around 2 hours. The steady increase seen in the fit for Phospho-Ser675 β-catenin is due to PKA Michaelis Menten constants being estimated far below their actual numbers. Density could be incorporated as a product of transcription of Phospho-Ser675 β-catenin and Phospho-Ser552 β-catenin and as a factor controlling the rate of β-catenin destruction in the model. More work needs to be done to adequately parameterize the model and make predictions.

2.3 Conclusion

This study established that the Wnt induced differentiation of hPSCs, *ceterus paribus*, without changing the basal media took up to 50 hours, occurring between 20 and 30 hours. It established that the differentiation was not a stochastic event, and that all cells differentiated at around the same time. It established that there was significant elevation of PKA phosphorylated β-catenin, Phospho-Ser675 β-catenin during the differentiation event. This species was also correlated with the presence of Brachyury in cells. Finally, it also established that the inhibition of PKA led to the inhibition of differentiation in the cells via western blotting and immunochemistry. Therefore, it identified a novel control point for the Wnt signaling pathway in hPSCs downstream of the destruction loop.

The observations regarding Brachyury, Nanog and PKA phosphorylated β-catenin were used to create a novel layout for the Wnt pathway in hPSCs. This layout, focused on the phosphorylation events rather than the destruction loop dynamics (in contrast to previous layouts of the Wnt

pathway). Newly produced β-catenin can be phosphorylated by any of three kinases, CK1α, PKA or Akt leading to either eventual destruction via GSK3β phosphorylation or two distinct transcriptional events. These transcriptional events lead either to the synthesis of Nanog or Brachyury. By altering the identity of the transcriptional products, the layout could be easily adapted to other systems in which Wnt has transcriptional roles. For example, Wnt induced epithelial to mesenchymal transition [76] could be studies by considering E-cadherin and N-cadherin in place of Nanog and Brachyury. Similarly, Wnt induced neural crest cell differentiation [77] could also be studied using this layout.

Finally, a mathematical framework was built on this layout. The framework utilized Michaelis-Menten reaction rate laws for modeling the phosphorylation events, along with zeroth order synthesis reactions for β-catenin and Nanog, along with first order synthesis reactions for Brachyury and first order destruction reactions for GSK3β phosphorylated β-catenin, Nanog and Brachyury. Once parameterized adequately, the model can be used to perform *in silico* experiments involving combinations of kinase inhibitors to build complex control systems for the Wnt pathway. Substitutions of Nanog and Brachyury for other transcriptional targets could allow for detailed control analysis of the Wnt pathway and help identify other combinations of inhibitors to engineer a variety of Wnt responses.

2.3.1 Qualitative improvement of the study

The correlation of Phospho-Ser675 β-catenin and Brachyury could be probed using flow cytometry effectively. By probing for Nanog, Brachyury, β-catenin and Phospho-Ser675 β-catenin simultaneously, several questions may be answered. Are there two populations of cells

expressing a high β-catenin concentration and a low β-catenin concentration? If so, are the low β-catenin cells Nanog positive, and the high β-catenin cells Brachyury positive? Alternatively, if there is uniform β-catenin across all of the cells, are the high Phospho-Ser675 β-catenin cells positive for Brachyury? These questions could be answered by probing for all 4 antigens simultaneously.

Immunoprecipitation could help link the phosphorylated states to transcription factors in the nucleus. Transcription factors TCF3 and LEF1 are known to bind to β-catenin within the nucleus. TCF3 is also known to be a major regulator of pluripotency, therefore, it is possible that Phospho-Ser552 β-catenin binds TCF3 and LEF1 binds Phospho-Ser675 β-catenin. This would increase the understanding of Wnt in hPSCs, and complete the mechanism from cell membrane to nucleus and translation.

2.3.2 Quantitative improvement of the study

The error bars on the Western blots need to be reduced. In addition, more work could be done towards equilibrating and parameterizing the model. The model could be initially equilibrated at two states, the zero hour state and the fifty hours with CHIR state. Density could be incorporated into the model, and a dependence of Brachyury on Nanog synthesis could be integrated. As the Brachyury concentration rises, the Nanog synthesis rate should diminish, rather than be a zeroth order reaction as it was for the generated graphs. Once parameterized, predictions for enzyme inhibitions can be made and tested across a variety of cell types and Wnt responsive proteins.

2.4 Materials and methods

2.4.1 hPSC culture and differentiation

hPSCs were obtained as frozen vials and banked under feeder independent conditions in mTeSR1 medium (STEMCELL Technologies, Vancouver, Canada). hPSCs were then thawed and cultured directly into E8 medium consisting of DMEM/F-12 (Life Technologies, Carlsbad, CA), 64 mg/l ascorbic acid (Sigma), 543 mg/l sodium bicarbonate (Sigma, St. Louis, MO), 14 µg/l sodium selenite (Sigma), 19.4 mg/l insulin (Sigma), 10.7 mg/l transferrin (Sigma), 100 µg/l FGF2 (Waisman Clinical Biomanufacturing Facility, University of Wisconsin-Madison), and 2 µg/l TGFβ1 (Peprotech, Rocky Hill, NJ). pH of E8 medium was adjusted to 7.4 and osmolarity was adjusted to 340 mOsm with NaCl. hPSCs were maintained on Matrigel (BD Biosciences, San Jose, CA). Cell line used in this study were H9 human embryonic stem cells (hESCs) (passages 25–35)

2.4.2 Immunostaining

hESCs cultured in microwells or on Matrigel-coated glass coverslips were fixed in 4% paraformaldehyde (EMS) for 20 min at room temperature. Samples were blocked and permeabilized for 1 hour in blocking buffer, PBS (Invitrogen) containing 5% chick serum (Invitrogen) and 0.2% Triton X-100 (Sigma). Primary antibodies (Cell Signaling Technologies, Danvers, MA) were incubated overnight at 4°C in blocking buffer, and after subsequent washes in PBS cells were incubated in blocking buffer containing chicken anti-mouse Alexa 488 (1:500, Invitrogen) and donkey anti-goat Alexa 594 (1:500, Invitrogen) for 1 hour at room temperature. Following PBS washes, the cell nuclei were labeled with Hoechst (1:5000, Invitrogen) for 20 min.

Samples were imaged using a Bio-Rad Radiance 2100 Multiphoton Rainbow microscope (Bio-Rad).

2.4.3 Flow Cytometry

Cells were detached using 0.25% trypsin-EDTA (Invitrogen), fixed in 1% paraformaldehyde for 10 min at 37°C, and permeabilized in ice-cold 90% methanol for 30 min. Primary antibodies (Brachyury, R&D Systems, Nanog, BD Biosciences) were incubated overnight in FACS buffer (PBS with 2%FBS and 0.1% Triton X-100). Following 2 PBS washes, cells were incubated with donkey anti-rabbit Alexa488 (1:1000, Invitrogen) and donkey anti-goat Alexa633 (1:1000, Invitrogen) for 30 min at room temperature (for Oct4 flow only). After 2 PBS washes, samples were analyzed on a FACSCaliber flow cytometer (Becton Dickinson Immunocytometry Systems, BDIS) using CellQuest software.

2.4.4 Western Blotting

Proteins were quantified using a BCA protein assay (Pierce), resolved on a 12% polyacrylamide gel and transferred to a nitrocellulose membrane. After blocking with 5% powdered milk in TBS + 1% Tween-20 for 1 hour at room temperature, membranes were labeled with primary antibodies (Cell Signaling Technology. Danvers, MA) overnight at 4°C followed by horseradish peroxidase-conjugated secondary antibodies overnight at 4°C. Protein levels were detected via a SuperSignal West Pico Chemiluminescent Substrate (Pierce). Quantification performed using ImageJ software.

2.4.5 Figures

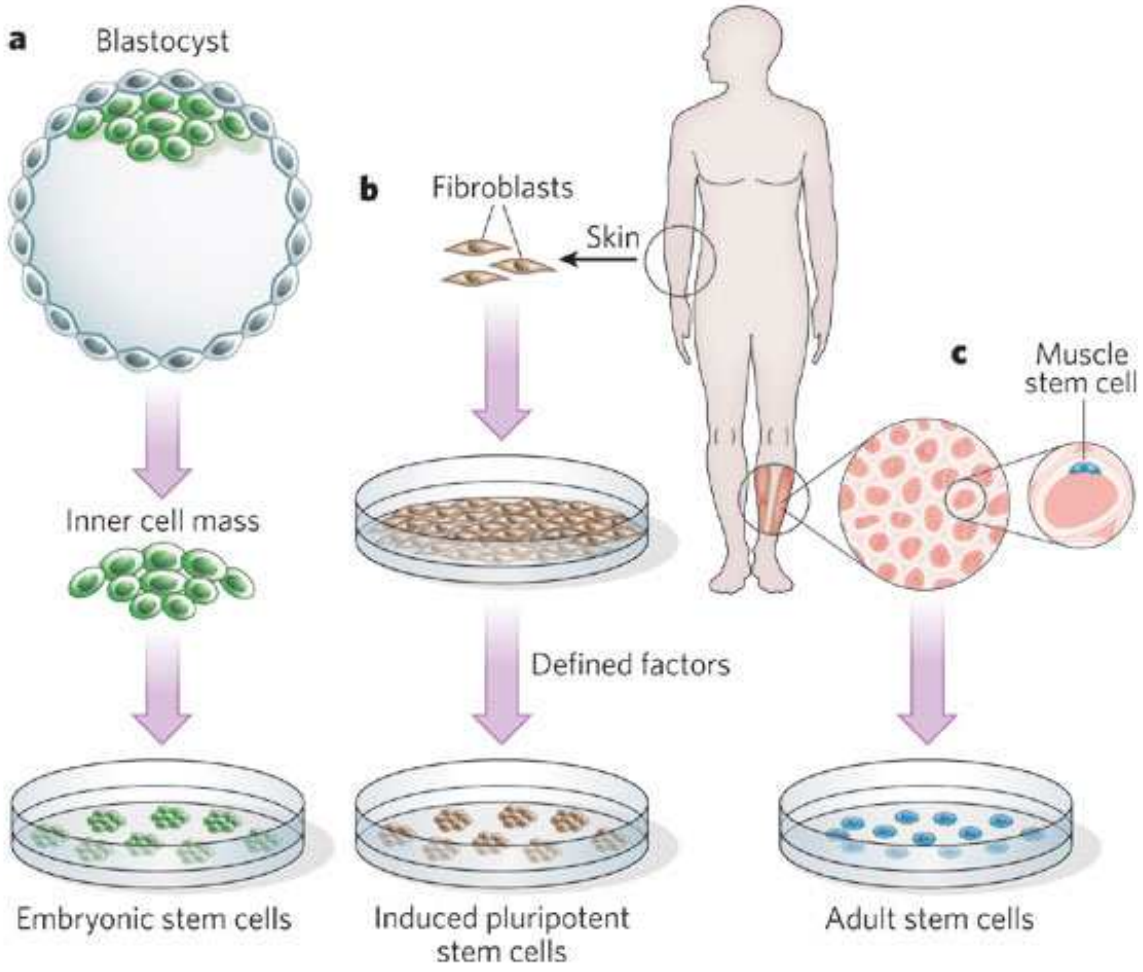

Figure 2.1: Schematic showing the variety of sources for hPSCs [78].

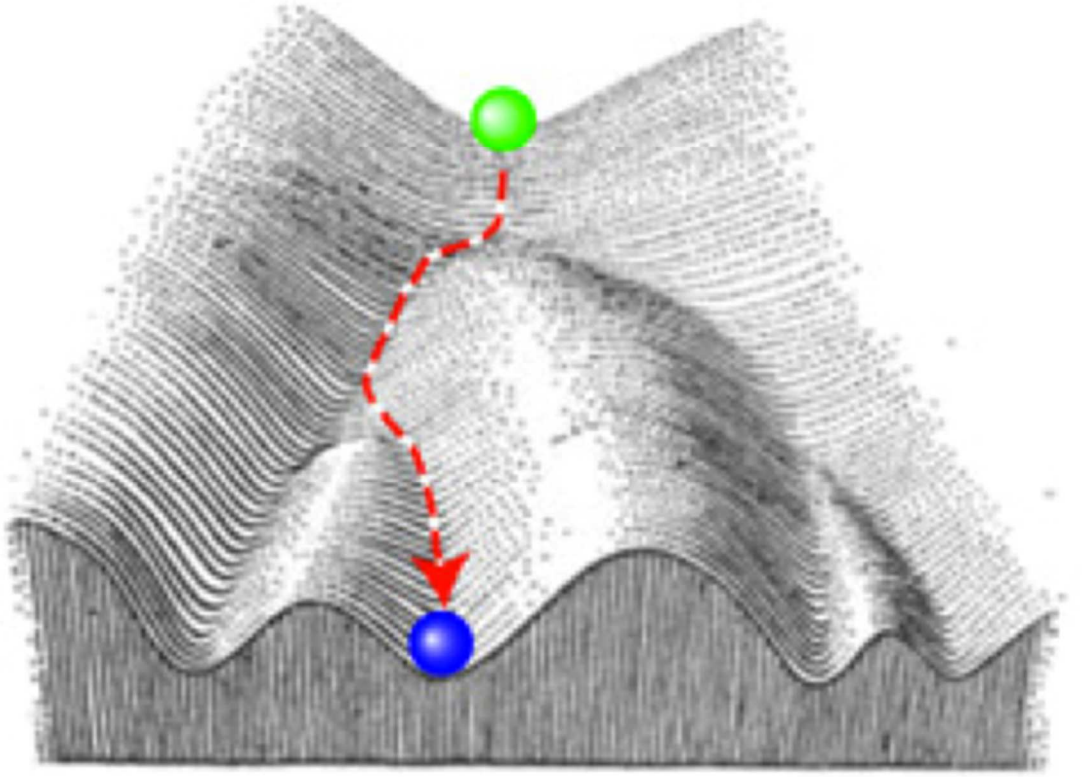

Figure 2.2: Waddington's epigenetic hypothesis. The green ball is a more multipotent state than the blue ball, which has already rolled down the epigenetic landscape to form somatic tissue. It is unlikely that the blue ball will roll up and back down to occupy any of the other slots at the bottom of the landscape [22].

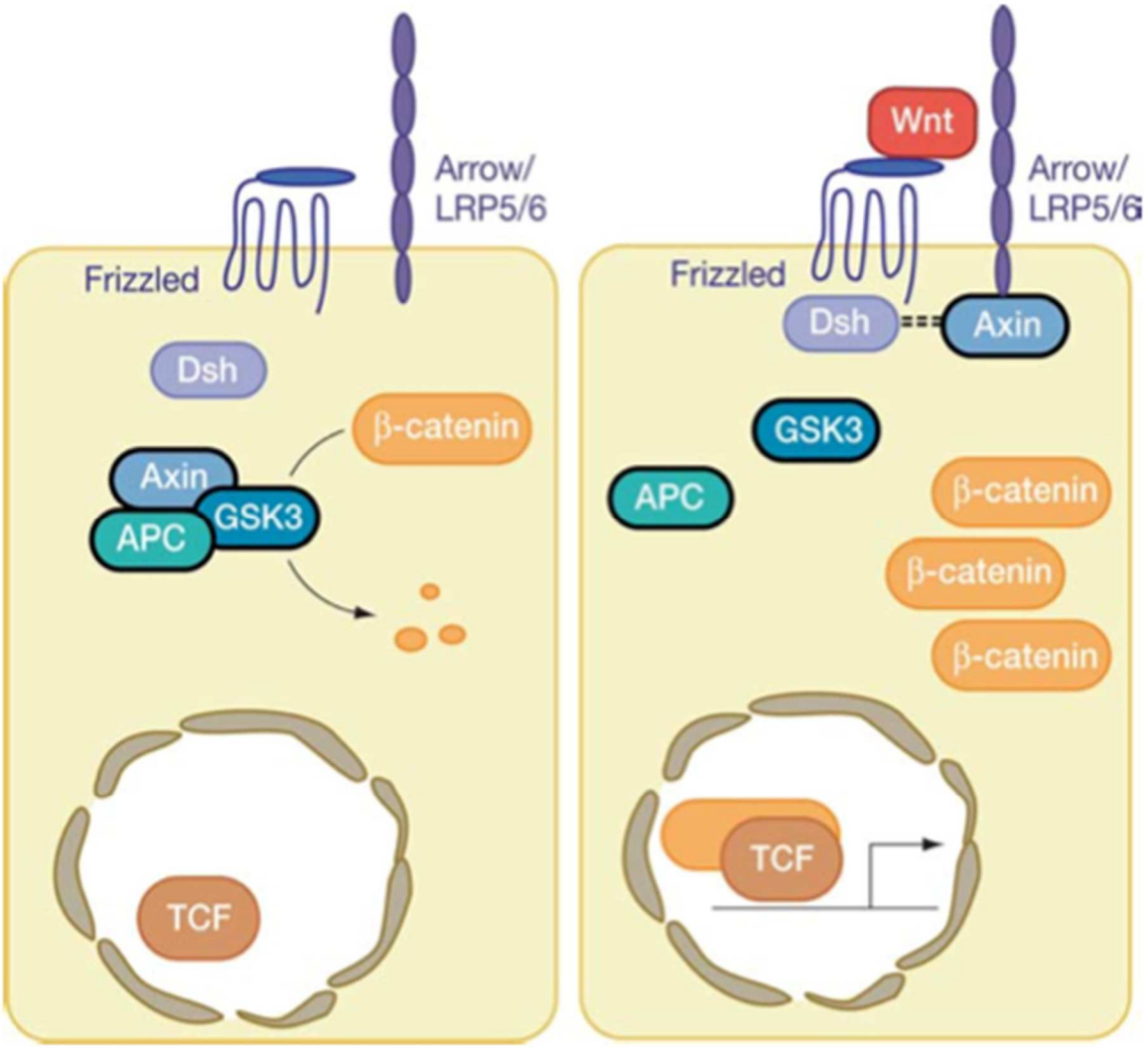

Figure 2.3: A schematic of the canonical Wnt pathway in its off and on state, adapted from Logan and Nusse [25].

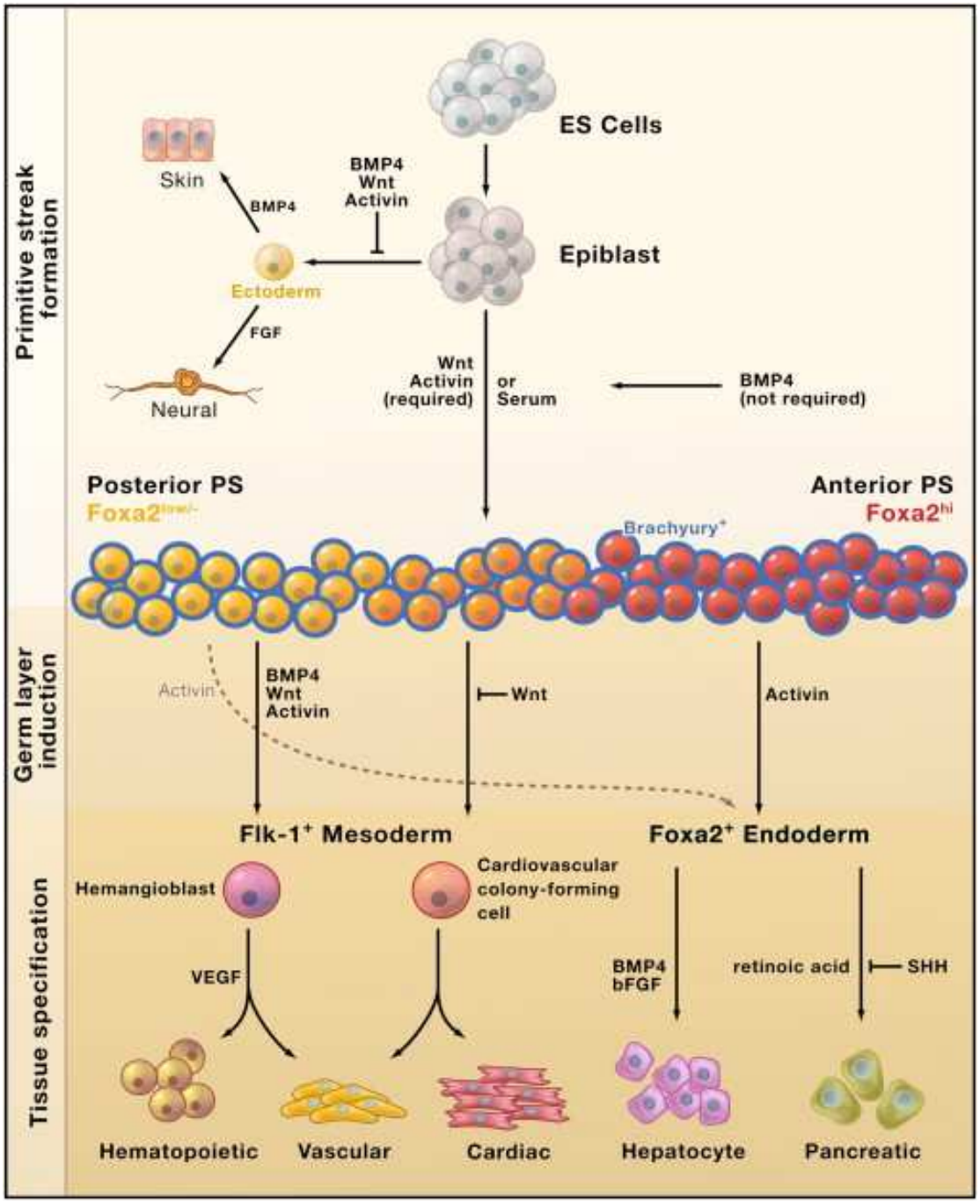

Figure 2.4: Schematic showing the terminal fates of Brachyury positive mesendodermal progenitors indicating the important role of Wnt signaling in development and differentiation[4].

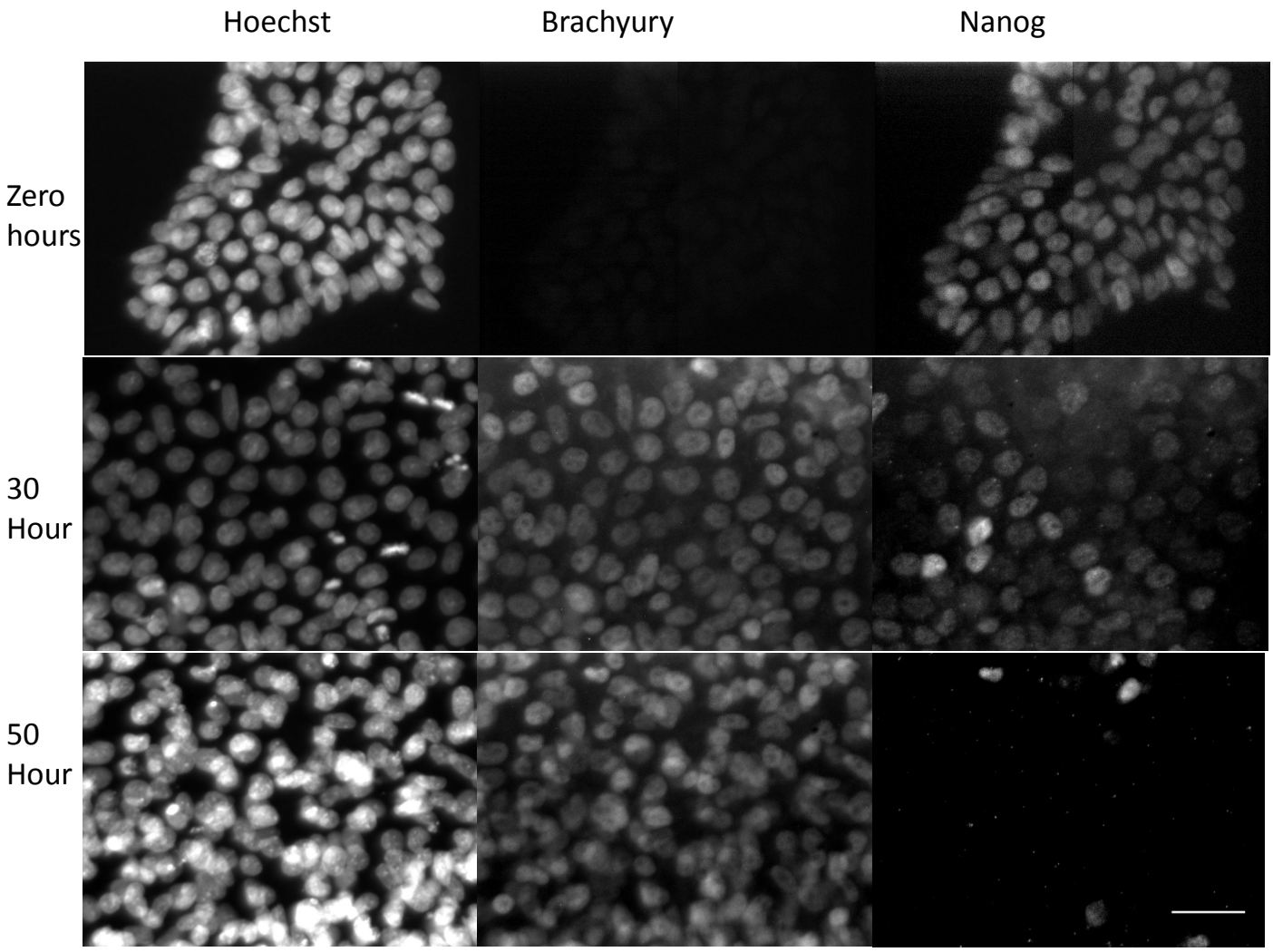

Figure 2.5: Immunostaining showing the differentiation of hPSCs on the addition of 2 µM of CHIR to cells in E8 over 0 hours, 30 hours and 50 hours. There is beginning Brachyury expression at 30 hours, along with residual Nanog expression, however this disappears in the next 20 hours. Left panel indicates Hoechst staining of DNA, middle panel indicates Brachyury, stained with Alexa-488 and right panel indicates Nanog stained with Alexa-594. Scale bar is 25 µm.

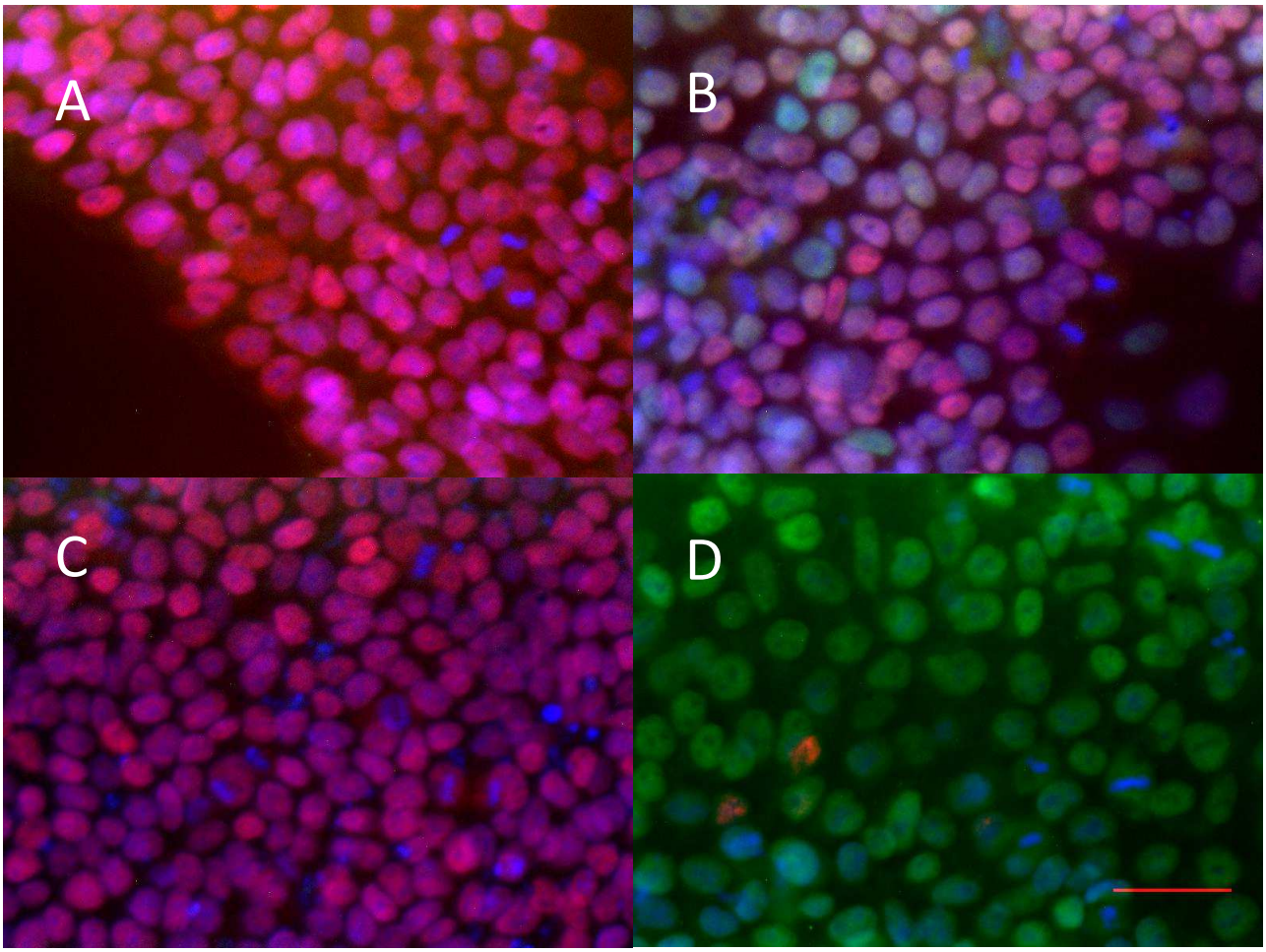

Figure 2.6: Immunostaining image showing cells 20 hours after addition of CHIR, (A) without CHIR and (B) with CHIR and 30 hours after addition of CHIR (C) without CHIR, and (D) with CHIR. Hoechst staining of DNA, middle panel indicates Brachyury, stained with Alexa-488 and right panel indicates Nanog stained with Alexa-594. Scale bar is 25 µm.

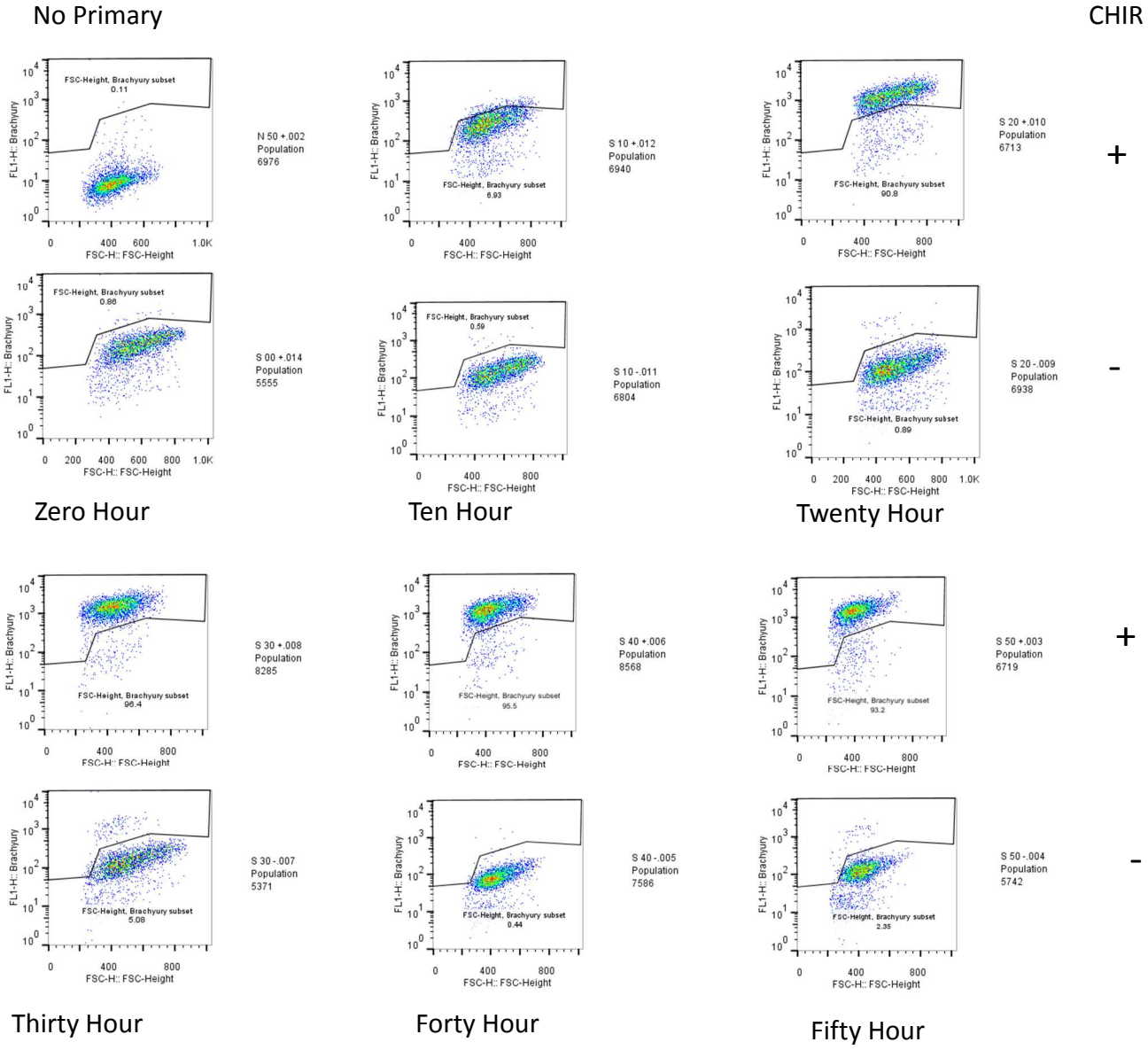

Figure 2.7: Flow cytometric analysis showing that the differentiation to Brachyury occurs uniformly and not sporadically, the entire population of cells migrates from a Brachyury negative to a Brachyury positive state. Similar changes are not observed for the –CHIR conditions. Brachyury-Alexa-633:FL4 is on the vertical axis.

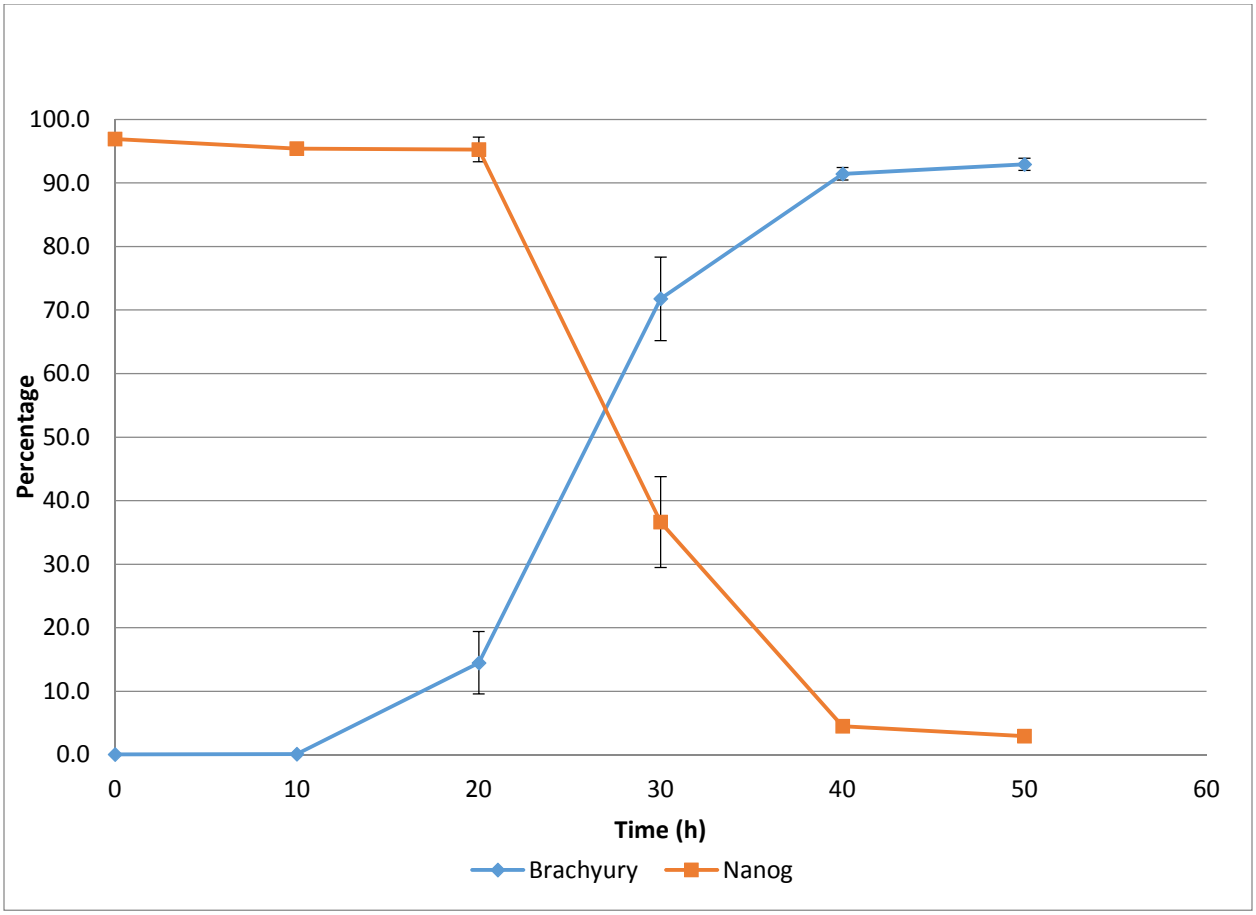

Figure 2.8: Flow cytometric analysis showing percentage of cells that are either Nanog positive or Brachyury positive over time during the CHIR treatment duration

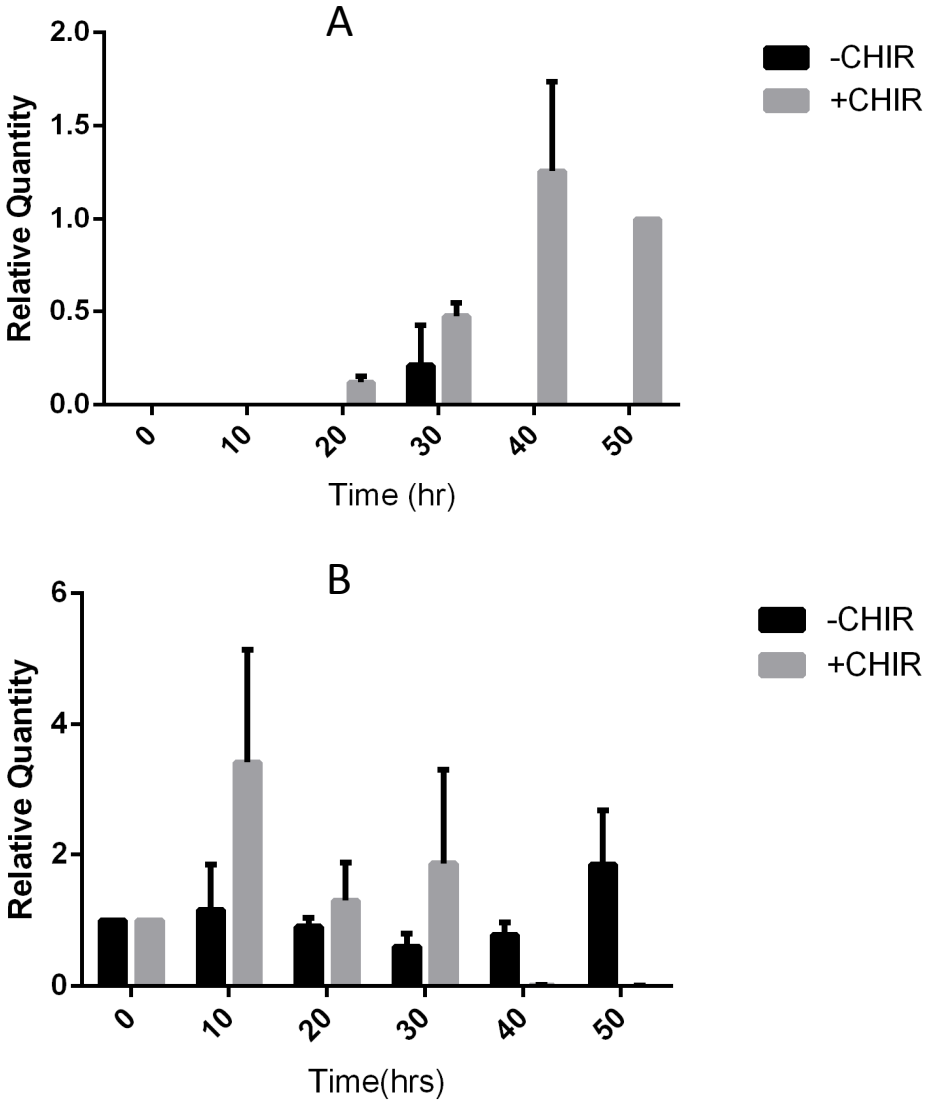

Figure 2.9: Western blotting data for Brachyury (A) and Nanog (B) during 50 hours with CHIR (gray) and without CHIR(black). n=3

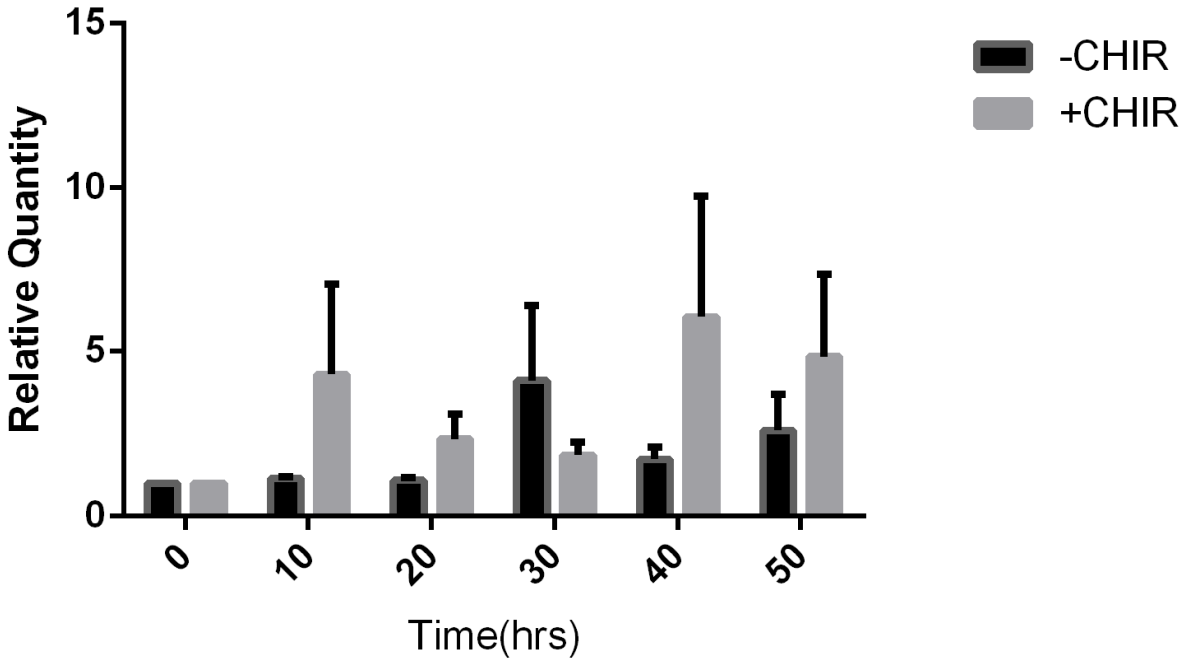

Figure 2.10: Panel showing western blotting quantification for total β-catenin throughout the differentiation process. n=3

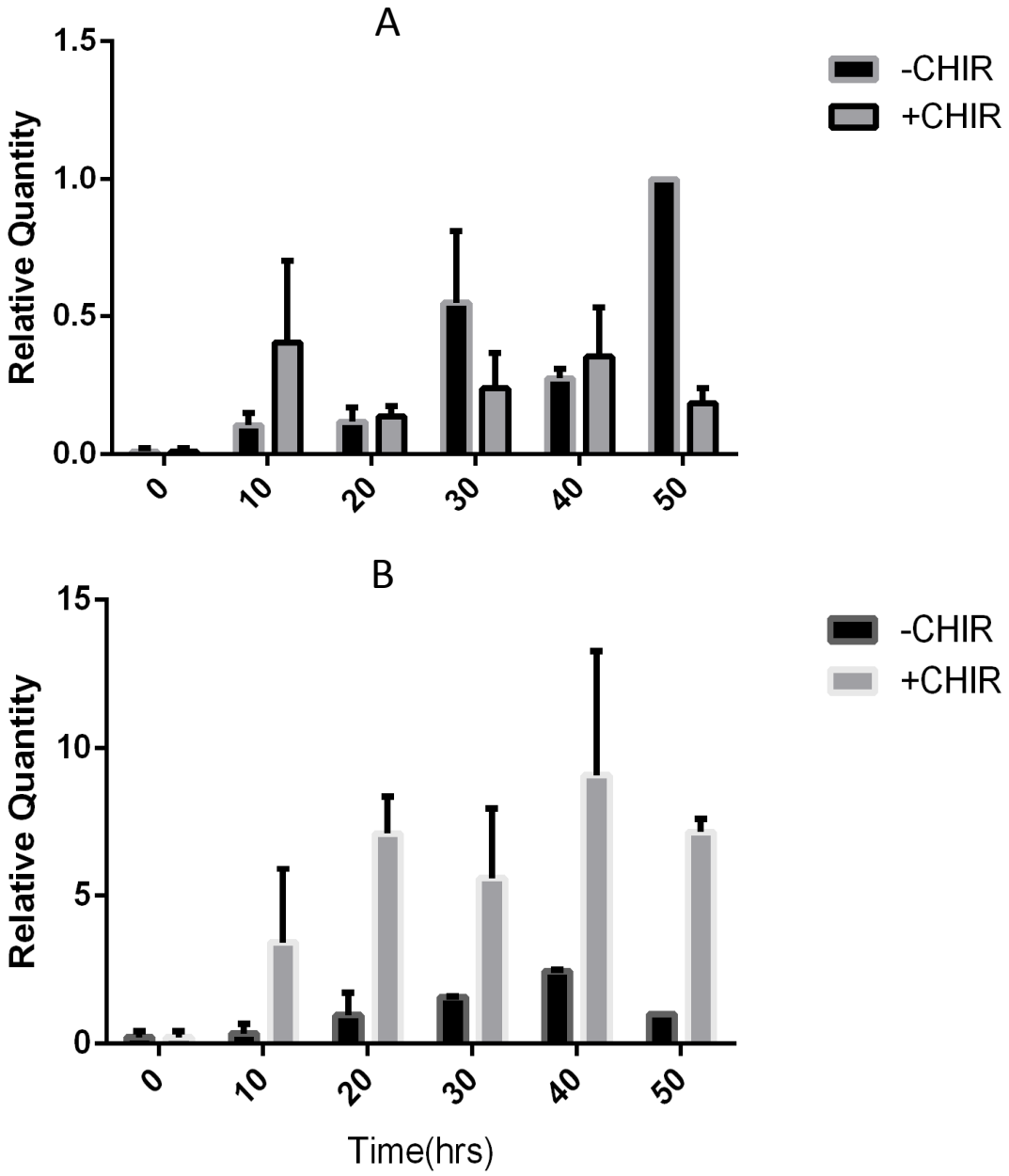

Figure 2.11: Panels showing the quantified amount of (A) Phospho-Ser33/Ser37/Thr41 β-catenin and (B) Phospho-Thr41/Ser45 β-catenin throughout 50 hours of culture and differentiation. N=3

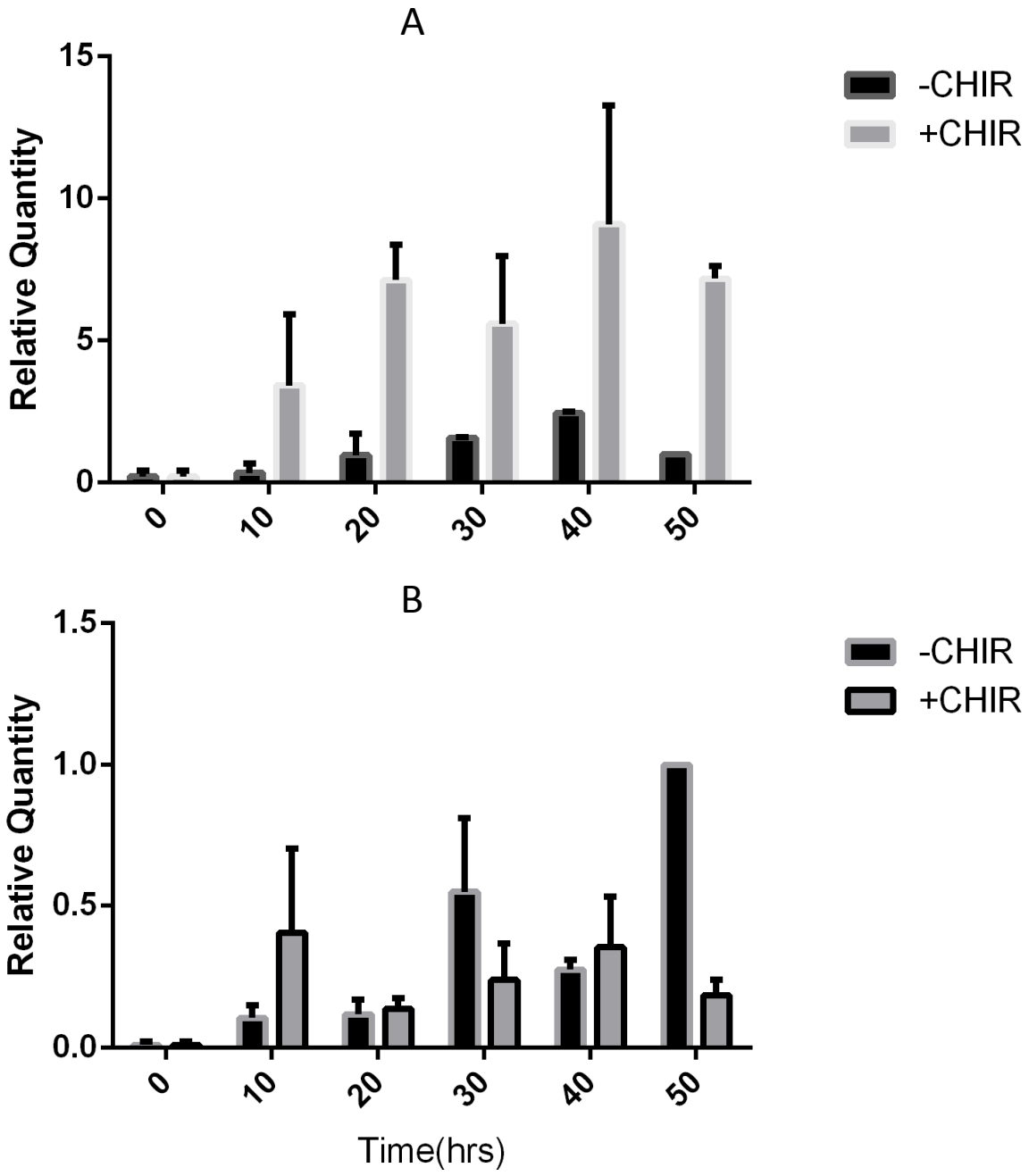

Figure 2.12: Panels showing western blotting data for (A) Phospho-Ser675 β-catenin and (B) Phospho-Ser552 β-catenin over 50 hours of differentiation. n=3

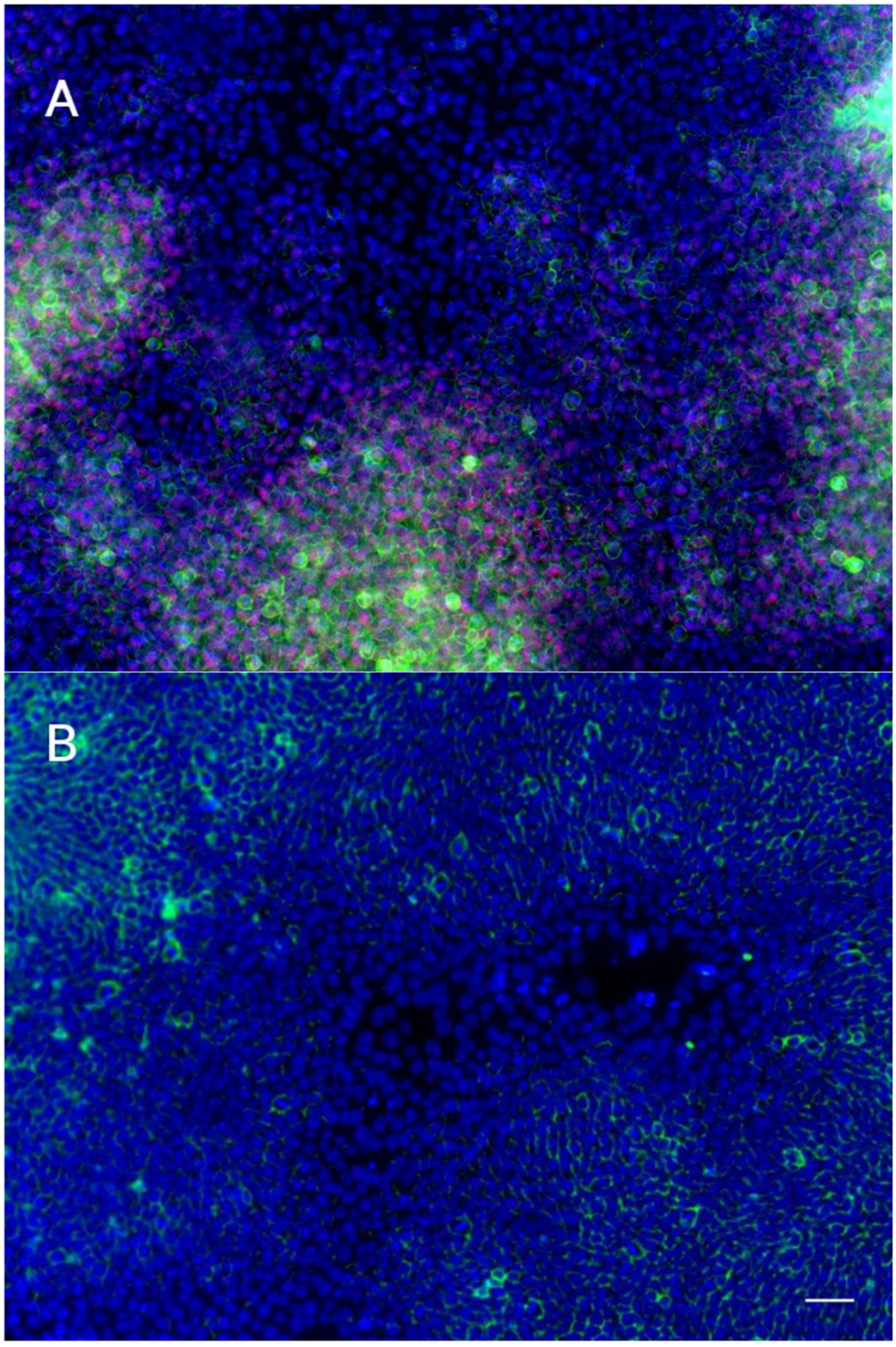

Figure 2.13: Colocalization of Phospho-Ser675 β-catenin and Brachyury in samples (A) treated with CHIR for 30 hours. Control (B) DMSO treatment have limited Phospho-Ser675 β-catenin expression, only in areas of high density. Scale bar is 100 µm.

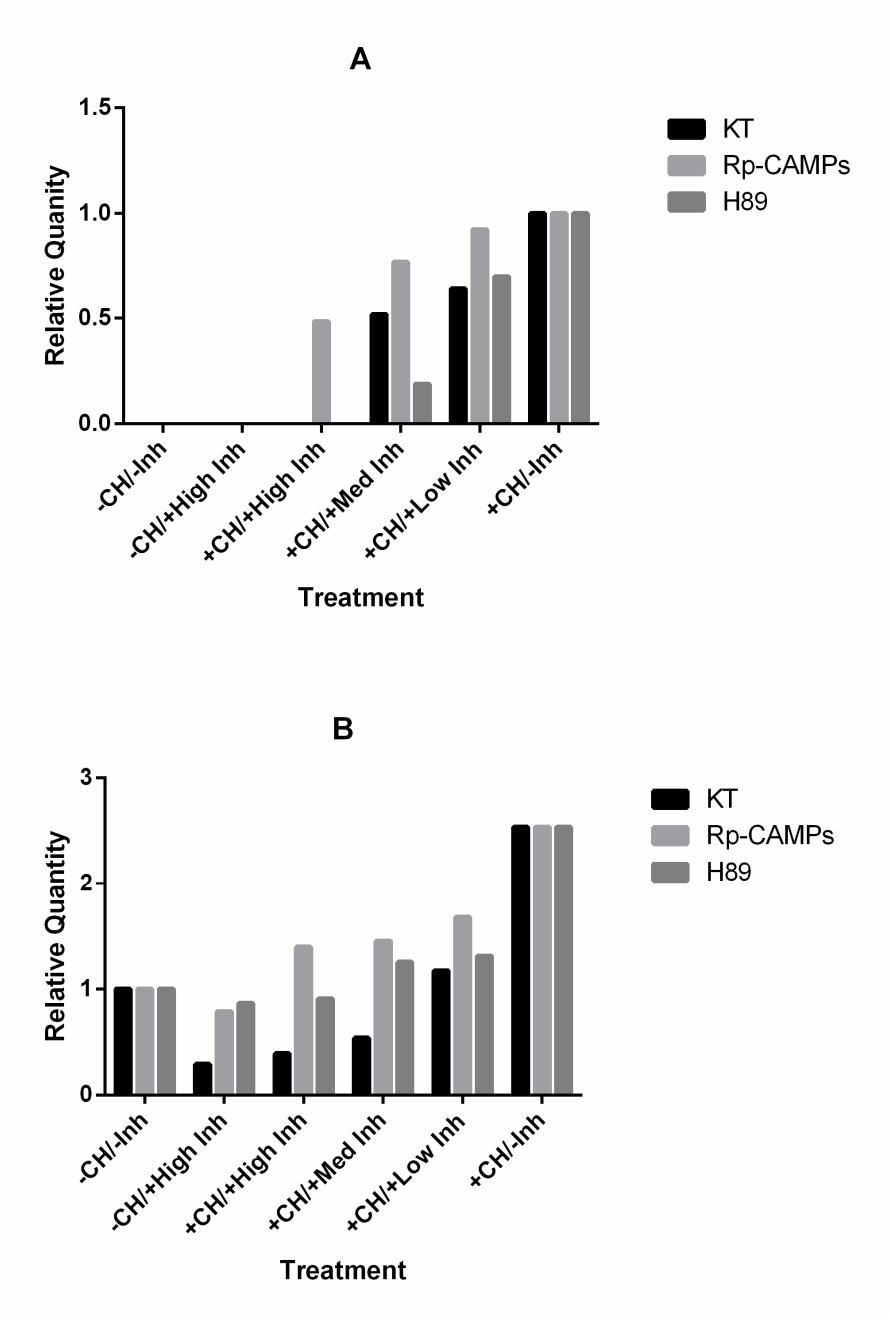

Figure 2.14: Western blotting results on treatment of cells with CHIR and PKA inhibitors for (A) Brachyury and (B) β-catenin

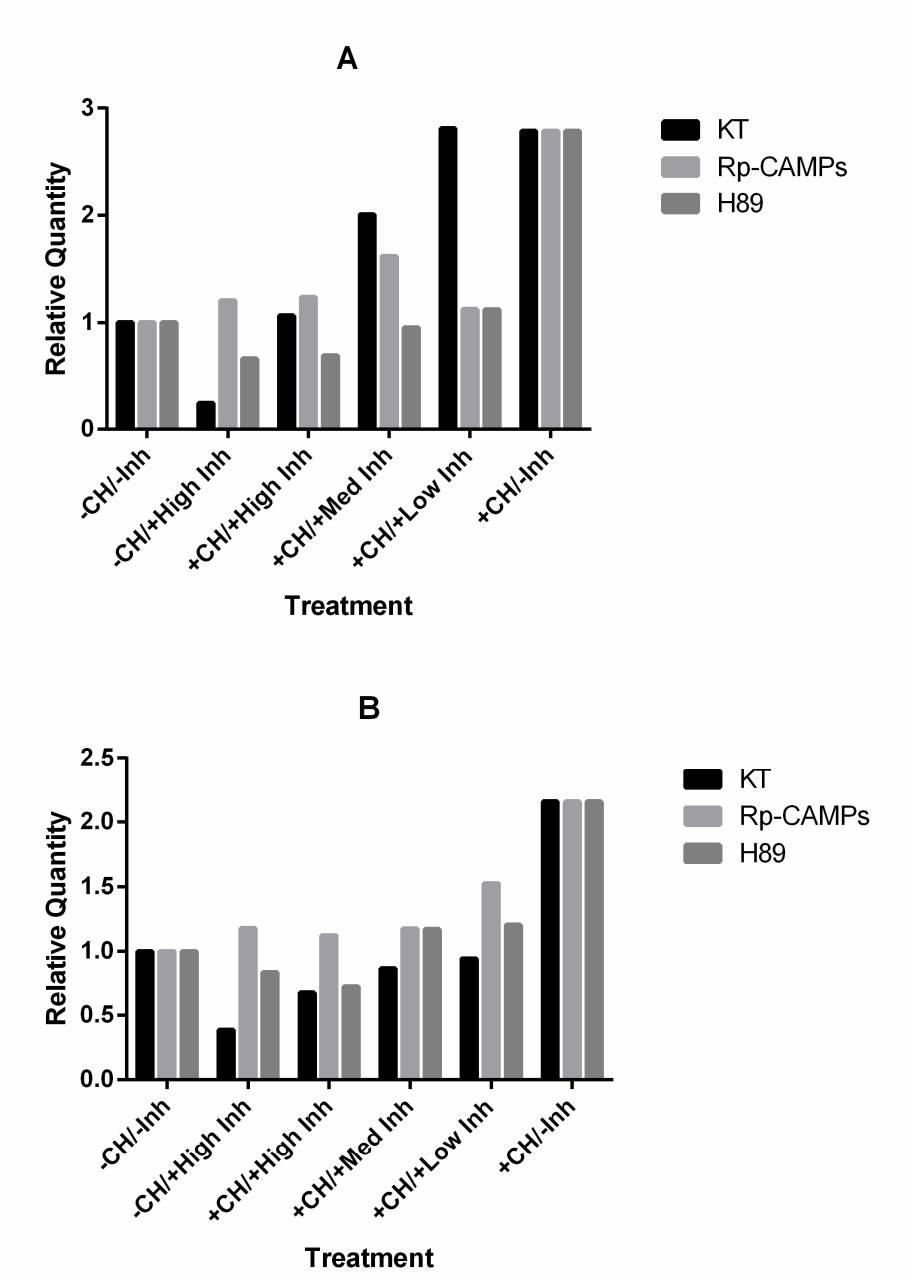

Figure 2.15: Western blotting results on treatment of cells with CHIR and PKA inhibitors for (A) Phospho-Ser552 β-catenin and (B) Phospho-Ser675-β-catenin

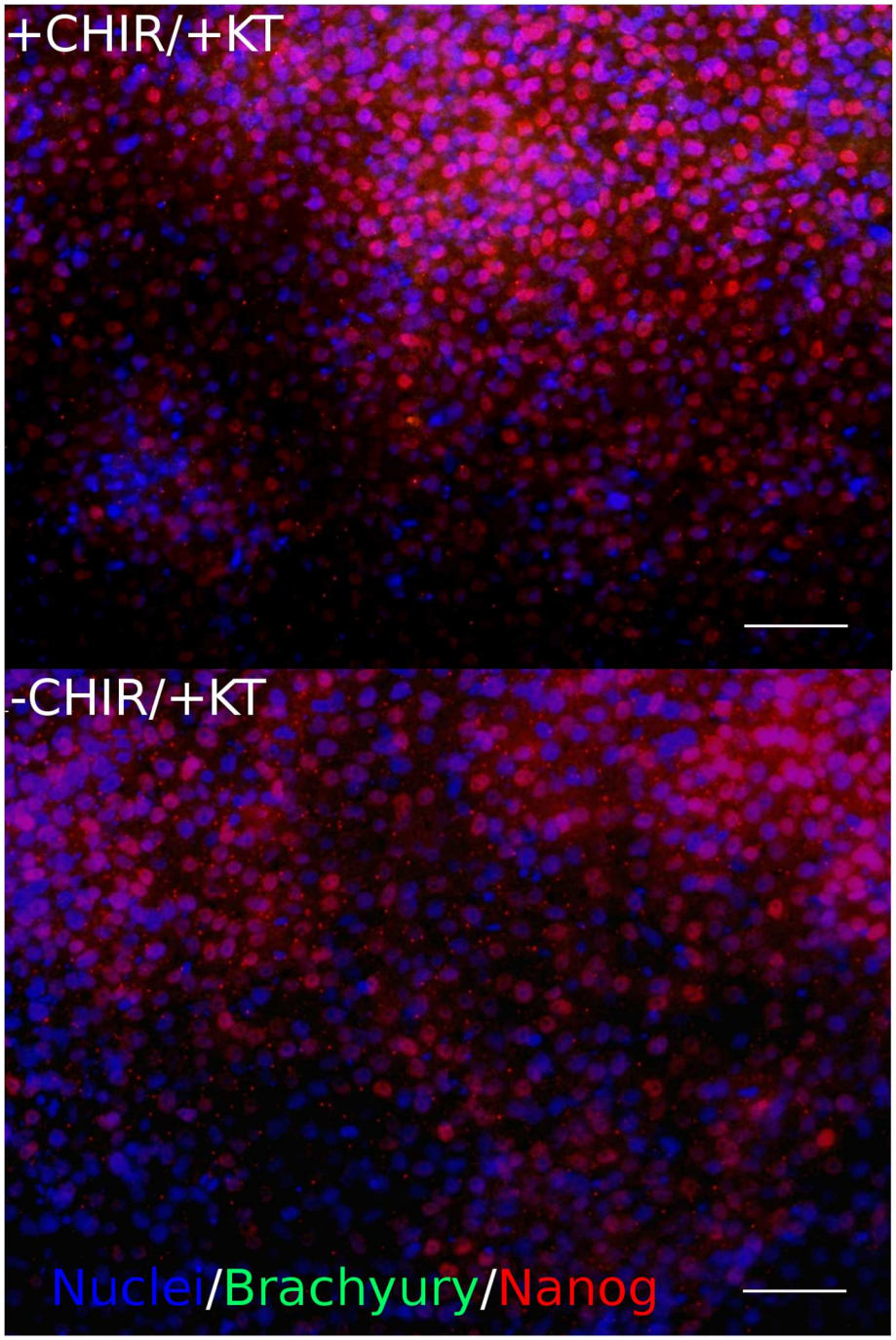

Figure 2.16: Immunostaining results showing cells 30 hours after the addition of KT5720, with and without CHIR. In both cases Brachyury is not seen and many of the cells are Nanog positive. Scale bar is 100 µm.

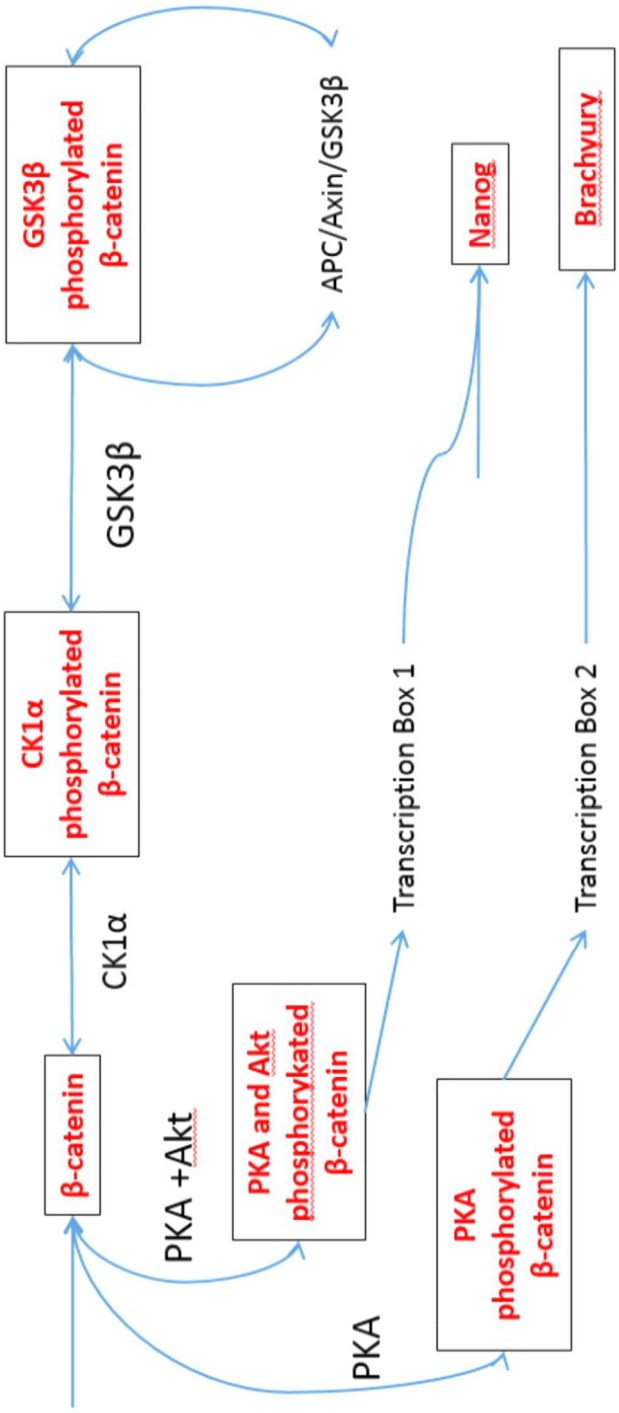

Figure 2.17: Schematic created highlighting the mechanism proposed to explain the results discovered

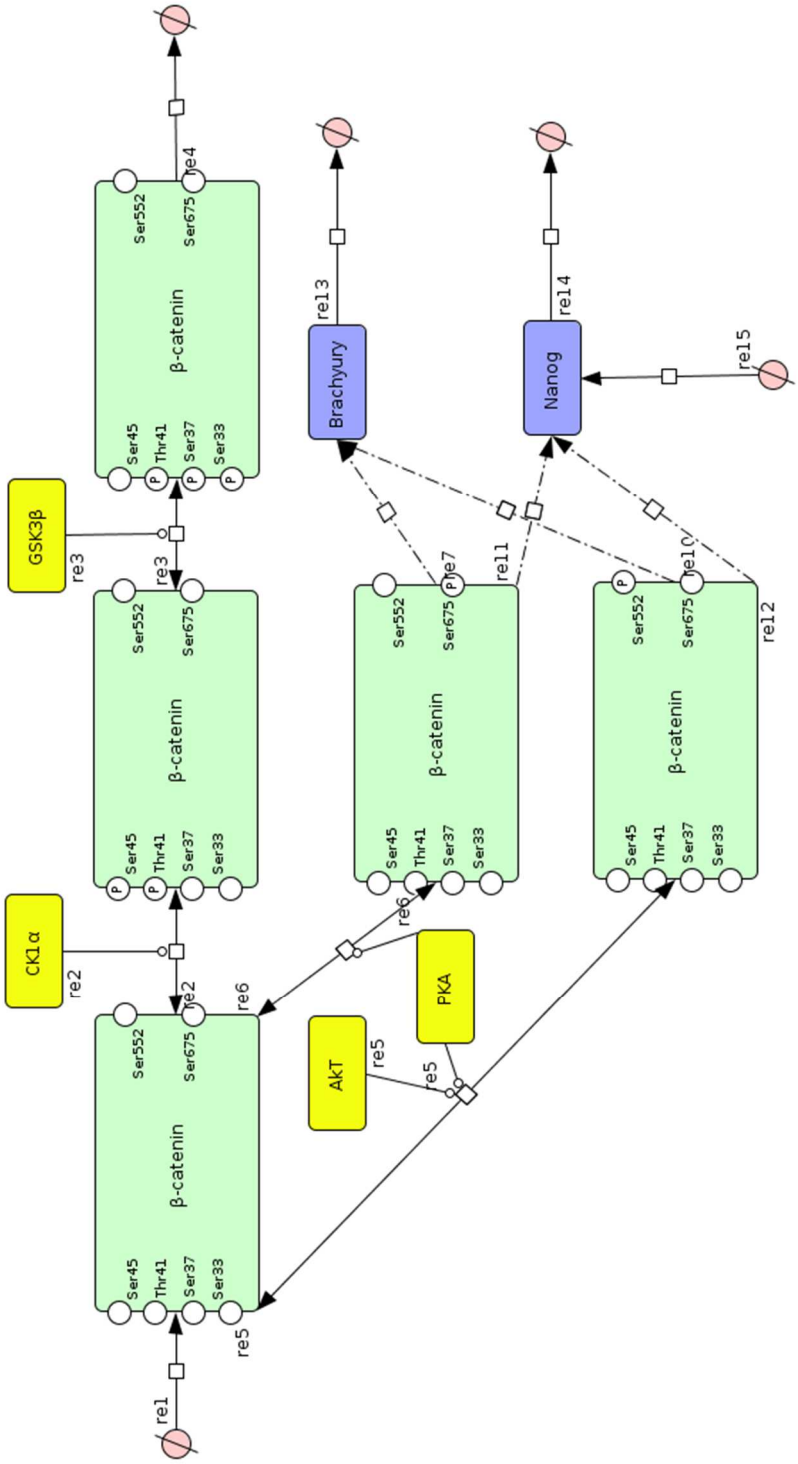

Figure 2.18: Reaction scheme created in CellDesigner to model the mechanism of Wnt signaling in hPSCs

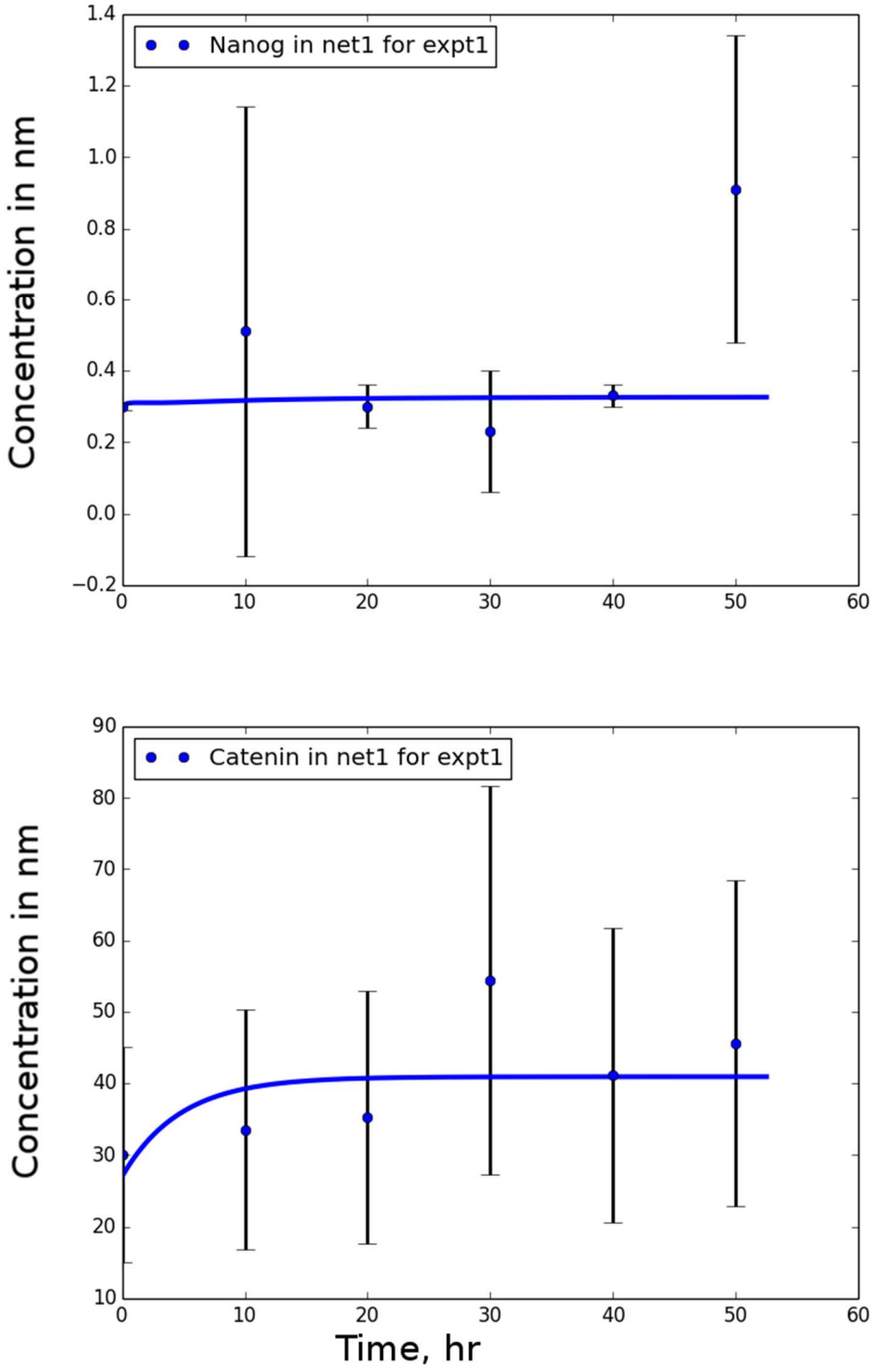

Figure 2.19: Parameter fit results for Nanog and total β-catenin for the DMSO control condition

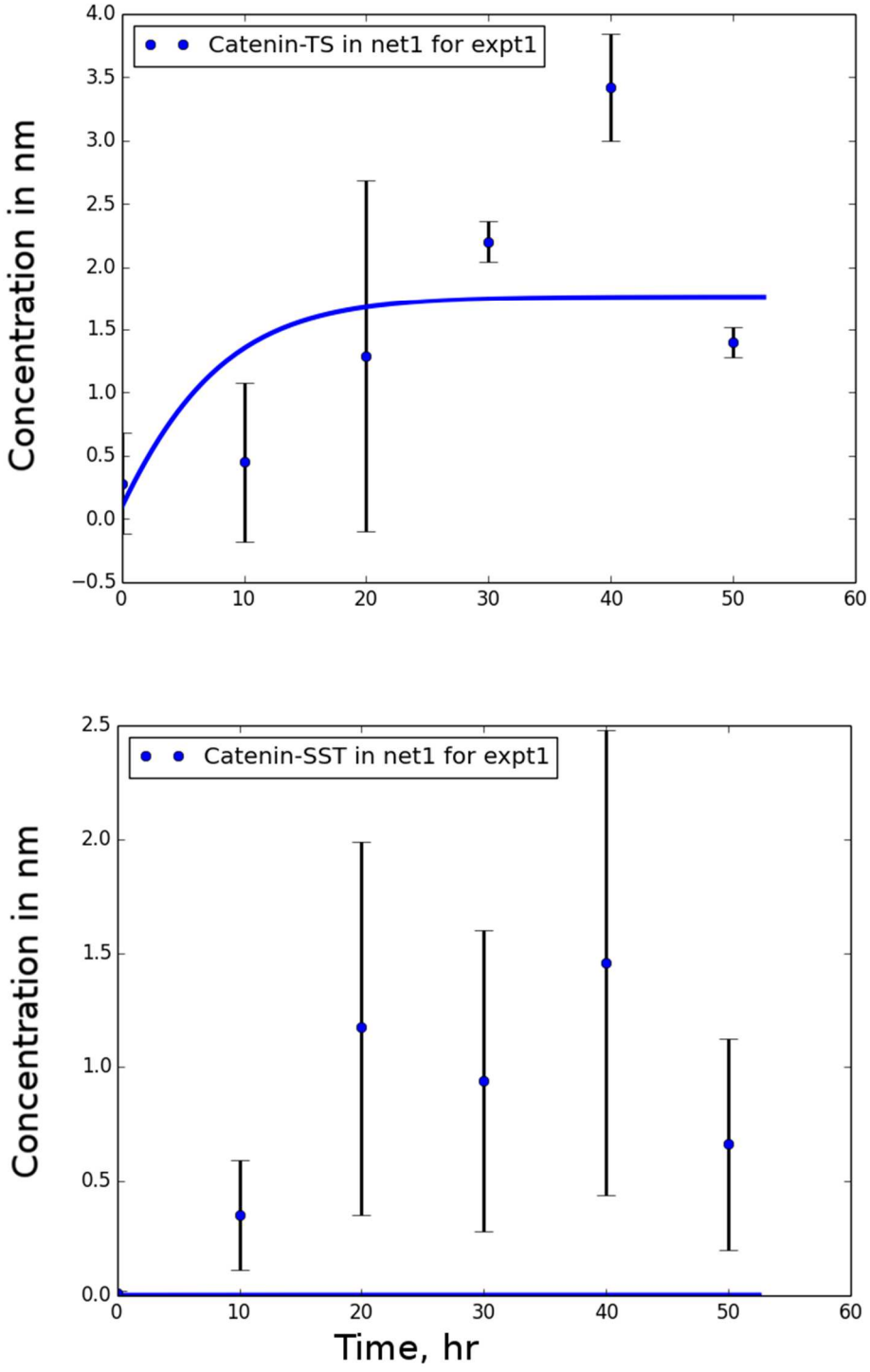

Figure 2.20: Parameter estimation fitting for Phospho-Thr41/Ser45 β-catenin and Phospho-Ser33/Ser37/Thr41 β-catenin for the DMSO control condition

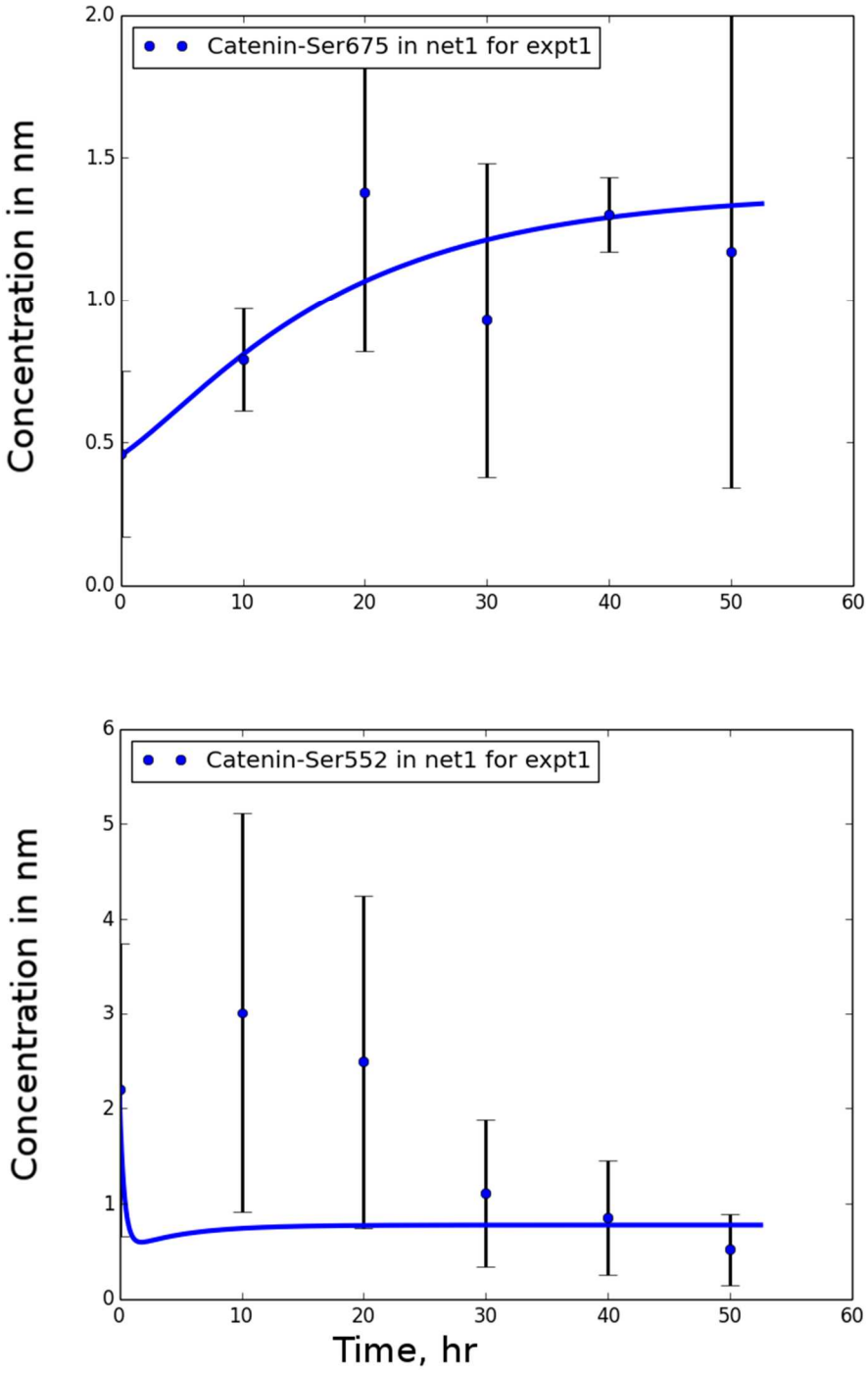

Figure 2.21: Parameter estimation fitting for Phospho-Ser675 β-catenin and Phospho-Ser552 β-catenin for the DMSO control condition

2.5 Tables

Table 1: Results of two-way ANOVA test of Brachyury western blotting values between CHIR treated conditions and DMSO treated conditions for each time point

10 hours	
20 hours	0.356
30 hours	**0.00624**
40 hours	**0.00137**
50 hours	**0**

Table 2: Results of two-way ANOVA test of Brachyury western blotting values between CHIR treated conditions across different time points. The column and row title indicate the time points being compared

	0 hours	**10 hours**	**20 hours**	**30 hours**	**40 hours**
10 hours					
20 hours	0.356	0.356			
30 hours	**0.006243**	**0.00624**	0.122		
40 hours	**0.00137**	**0.00137**	**0.00464**	**0.0146**	
50 hours			**0.000107**	**0.000169**	0.971

Table 3: Results of two-way ANOVA test of Nanog western blotting values between CHIR treated conditions and DMSO treated conditions for each time point

10 hours	0.482
20 hours	0.585
30 hours	0.861
40 hours	0.229
50 hours	0.324

Table 4: Results of two-way ANOVA test of Nanog western blotting values between DMSO treated conditions across different time points. The column and row title indicate the time points being compared

	0 hours	**10 hours**	**20 hours**	**30 hours**	**40 hours**
10 hours	0.0409				
20 hours	0.177	0.459			
30 hours	0.669	0.298	0.252		
40 hours	0.391	0.727	0.843	0.477	
50 hours	0.416	0.568	0.788	0.454	0.714

Table 5: Results of two-way ANOVA test of Nanog western blotting values between CHIR treated conditions across different time points. The column and row title indicate the time points being compared

	0 hours	**10 hours**	**20 hours**	**30 hours**	**40 hours**
10 hours	0.266				
20 hours	0.164	0.559			
30 hours	0.687	0.292	0.236		
40 hours	**6.83E-11**	0.167	**0.0435**	**0.0284**	
50 hours	**2.17E-13**	0.166	**0.0431**	**0.0278**	0.587

Table 6: Results of two-way ANOVA test of β-Catenin western blotting values between CHIR treated conditions and DMSO treated conditions for each time point

10 hours	0.371
20 hours	0.250
30 hours	0.435
40 hours	0.430
50 hours	0.674

Table 7: Results of two-way ANOVA test of β-Catenin western blotting values between DMSO treated conditions across different time points. The column and row title indicate the time points being compared

	0 hours	**10 hours**	**20 hours**	**30 hours**	**40 hours**
10 hours	0.0695				
20 hours	0.350	0.552			
30 hours	0.309	0.328	0.320		
40 hours	0.301	0.348	0.329	0.552	
50 hours	0.395	0.403	0.400	0.614	0.475

Table 8: Results of two-way ANOVA test of β-Catenin western blotting values between CHIR treated conditions across different time points. The column and row title indicate the time points being compared

	0 hours	**10 hours**	**20 hours**	**30 hours**	**40 hours**
10 hours	0.352				
20 hours	0.224	0.562			
30 hours	0.156	0.470	0.632		
40 hours	0.301	0.738	0.424	0.372	
50 hours	0.269	0.900	0.445	0.365	0.808

Table 9: Results of two-way ANOVA test of Phospho-β-Catenin Thr41/Ser45 western blotting values between CHIR treated conditions and DMSO treated conditions for each time point

10 hours	0.330
20 hours	**0.0286**
30 hours	0.198
40 hours	0.283
50 hours	**0.000104**

Table 10: Results of two-way ANOVA test of Phospho-β-Catenin Thr41/Ser45 western blotting values between DMSO treated conditions across different time points. The column and row title indicate the time points being compared

	0 hours	**10 hours**	**20 hours**	**30 hours**	**40 hours**
10 hours	0.785				
20 hours	0.429	0.518			
30 hours	**0.0242**	**0.0624**	0.451		
40 hours	**0.0168**	**0.0312**	0.174	**0.0635**	
50 hours	**0.0633**	0.171	0.920	**0.0311**	**0.0231**

Table 11: Results of two-way ANOVA test of Phospho-β-Catenin Thr41/Ser45 western blotting values between CHIR treated conditions across different time points. The column and row title indicate the time points being compared

	0 hours	**10 hours**	**20 hours**	**30 hours**	**40 hours**
10 hours	0.313				
20 hours	**0.014**	0.257			
30 hours	0.124	0.549	0.539		
40 hours	0.193	0.366	0.679	0.528	
50 hours	**0.00084**	0.230	0.912	0.490	0.688

Table 12: Results of two-way ANOVA test of Phospho-β-Catenin Ser33/Ser37/Thr41 western blotting values between CHIR treated conditions and DMSO treated conditions for each time point

10 hours	0.712
20 hours	0.974
30 hours	0.570
40 hours	0.841
50 hours	0.661

Table 13: Results of two-way ANOVA test of Phospho-β-Catenin Ser33/Ser37/Thr41 western blotting values between DMSO treated conditions across different time points. The column and row title indicate the time points being compared

	0 hours	**10 hours**	**20 hours**	**30 hours**	**40 hours**
10 hours	0.0780				
20 hours	0.0263	0.664			
30 hours	0.0568	0.386	0.551		
40 hours	**0.000977**	0.537	0.934	0.541	
50 hours	**0.000448**	0.610	0.257	0.210	**0.0251**

Table 14: Results of two-way ANOVA test of Phospho-β-Catenin Ser33/Ser37/Thr41 western blotting values between CHIR treated conditions across different time points. The column and row title indicate the time points being compared

	0 hours	**10 hours**	**20 hours**	**30 hours**	**40 hours**
10 hours	0.229				
20 hours	0.136	0.549			
30 hours	0.128	0.590	0.930		
40 hours	0.187	0.662	0.890	0.954	
50 hours	0.242	0.690	0.901	0.961	0.997

Table 15: Results of two-way ANOVA test of Phospho-β-Catenin Ser675 western blotting values between CHIR treated conditions and DMSO treated conditions for each time point

10 hours	0.567
20 hours	0.216
30 hours	0.164
40 hours	0.231
50 hours	0.0257

Table 16: Results of two-way ANOVA test of Phospho-β-Catenin Ser675 western blotting values between DMSO treated conditions across different time points. The column and row title indicate the time points being compared

	0 hours	**10 hours**	**20 hours**	**30 hours**	**40 hours**
10 hours	0.372				
20 hours	0.184	0.645			
30 hours	0.307	0.732	0.963		
40 hours	0.182	0.690	0.934	0.983	
50 hours	**0.0592**	0.304	0.565	0.591	0.497

Table 17: Results of two-way ANOVA test of Phospho-β-Catenin Ser675 western blotting values between CHIR treated conditions across different time points. The column and row title indicate the time points being compared

	0 hours	**10 hours**	**20 hours**	**30 hours**	**40 hours**
10 hours	0.202				
20 hours	**0.0235**	0.330			
30 hours	**0.0420**	0.199	0.509		
40 hours	0.134	0.274	0.466	0.736	
50 hours	**1.44E-05**	**0.0354**	0.218	0.980	0.696

Table 18: Results of two-way ANOVA test of Phospho-β-Catenin Ser552 western blotting values between CHIR treated conditions and DMSO treated conditions for each time point

10 hours	0.431
20 hours	0.0581
30 hours	0.878
40 hours	0.455
50 hours	0.00435

Table 19: Results of two-way ANOVA test of Phospho-β-Catenin Ser552 western blotting values between DMSO treated conditions across different time points. The column and row title indicate the time points being compared

	0 hours	**10 hours**	**20 hours**	**30 hours**	**40 hours**
10 hours	0.358				
20 hours	0.453	0.607			
30 hours	0.460	0.736	0.641		
40 hours	0.801	0.304	0.417	0.497	
50 hours	0.740	**0.0682**	**0.0578**	0.359	0.337

Table 20: Results of two-way ANOVA test of Phospho-β-Catenin Ser552 western blotting values between CHIR treated conditions across different time points. The column and row title indicate the time points being compared

	0 hours	**10 hours**	**20 hours**	**30 hours**	**40 hours**
10 hours	0.233				
20 hours	**0.0788**	0.239			
30 hours	0.2239	0.638	**0.0879**		
40 hours	0.483	0.269	**0.0518**	0.0894	
50 hours	0.226	0.610	**0.0820**	0.853	**0.0651**

Table 21: Parameters used for initial run for the Wnt signaling pathway in hPSC model

Symbol	Parameter	Value	Units
k_1	β-catenin synthesis rate	30	nmol hr^{-1}
K_{CK1}	CK1α Michaelis Menten constant	300	
V_{CK1}	CK1α theoretical maximum velocity	3080	nmol hr^{-1}
K_{GSK3}	GSK3β Michaelis Menten constant	129	
V_{GSK3}	GSK3β Vmax value	9190	nmol hr^{-1}
k_4	β-catenin degradation rate	60	hr^{-1}
K_{PKA}	PKA Michaelis Menten constant	215	
V_{PKA}	PKA theoretical maximum velocity	6130	nmol hr^{-1}
K_{Akt}	AkT Michaelis Menten constant	215	
V_{Akt}	AkT theoretical maximum velocity	6130	nmol hr^{-1}
k_7	Ser675 transcription rate for Brachyury	37	hr^{-1}
k_{10}	Ser552 rate of Brachyury Transcription	37	hr^{-1}
k_{11}	Ser675 Transcription rate for Nanog	37	hr^{-1}
k_{12}	Ser552 transcription rate of Nanog	37	hr^{-1}
k_{13}	Brachyury destruction rate constant	2.60	hr^{-1}
k_{14}	Nanog destruction rate	2.60	hr^{-1}
k_{15}	Nanog synthesis rate	1.30	nmol hr^{-1}
x_{PKA}	Portion of PKA phosphorylated β-catenin phosphorylated at Ser675	0.25	

2.6 Equations

Equation 1: Michealis-Menten reaction equation

$$V_0 = \frac{V_{max}S}{K_m + S}$$

Equation 2: Change in K_m with inhibitor added

$$K'_m = K_m(1 + \frac{[I]}{K_i})$$

Equation 3: Calculation of K_i from IC50 using expression by Brandt et al[79]

$$K_i = \frac{IC_{50}}{(\frac{S}{K_m} + 1)}$$

Equation 4: Equation for reaction re1 indicating the zeroth order synthesis of β-catenin

$$v_1 = k_1$$

Equation 5: Equation for reaction re2, indicating the phosphorylation of β-catenin at Thr41/Ser45 by CK1α. $V_{CK1\alpha}$ and $K_{CK1\alpha}$, are the maximum velocity and Michaelis Menten constant for CK1α, the species s2 represents β-catenin

$$v_2 = \frac{V_{CK1\alpha}(s2)}{K_{CK1\alpha} + (s2)}$$

Equation 6: Equation for reaction re3, indicating the phosphorylation of β-catenin at Ser33/Ser37/Thr41 by GSK3β. $V_{GSK3\beta}$ and $K_{GSK3\beta}$, are the maximum velocity and Michaelis Menten constant for GSK3β, the species s8 represents Phospho-β-catenin Thr41/Ser45

$$v_3 = \frac{V_{\mathrm{GSK3\beta}}(s8)}{K_{\mathrm{GSK3\beta}} + (s8)}$$

Equation 7: Equation for re4, the first order ubiquitination and destruction of Phospho-β-catenin Ser33/Ser37/Thr41, the species s11 represents Phospho-β-catenin Ser33/Ser37/Thr41

$$v_4 = k_4 * (s11)$$

Equation 8: Equation for re5, the formation of Phospho-β-catenin Ser552 through phosphorylation of β-catenin by both Akt and PKA. V_{PKA} and K_{PKA}, are the maximum velocity and Michaelis Menten constant for PKA, V_{Akt} and K_{Akt}, are the maximum velocity and Michaelis Menten constant for Akt, and the term x_{PKA} represents the proportion of PKA phosophorylated β-catenin phosphorylated at Ser675

$$v_5 = (1 - x_{PKA})\frac{V_{\mathrm{PKA}}(s2)}{K_{\mathrm{PKA}} + (s2)} + \frac{V_{\mathrm{Akt}}(s2)}{K_{\mathrm{Akt}} + (s2)}$$

Equation 9: Equation for re6, the formation of Phospho-β-catenin Ser552 through phosphorylation of β-catenin by both Akt and PKA. V_{PKA} and K_{PKA}, are the maximum velocity and Michaelis Menten constant for PKA. The term x_{PKA} represents the proportion of PKA phosophorylated β-catenin phosphorylated at Ser675.

$$v_6 = x_{PKA}\frac{V_{\mathrm{PKA}}(s2)}{K_{\mathrm{PKA}} + (s2)}$$

Equation 10: Equation for re7, the transcription of Brachyury through the action of Phospho-β-catenin Ser675. The species s14 represents Phospho-β-catenin Ser675

$$v_7 = k_7 * (s14)$$

Equation 11: Equation for re11, the transcription of Nanog through the action of Phospho-β-catenin Ser675. The species s14 represents Phospho-β-catenin Ser675

$$v_8 = k_8 * (s14)$$

Equation 12: Equation for re10, the transcription of Brachyury through the action of Phospho-β-catenin Ser552. The species s13 represents Phospho-β-catenin Ser552

$$v_{10} = k_{10} * (s13)$$

Equation 13: Equation for re12, the transcription of Nanog through the action of Phospho-β-catenin Ser552. The species s13 represents Phospho-β-catenin Ser552

$$v_{12} = k_{12} * (s13)$$

Equation 14: Equation for re13, representing the destruction of Brachyury. The species s15 represents Brachyury

$$v_{13} = k_{13} * (s15)$$

Equation 15: Equation for re15 representing the zeroth order synthesis of Nanog

$$v_{15} = k_{15}$$

Equation 16: Equation for re14, representing the destruction of Nanog. The species s16 represents Nanog

$$v_{14} = k_{14} * (s16)$$

2.7 References

1. Thomson JA, Itskovitz-Eldor J, Shapiro SS, Waknitz MA, Swiergiel JJ, Marshall VS, et al. Embryonic stem cell lines derived from human blastocysts. Science. 1998;282(5391):1145-7. doi: 10.1126/science.282.5391.1145. PubMed PMID: WOS:000076887700056.

2. Feinberg AP. Phenotypic plasticity and the epigenetics of human disease. Nature. 2007;447(7143):433-40. doi: 10.1038/nature05919. PubMed PMID: WOS:000246693100039.

3. Lindvall O, Kokaia Z, Martinez-Serrano A. Stem cell therapy for human neurodegenerative disorders - how to make it work. Nature Medicine. 2004;10(7):S42-S50. doi: 10.1038/nm1064. PubMed PMID: WOS:000223202100007.

4. Murry CE, Keller G. Differentiation of embryonic stem cells to clinically relevant populations: Lessons from embryonic development. Cell. 2008;132(4):661-80. doi: 10.1016/j.cell.2008.02.008. PubMed PMID: WOS:000253817900024.

5. Liras A. Future research and therapeutic applications of human stem cells: general, regulatory, and bioethical aspects. Journal of Translational Medicine. 2010;8. doi: 10.1186/1479-5876-8-131. PubMed PMID: WOS:000285884900001.

6. Takahashi K, Tanabe K, Ohnuki M, Narita M, Ichisaka T, Tomoda K, et al. Induction of pluripotent stem cells from adult human fibroblasts by defined factors. Cell. 2007;131(5):861-72. doi: 10.1016/j.cell.2007.11.019. PubMed PMID: WOS:000251800900010.

7. Yu JY, Vodyanik MA, Smuga-Otto K, Antosiewicz-Bourget J, Frane JL, Tian S, et al. Induced pluripotent stem cell lines derived from human somatic cells. Science. 2007;318(5858):1917-20. doi: 10.1126/science.1151526. PubMed PMID: WOS:000251786600057.

8. Stadtfeld M, Nagaya M, Utikal J, Weir G, Hochedlinger K. Induced Pluripotent Stem Cells Generated Without Viral Integration. Science. 2008;322(5903):945-9. doi: 10.1126/science.1162494. PubMed PMID: WOS:000260674100048.

9. Yu JY, Hu KJ, Smuga-Otto K, Tian SL, Stewart R, Slukvin, II, et al. Human Induced Pluripotent Stem Cells Free of Vector and Transgene Sequences. Science. 2009;324(5928):797-801. doi: 10.1126/science.1172482. PubMed PMID: WOS:000265832400050.

10. Yu JY, Thomson JA. Pluripotent stem cell lines. Genes & Development. 2008;22(15):1987-97. doi: 10.1101/gad.1689808. PubMed PMID: WOS:000258117500001.

11. Stocum DL, Zupanc GKH. Stretching the Limits: Stem Cells in Regeneration Science. Developmental Dynamics. 2008;237(12):3648-71. doi: 10.1002/dvdy.21774. PubMed PMID: WOS:000261679300019.

12. Hanna J, Wernig M, Markoulaki S, Sun CW, Meissner A, Cassady JP, et al. Treatment of sickle cell anemia mouse model with iPS cells generated from autologous skin. Science. 2007;318(5858):1920-3. doi: 10.1126/science.1152092. PubMed PMID: WOS:000251786600058.

13. Moretti A, Bellin M, Welling A, Jung CB, Lam JT, Bott-Flugel L, et al. Patient-Specific Induced Pluripotent Stem-Cell Models for Long-QT Syndrome. New England Journal of Medicine. 2010;363(15):1397-409. doi: 10.1056/NEJMoa0908679. PubMed PMID: WOS:000282575100005.

14. Egashira T, Yuasa S, Suzuki T, Aizawa Y, Yamakawa H, Matsuhashi T, et al. Disease characterization using LQTS-specific induced pluripotent stem cells. Cardiovascular Research. 2012;95(4):419-29. doi: 10.1093/cvr/cvs206. PubMed PMID: WOS:000307781800007.

15. Park SW, Koh YJ, Jeon J, Cho YH, Jang MJ, Kang Y, et al. Efficient differentiation of human pluripotent stem cells into functional CD34(+) progenitor cells by combined modulation of the MEK/ERK and BMP4 signaling pathways. Blood. 2010;116(25):5762-72. doi: 10.1182/blood-201004-280719. PubMed PMID: WOS:000285383900042.

16. Yamanaka S, Blau HM. Nuclear reprogramming to a pluripotent state by three approaches. Nature. 2010;465(7299):704-12. doi: 10.1038/nature09229. PubMed PMID: WOS:000278551800032.

17. Evans MJ, Kaufman MH. ESTABLISHMENT IN CULTURE OF PLURIPOTENTIAL CELLS FROM MOUSE EMBRYOS. Nature. 1981;292(5819):154-6. doi: 10.1038/292154a0. PubMed PMID: WOS:A1981LW55000043.

18. Odorico JS, Kaufman DS, Thomson JA. Multilineage differentiation from human embryonic stem cell lines. Stem Cells. 2001;19(3):193-204. doi: 10.1634/stemcells.19-3-193. PubMed PMID: WOS:000168989700003.

19. Ludwig TE, Levenstein ME, Jones JM, Berggren WT, Mitchen ER, Frane JL, et al. Derivation of human embryonic stem cells in defined conditions. Nature Biotechnology. 2006;24(2):185-7. doi: 10.1038/nbt1177. PubMed PMID: WOS:000235232300034.

20. Chen GK, Gulbranson DR, Hou ZG, Bolin JM, Ruotti V, Probasco MD, et al. Chemically defined conditions for human iPSC derivation and culture. Nature Methods. 2011;8(5):424-U76. doi: 10.1038/nmeth.1593. PubMed PMID: WOS:000289987100021.

21. Chen GK, Hou ZG, Gulbranson DR, Thomson JA. Actin-Myosin Contractility Is Responsible for the Reduced Viability of Dissociated Human Embryonic Stem Cells. Cell Stem Cell. 2010;7(2):240-8. doi: 10.1016/j.stem.2010.06.017. PubMed PMID: WOS:000281107400015.

22. Waddington C. The Strategy of the Genes: Allen and Unwin; 1957.

23. Metallo CM, Mohr JC, Detzel CJ, de Pablo JJ, Van Wie BJ, Palecek SP. Engineering the stem cell microenvironment. Biotechnology Progress. 2007;23(1):18-23. doi: 10.1021/bp060350a. PubMed PMID: WOS:000243927600003.

24. Azarin SM, Palecek SP. Development of scalable culture systems for human embryonic stem cells. Biochemical Engineering Journal. 2010;48(3):378-84. doi: 10.1016/j.bej.2009.10.020. PubMed PMID: WOS:000276121700011.

25. Logan CY, Nusse R. The Wnt signaling pathway in development and disease. Annual Review of Cell and Developmental Biology. 2004;20:781-810. doi: 10.1146/annurev.cellbio.20.010403.113126. PubMed PMID: WOS:000225318200029.

26. Tian Y, Cohen ED, Morrisey EE. The Importance of Wnt Signaling in Cardiovascular Development. Pediatric Cardiology. 2010;31(3):342-8. doi: 10.1007/s00246-009-9606-z. PubMed PMID: WOS:000275464400005.

27. Katoh M. WNT signaling in stem cell biology and regenerative medicine. Current Drug Targets. 2008;9(7):565-70. doi: 10.2174/138945008784911750. PubMed PMID: WOS:000257455900006.

28. Jiang J, Struhl G. Regulation of the Hedgehog and Wingless signalling pathways by the F-box/WD40-repeat protein Slimb. Nature. 1998;391(6666):493-6. doi: 10.1038/35154. PubMed PMID: WOS:000071701800052.

29. Morin PJ, Sparks AB, Korinek V, Barker N, Clevers H, Vogelstein B, et al. Activation of beta-catenin-Tcf signaling in colon cancer by mutations in beta-catenin or APC. Science. 1997;275(5307):1787-90. doi: 10.1126/science.275.5307.1787. PubMed PMID: WOS:A1997WP05600040.

30. Borowiak M, Maehr R, Chen SB, Chen AE, Tang WP, Fox JL, et al. Small Molecules Efficiently Direct Endodermal Differentiation of Mouse and Human Embryonic Stem Cells. Cell Stem Cell. 2009;4(4):348-58. doi: 10.1016/j.stem.2009.01.014. PubMed PMID: WOS:000265162700011.

31. Hernandez AR, Klein AM, Kirschner MW. Kinetic Responses of beta-Catenin Specify the Sites of Wnt Control. Science. 2012;338(6112):1337-40. doi: 10.1126/science.1228734. PubMed PMID: WOS:000311991200065.

32. Nusse R. Wnt signaling and stem cell control. Cell Research. 2008;18(5):523-7. doi: 10.1038/cr.2008.47. PubMed PMID: WOS:000256409000001.

33. Willert K, Brown JD, Danenberg E, Duncan AW, Weissman IL, Reya T, et al. Wnt proteins are lipid-modified and can act as stem cell growth factors. Nature. 2003;423(6938):448-52. doi: 10.1038/nature01611. PubMed PMID: WOS:000183012000044.

34. Yost C, Torres M, Miller RR, Huang E, Kimelman D, Moon RT. The axis-inducing activity, stability, and subcellular distribution of beta-catenin is regulated in Xenopus embryos by glycogen synthase kinase 3. Genes & Development. 1996;10(12):1443-54. doi: 10.1101/gad.10.12.1443. PubMed PMID: WOS:A1996UU11700002.

35. Korinek V, Barker N, Morin PJ, vanWichen D, deWeger R, Kinzler KW, et al. Constitutive transcriptional activation by a beta-catenin-Tcf complex in APC(-/-) colon carcinoma. Science. 1997;275(5307):1784-7. doi: 10.1126/science.275.5307.1784. PubMed PMID: WOS:A1997WP05600039.

36. He XC, Yin T, Grindley JC, Tian Q, Sato T, Tao WA, et al. PTEN-deficient intestinal stem cells initiate intestinal polyposis. Nature Genetics. 2007;39(2):189-98. doi: 10.1038/ng1928. PubMed PMID: WOS:000244063900016.

37. Sato N, Meijer L, Skaltsounis L, Greengard P, Brivanlou AH. Maintenance of pluripotency in human and mouse embryonic stem cells through activation of Wnt signaling by a

pharmacological GSK-3-specific inhibitor. Nature Medicine. 2004;10(1):55-63. doi: 10.1038/nm979. PubMed PMID: WOS:000187743600039.

38. Nakanishi M, Kurisaki A, Hayashi Y, Warashina M, Ishiura S, Kusuda-Furue M, et al. Directed induction of anterior and posterior primitive streak by Wnt from embryonic stem cells cultured in a chemically defined serum-free medium. Faseb Journal. 2009;23(1):114-22. doi: 10.1096/fj.08-111203. PubMed PMID: WOS:000262095500014.

39. Piccolo S, Agius E, Leyns L, Bhattacharyya S, Grunz H, Bouwmeester T, et al. The head inducer Cerberus is a multifunctional antagonist of Nodal, BMP and Wnt signals. Nature. 1999;397(6721):707-10. PubMed PMID: WOS:000078840100053.

40. Glinka A, Wu W, Delius H, Monaghan AP, Blumenstock C, Niehrs C. Dickkopf-1 is a member of a new family of secreted proteins and functions in head induction. Nature. 1998;391(6665):357-62. PubMed PMID: WOS:000071604200044.

41. Behrens J, Jerchow BA, Wurtele M, Grimm J, Asbrand C, Wirtz R, et al. Functional interaction of an axin homolog, conductin, with beta-catenin, APC, and GSK3 beta. Science. 1998;280(5363):596-9. doi: 10.1126/science.280.5363.596. PubMed PMID: WOS:000073242100049.

42. Moon RT, Brown JD, Torres M. WNTs modulate cell fate and behavior during vertebrate development. Trends in Genetics. 1997;13(4):157-62. doi: 10.1016/s0168-9525(97)01093-7. PubMed PMID: WOS:A1997WQ96900010.

43. Huber O, Korn R, McLaughlin J, Ohsugi M, Herrmann BG, Kemler R. Nuclear localization of beta-catenin by interaction with transcription factor LEF-1. Mechanisms of Development. 1996;59(1):3-10. doi: 10.1016/0925-4773(96)00597-7. PubMed PMID: WOS:A1996VL19200001.

44. Martin BL, Kimelman D. Brachyury establishes the embryonic mesodermal progenitor niche. Genes & Development. 2010;24(24):2778-83. doi: 10.1101/gad.1962910. PubMed PMID: WOS:000285331800010.

45. Suemori H, Tada T, Torii R, Hosoi Y, Kobayashi K, Imahie H, et al. Establishment of embryonic stem cell lines from cynomolgus monkey blastocysts produced by IVF or ICSI. Developmental Dynamics. 2001;222(2):273-9. doi: 10.1002/dvdy.1191. PubMed PMID: WOS:000171382200013.

46. Itskovitz-Eldor J, Schuldiner M, Karsenti D, Eden A, Yanuka O, Amit M, et al. Differentiation of human embryonic stem cells into embryoid bodies comprising the three embryonic germ layers. Molecular Medicine. 2000;6(2):88-95. PubMed PMID: WOS:000087110900003.

47. Amit M, Carpenter MK, Inokuma MS, Chiu CP, Harris CP, Waknitz MA, et al. Clonally derived human embryonic stem cell lines maintain pluripotency and proliferative potential for prolonged periods of culture. Developmental Biology. 2000;227(2):271-8. doi: 10.1006/dbio.2000.9912. PubMed PMID: WOS:000165363000003.

48. Lu J, Hou RH, Booth CJ, Yang SH, Snyder M. Defined culture conditions of human embryonic stem cells. Proceedings of the National Academy of Sciences of the United States of

America. 2006;103(15):5688-93. doi: 10.1073/pnas.0601383103. PubMed PMID: WOS:000236896200012.

49. Tsutsui H, Valamehr B, Hindoyan A, Qiao R, Ding XT, Guo SL, et al. An optimized small molecule inhibitor cocktail supports long-term maintenance of human embryonic stem cells. Nature Communications. 2011;2. doi: 10.1038/ncomms1165. PubMed PMID: WOS:000288225700017.

50. Nichols J, Silva J, Roode M, Smith A. Suppression of Erk signalling promotes ground state pluripotency in the mouse embryo. Development. 2009;136(19):3215-22. doi: 10.1242/dev.038893. PubMed PMID: WOS:000269568400002.

51. Ying QL, Wray J, Nichols J, Batlle-Morera L, Doble B, Woodgett J, et al. The ground state of embryonic stem cell self-renewal. Nature. 2008;453(7194):519-U5. doi: 10.1038/nature06968. PubMed PMID: WOS:000256023700042.

52. Dravid G, Ye ZH, Hammond H, Chen GB, Pyle A, Donovan P, et al. Defining the role of Wnt/beta-catenin signaling in the survival, proliferation, and self-renewal of human embryonic stem cells. Stem Cells. 2005;23(10):1489-501. doi: 10.1634/stemcells.2005-0034. PubMed PMID: WOS:000233708700008.

53. Singh AM, Reynolds D, Cliff T, Ohtsuka S, Mattheyses AL, Sun YH, et al. Signaling Network Crosstalk in Human Pluripotent Cells: A Smad2/3-Regulated Switch that Controls the Balance between Self-Renewal and Differentiation. Cell Stem Cell. 2012;10(3):312-26. doi: 10.1016/j.stem.2012.01.014. PubMed PMID: WOS:000301466500012.

54. Davidson KC, Adams AM, Goodson JM, McDonald CE, Potter JC, Berndt JD, et al. Wnt/beta-catenin signaling promotes differentiation, not self-renewal, of human embryonic stem cells and is repressed by Oct4. Proceedings of the National Academy of Sciences of the United States of America. 2012;109(12):4485-90. doi: 10.1073/pnas.1118777109. PubMed PMID: WOS:000301712600033.

55. Lian XJ, Hsiao C, Wilson G, Zhu KX, Hazeltine LB, Azarin SM, et al. Robust cardiomyocyte differentiation from human pluripotent stem cells via temporal modulation of canonical Wnt signaling. Proceedings of the National Academy of Sciences of the United States of America. 2012;109(27):E1848-E57. doi: 10.1073/pnas.1200250109. PubMed PMID: WOS:000306641100009.

56. Dietrich C, Scherwat J, Faust D, Oesch F. Subcellular localization of beta-catenin is regulated by cell density. Biochemical and Biophysical Research Communications. 2002;292(1):195-9. doi: 10.1006/bbrc.2002.6625. PubMed PMID: WOS:000174591900030.

57. Steel MD, Puddicombe SM, Hamilton LM, Powell RM, Holloway JW, Holgate ST, et al. beta-Catenin/T-cell factor-mediated transcription is modulated by cell density in human bronchial epithelial cells. International Journal of Biochemistry & Cell Biology. 2005;37(6):1281-95. doi: 10.1016/j.biocel.2004.12.010. PubMed PMID: WOS:000228373300014.

58. Murray AJ. Pharmacological PKA Inhibition: All May Not Be What It Seems. Science Signaling. 2008;1(22). doi: 10.1126/scisignal.122re4. PubMed PMID: WOS:000207493000003.

59. Lochner A, Moolman JA. The many faces of H89: A review. Cardiovascular Drug Reviews. 2006;24(3-4):261-74. doi: 10.1111/j.1527-3466.2006.00261.x. PubMed PMID: WOS:000243022600007.

60. Lee E, Salic A, Kruger R, Heinrich R, Kirschner MW. The roles of APC and axin derived from experimental and theoretical analysis of the Wnt pathway. Plos Biology. 2003;1(1):116-32. doi: 10.1371/journal.pbio.0000010. PubMed PMID: WOS:000188834700019.

61. Kofahl B, Wolf J. Mathematical modelling of Wnt/beta-catenin signalling. Biochemical Society Transactions. 2010;38:1281-5. doi: 10.1042/bst0381281. PubMed PMID: WOS:000283039000020.

62. Cho K-H, Baek S, Sung M-H. Wnt pathway mutations selected by optimal beta-catenin signaling for tumorigenesis. Febs Letters. 2006;580(15):3665-70. doi: 10.1016/j.febslet.2006.05.053. PubMed PMID: WOS:000238691600015.

63. Wawra C, Kuehl M, Kestler HA. Extended analyses of the Wnt/beta-catenin pathway: Robustness and oscillatory behaviour. Febs Letters. 2007;581(21):4043-8. doi: 10.1016/j.febslet.2007.07.043. PubMed PMID: WOS:000249077900025.

64. Goentoro L, Kirschner MW. Evidence that Fold-Change, and Not Absolute Level, of beta-Catenin Dictates Wnt Signaling. Molecular Cell. 2009;36(5):872-84. doi: 10.1016/j.molcel.2009.11.017. PubMed PMID: WOS:000272965400019.

65. Kruger R, Heinrich R. Model reduction and analysis of robustness for the Wnt/beta-catenin signal transduction pathway. Genome informatics International Conference on Genome Informatics. 2004;15(1):138-48. PubMed PMID: MEDLINE:15712117.

66. Mirams GR, Byrne HM, King JR. A multiple timescale analysis of a mathematical model of the Wnt/beta-catenin signalling pathway. Journal of Mathematical Biology. 2010;60(1):131-60. doi: 10.1007/s00285-009-0262-y. PubMed PMID: WOS:000269854000007.

67. van Leeuwen IMM, Mirams GR, Walter A, Fletcher A, Murray P, Osborne J, et al. An integrative computational model for intestinal tissue renewal. Cell Proliferation. 2009;42(5):617-36. doi: 10.1111/j.1365-2184.2009.00627.x. PubMed PMID: WOS:000269674100005.

68. van Leeuwen IMM, Byrne HM, Jensen OE, King JR. Elucidating the interactions between the adhesive and transcriptional functions of beta-catenin in normal and cancerous cells. Journal of theoretical biology. 2007;247(1):77-102. doi: 10.1016/j.jtbi.2007.01.019. PubMed PMID: MEDLINE:17382967.

69. Tan CW, Gardiner BS, Hirokawa Y, Layton MJ, Smith DW, Burgess AW. Wnt Signalling Pathway Parameters for Mammalian Cells. Plos One. 2012;7(2). doi: 10.1371/journal.pone.0031882. PubMed PMID: WOS:000302873700114.

70. Mazemondet O, John M, Leye S, Rolfs A, Uhrmacher AM. Elucidating the Sources of beta-Catenin Dynamics in Human Neural Progenitor Cells. Plos One. 2012;7(8). doi: 10.1371/journal.pone.0042792. PubMed PMID: WOS:000307733800028.

71. MacLean AL, Rosen Z, Byrne HM, Harrington HA. Parameter-free methods distinguish Wnt pathway models and guide design of experiments. Proceedings of the National Academy of

Sciences of the United States of America. 2015;112(9):2652-7. doi: 10.1073/pnas.1416655112. PubMed PMID: WOS:000350224900031.

72. Matsuoka Y, Funahashi A, Ghosh S, Kitano H. Modeling and Simulation Using CellDesigner. Transcription Factor Regulatory Networks: Methods and Protocols. 2014;1164:121-45. doi: 10.1007/978-1-4939-0805-9_11. PubMed PMID: WOS:000338027600012.

73. Gutenkunst RN, Waterfall JJ, Casey FP, Brown KS, Myers CR, Sethna JP. Universally sloppy parameter sensitivities in systems biology models. Plos Computational Biology. 2007;3(10):1871-8. doi: 10.1371/journal.pcbi.0030189. PubMed PMID: WOS:000251113500007.

74. Myers CR, Gutenkunst RN, Sethna JP. Python unleashed on systems biology. Computing in Science & Engineering. 2007;9(3):34-7. doi: 10.1109/mcse.2007.60. PubMed PMID: WOS:000245668100007.

75. Tan CW, Gardiner BS, Hirokawa Y, Smith DW, Burgess AW. Analysis of Wnt signaling beta-catenin spatial dynamics in HEK293T cells. Bmc Systems Biology. 2014;8. doi: 10.1186/1752-0509-8-44. PubMed PMID: WOS:000334805600001.

76. Schmalhofer O, Brabletz S, Brabletz T. E-cadherin, beta-catenin, and ZEB1 in malignant progression of cancer. Cancer and Metastasis Reviews. 2009;28(1-2):151-66. doi: 10.1007/s10555-008-9179-y. PubMed PMID: WOS:000264476600013.

77. Dorsky RI, Moon RT, Raible DW. Control of neural crest cell fate by the Wnt signalling pathway. Nature. 1998;396(6709):370-3. doi: 10.1038/24620. PubMed PMID: WOS:000077204000050.

78. Lutolf MP, Gilbert PM, Blau HM. Designing materials to direct stem-cell fate. Nature. 2009;462(7272):433-41. doi: 10.1038/nature08602. PubMed PMID: WOS:000272144200031.

79. Brandt RB, Laux JE, Yates SW. CALCULATION OF INHIBITOR KI AND INHIBITOR TYPE FROM THE CONCENTRATION OF INHIBITOR FOR 50-PERCENT INHIBITION FOR MICHAELIS-MENTEN ENZYMES. Biochemical Medicine and Metabolic Biology. 1987;37(3):344-9. doi: 10.1016/0885-4505(87)90046-6. PubMed PMID: WOS:A1987H942200010.

3 Vocal Fold Epithelia Differentiation on Transwell® Inserts

3.1 Introduction

3.1.1 Vocal Fold Epithelial Tissue

The human vocal fold has been described as a “human instrument” [1] due to the remarkable range of sounds produced and its small size compared to larger orchestral instruments. In order to produce sounds, an instrument requires three components, a sound source that vibrates in the air, a resonator that increases the strength of the fundamental frequency of the vibration and an orifice that transfers the sound to the free air space [1]. The vocal folds act as the vibrating sound source for the production of a fundamental frequency. They consist of two small specialized tissues that produce sound by rapidly oscillating as they come into contact and separate from each other. The change in length of the vocal fold create multiple frequencies that are perceived as pitch. This relationship between airflow and speech has been characterized, at least since the time of Aristotle (circa 384 – 322 BC) [2].

The vocal folds are composed of many different tissue types, epithelium, lamina propria, striated muscle, nerves, vasculature and cartilage. The striated muscle give the vocal folds the ability to oscillate and create a fundamental frequency, the epithelium, protects the musculature, and other tissues from injury. The vocal folds are prone to injury from various sources, including environmental irritants [3-5] like airborne pollutants (inhaled smoke), surgical procedures [6] and vibratory trauma [7] from use. The epithelia which sits over the muscle and the lamina propria forms a physical cellular barrier against injury through the formation of tight cellular junctions.

Recently, researchers have identified associations between epithelial disruption and vocal fold injury [8]. Since voice disorders are estimated to affect up to 9% of Americans [9], research into the primary protective mechanism, vocal fold epithelia is warranted.

Epithelial cells are cells that line the cavities in the body and cover flat surfaces. In particular the luminal surface (exposed to the air) of vocal folds is covered in multiple layers of closely packed stratified squamous (square shaped) cells [6, 8, 10]. Human vocal fold epithelium typically consists of between 5 – 10 epithelial cell layers [11]. The layers of the squamous cells in the membranous vocal fold epithelium can be divided into basal and luminal layers, each of which expresses a different cytokeratin marker protein [12, 13]. Cytokeratin 14 is located in the basal layer, while Cytokeratin 13 is localized to the luminal layer. The vocal fold epithelia experiences continuous turnover [14], with estimates of continuous turnover time being about 4 days in murine models [15]. Despite the turnover, epithelial cell layers serve to create a barrier to protect the tissue underneath. This barrier is maintained through the presence of tight cellular junctions between the epithelial cells.

Cellular junctions are protein complexes between cells that facilitate adherence between either a pair of cells or between a cell and a basement membrane. This adherence helps in the maintenance of tissue integrity and protects against injury [16]. Protein complexes called “tight junctions” are the primary occluding junction of the vocal fold epithelium and serve to bind adjacent epithelial cells [17]. The presence of these tight junctions creates a selectively permeable barrier to ion and compound flow in the transport through the epithelia. Disruptions of these tight junctions are critical in the protection of vocal folds from chemical injury. The

selective permeability of ions across the vocal fold epithelia causes resistance to electrical current across the barrier. This Transepithelial Electrical Resistance (TEER) can be measured and used to quantify the tightness of vocal fold epithelia [18, 19]. Paracellular fluxes measure the permeability of non-ionic molecules like fluorescein through the membrane [20]. Paracellular fluxes and TEER are typically correlated with each other, epithelia displaying high TER typically will show lower fluxes.

The measurement of TEER is convenient and provides instantaneous feedback of the barrier tightness. Paracellular fluxes indicate barrier tightness over extended periods of time [21]. Measurement of TER of vocal fold epithelia has been performed using the Ussig chamber [19] and dissected animal vocal folds[18]. The process of dissection and sample transfer from the slaughterhouse could cause differences in measured barrier tightness and may not be indicative of barrier tightness in human systems due to differences in species. The generation and characterization of human vocal fold epithelia from human pluripotent stem cells (hPSCs) could help further the understanding of human vocal fold epithelia.

3.1.2 Vocal Fold Epithelial Differentiation

The removal of epithelial cells from the larynx creates an unacceptable risk to vocal fold function. Impairment of vocal fold function is associated with significant economic, social and psychological costs [22]. The Thibeault lab in association with the Palecek lab developed an *in vitro* stem cell derived model for vocal folds [13] by building on prior research done in both labs. Previous work by Chen et al, 2010 indicated that vocal fold fibroblasts, which are found in the lamina propria, demonstrated phenotypes in 3D models that were more consistent with vocal

fold tissue than fibroblasts grown in monolayers [23]. Work done by Metallo et al in the Palecek group indicated that human pluripotent stem cells (hPSCs) can be differentiated into epithelial progenitors through the systematic treatment with all-trans Retinoic acid (RA)[24]. Furthermore, the epithelial progenitors can be cultured to form epidermal progenitors that are capable of forming stratified dermal epithelium. Stratification is induced by culturing the epidermal progenitors on a collagen gel embedded with primary derived foreskin fibroblasts at the air liquid interface (ALI)[25]. Leydon et al developed an analogous process using epithelial progenitors derived through RA treatment followed by co-culture with Vocal Fold Fibroblasts (VFF) embedded in a collagen gel at the ALI [13].

This protocol was used to probe the role of Epidermal Growth Factor (EGF) in the healing of injured vocal fold tissue in a study performed by Liliana Palencia and me [26]. In this study, the 3D vocal fold epithelium construct was differentiated using hPSCs and then serum starved overnight to eliminate growth factors in serum. A scratch wound, approximately 500 µm was created using a 100 µL pipette. The wound closure rates were observed under four conditions – without any exogenous compounds or growth factors, EGF supplemented media, with Gefitinib, an EGF receptor inhibitor and with both the EGF and Gefitinib. Wound repair was significantly accelerated with exogenous EGF treatment, but slowed down by Gefitinib addition, indicating an EGF receptor mediated wound healing mechanism. This type of study would have been very difficult to do using dissected tissue due to the limited viability of the dissected tissue. However, barrier resistance cannot be adequately characterized using the collagen gel setup.

In order to create an Air Liquid Interface (ALI), the collagen gel is typically deposited on an insert, with the addition of media on the baso-lateral side of the insert, with the apical side exposed to air (Figure 3.1). When both chambers are filled with media, electrodes can be used to measure the resistance across the membrane. Therefore, when cells are grown on the insert, electrical measurements can be conducted with minimal interference to the tissue. However, the embedding of fibroblasts within the collagen gel causes the contraction of the gel and consequently reduces the surface coverage of the insert causing gaps allowing easy flow of ions and disrupting electrical measurements. In order to eliminate this error, I differentiated hPSCs into vocal fold epithelia by seeding hPSCs on the inserts and coculturing with vocal fold fibroblasts on the baso-lateral side of the insert.

3.1.3 Aim of the current study

This study identified the factors required for differentiation of hPSCs into vocal fold epithelia on a Transwell® insert. The inserts can be either made of polycarbonate or polyester and are available with pore sizes ranging from 0.4 µm to 8 µm. Previous attempts of epidermal stratification were performed where partially differentiated cells were sub-cultured on to the insert for further differentiation and stratification [27]. The requirement for subculture for further purification is present in our epidermal differentiation protocol. However, the subculture step typically causes a certain amount of cell death and sub-confluent cell growth [28]. For this study, I observed that the epithelial cell progenitors were plated on to the collagen gel-fibroblast matrix at high density [13]. This coupled with the poor detachment and singularization capacity of the epithelial progenitors implied that seeding hPSCs on the inserts and differentiating them was a better method. This allowed for the growth of a tissue undisturbed by enzymatic passaging.

Prior work on the Blood Brain Barrier system in the Palecek & Shusta labs [29] had used polystyrene inserts with a 0.4 μm pore size. Prior work showing that epithelial differentiation outcomes were driven by seeding density [28] implied initial experiments with different hPSC seeding densities and expansion times prior to treatment with all-trans Retinoic acid treatment for epithelial differentiation induction. After this initial screening, polycarbonate inserts and other porosities were tried as well. Finally, the differentiated tissue was subjected to histological analysis and permeability analysis using Sodium Fluorescein.

3.2 Results

3.2.1 Stepwise differentiation scheme adapted from collagen-matrix system

Briefly, the vocal fold epithelia (VFE) differentiation scheme established by Thibeault coworkers [13] involves the preparation of a collagen matrix embedded with vocal fold fibroblast (VFF), in which the fibroblasts are harvested using trypsin and dissolved in the collagen. This is then allowed to grow for a week. During this time, the collagen contracts. Simultaneously, hPSCs are seeded onto Matrigel at a density between 30k and 100k cells/cm2 and expanded for 2 days before treatment with 1 μM all-trans Retinoic acid for 7 days. The differentiated epithelial progenitors are then harvested with dispase and seeded onto the contracted collagen gel. For 2 days, both the base of the gel and the top are treated with FAD media, followed by 14 days of culture at the air liquid interface, only the base is treated with FAD media. It was hoped that differentiating the hPSCs on the insert will eliminate the subculture step required.

Figure 3.2 shows the adaptation of this scheme for hPSCs plated on the insert. Based on work standardizing the epithelial differentiation protocol by Selekman et al [28], it was decided that

the RA treatment duration would be 5 days long following a 4 day expansion. A longer expansion time was chosen as higher purities of K18 positive progenitors have been reported in this condition. The VFFs were thawed and cultured for a week before being subcultured onto the plate prior to the transfer of the inserts with the differentiated cells. Based on the assumption that a strong barrier post stratification develops from a strong barrier pre-stratification, the transepithelial electrical resistance (TEER) was used to evaluate the various experimental conditions.

3.2.2 Initial Seeding Density

Prior work [28] indicated that a higher starting density of hPSCs prior to epithelial progenitor differentiation would lead to higher purity, but not yield of epidermal keratinocytes. Higher purity of keratinocyte progenitors imply a stronger barrier. Contaminating cell types were often fibroblasts and less commonly neural cells (only at lower densities), neither of which are barrier forming cells. To test this hypothesis, hPSCs seeded at 50k cells/cm^2 and 100k cells/cm^2 were expanded for 4 days, and differentiated using at-RA for 5 days. TEER measurements were made every day.

After one day, there is barrier formation in both the density conditions, however, as expected the 100 cells/cm^2 condition shows higher TEER values throughout all 5 days of differentiation, as seen in Figure 3.3. Both of these experiments were conducted on 3 µm pore polyester inserts. The porosity of the 0.4 µm polyester insert was expected to be lower than that of the 3 µm insert, therefore the porosity was tested next.

3.2.3 Porosity

Figure 3.4 shows the TEER values obtained for 100k cells/cm^2, expanded for 4 days and then differentiated for 5 days. The smaller pore size showed that there was a decrease in TEER over the duration of at-RA treatment (Figure 3.4B). This was considered to be unexpected, however, on further inspection, it was found that the pore density of the 0.4 µm pore insert is about 100 times higher than the equivalent 3 µm pore, indicating, perhaps a cause for the lower barrier.

At this point, it was noticed that neither the 3 µm pore insert nor the 0.4 µm pore insert were capable of supporting an epithelial barrier past the progenitor differentiation stage. Hence, different insert materials were then tried, 3 µm pore size polyester inserts were tried along with 3 µm pore size polycarbonate inserts.

3.2.4 Insert Material

Figure 3.5A indicates that the polycarbonate insert was capable of supporting much higher barrier resistance than the equivalent polyester insert. With the polycarbonate insert, the resistance values seen approached those for stratified epidermal tissue [27]. With the ability to differentiate VFE tissue on inserts, it was now possible to scale up or scale down this system for various different experiments, therefore scalability was tested using 1.2 cm^2 inserts and 4.5 cm^2 inserts.

3.2.5 Scalability

Figure 3.6 shows that regardless of the diameter of the insert used, 1.2 cm^2 for (A), and 4.5 cm^2 for (B), the TEER trend remained consistent. The final TEER values for both samples are

statistically insignificant from each other (p-value=0.83). Further smaller inserts could be tested, as these may be useful for large scale screening experiments.

3.2.6 Histology

Figure 3.7 shows hematoxylin and eosin staining for the VFE tissue differentiated in a 4.5 cm^2 polycarbonate 3 μm pore insert with 15 days of stratification at the ALI. The thickness of the tissue formed was about 35 μm, which was significantly thinner than the differentiated tissue in Leydon et al [13]. This epithelial thickness was also small compared to measurements in patient samples [30]. This lowered thickness may be due to several factors, including the altered extracellular matrix conditions, or altered growth kinetics on the insert.

3.2.7 Barrier Permeability

Finally, the barrier permeability was tested for differentiations on 1.2 cm^2 polycarbonate and polyester inserts with 3 μm porosity. It was seen that the polycarbonate insert showed a barrier permeability of about 8.14 ± 1.95 nm/s with 10 μM Sodium Fluorescein, and the polyester insert had a permeability of 6330 ± 1449 nm/s. Compared to previous *ex vivo* studies performed with dextran [12, 18, 31](a larger, therefore more impermeable molecule), the presence of a barrier with Sodium fluorescein was deemed extremely significant.

3.3 Conclusions and Future directions

In this chapter, a protocol for the differentiation of hPSCs to vocal fold epithelia on Transwell® inserts has been established. hPSCs seeded at 100k cells/cm^2 on 3 μm pore size polycarbonate inserts were allowed to expand for 4 days in mTeSR1, prior to the initiation of differentiation

through the addition of retinoic acid. Retinoic acid treatment was continued for 5 days, during which time the electrical barrier rose to around 600 Ω cm^2. Following which the inserts were transferred onto wells coated with vocal fold fibroblasts and both the apical and basolateral side of the insert were filled with FAD media for 2 days. The media was then removed from the apical side, thus the differentiating tissue was effectively being raised to the ALI. Stratification proceeded for 14 days, during which time an electrical barrier in excess of 2000 Ω cm^2 was observed. This protocol was also scalable to larger 6 well plates, as well as 12 well plates.

Significant challenges remain in cell characterization for this protocol. Due to the fragile nature of the barrier on the insert and its small thickness, processing for histological applications was challenging. However, despite this handicap, this protocol enables a lot more experiments than differentiation on collagen matrixes or even more fragile *ex vivo* samples.

Welham and coworkers [32-34] have been attempting to characterize the proteome, extracellular matrix and gene expression of the vocal fold epithelia. This platform with some improvements offers a much simpler system to study. Given that the epithelial progenitor differentiation can be carried out on Synthemax and StemAdhere, both of which are defined extracellular proteins [28], analyzing the ECM deposited by the differentiating cells provides a cleaner system. Would healing rates can be easily plotted through the measurement of TEER, a more objective approach than image analysis [26]. Scaling down this system into 24 well plates or 48 well plates, which can be reasonably expected to be successful, based on a similar scale down of the blood brain barrier system [35] will enable simpler easier drug screens to investigate vocal fold mucosa injury.

Longer stratification times may lead to thicker tissue in this protocol. Overlaying the epithelial progenitors with collagen when adding the VFFs may also be tried to restore the ~100 µm thickness of the vocal fold epithelium. However, significant questions still remain regarding the embryonic germ layer origin of this differentiated tissue. It is expected to express similar markers to the tissue derived by Leydon and coworkers [13], based on the analogical approach. This protocol leads to tissue that is most probably ectodermal in origin, however, recent work by Lungova and Thibeault [36] indicate a endodermal origin for the vocal fold mucosa. A blend of endodermal progenitor differentiation techniques along with the technical knowledge of using inserts, may allow for tissue engineering an endoderm derived tissue.

Ultimately, the novelty of this work is the culturing on hPSCs on inserts, along with the use of barrier phenotypes to guide differentiation protocol development. Some challenges remain to generate tissue identical to *in vivo* vocal fold epithelia, however a scalable, convenient platform has been developed to speed up that process.

3.4 Materials and Methods

3.4.1 hPSC Maintenance and differentiation

Epithelial progenitor cells were differentiated from a hESC line (WA09; passage 20–26).

Briefly, hESCs were cultured on Matrigel (BD Biosciences), then plated on Matrigel-coated plates, and cultured in mTeSR1 (StemCell Technologies, Vancouver, CA) for hESC expansion. For differentiation, hESCs were cultured on Matrigel (BD Biosciences, San Jose, CA) in unconditioned hESC medium (UM) supplemented with retinoic acid (UM + RA): the DMEM/F12 containing 20%

knockout serum replacer (Life Technologies Corporation, Carlsbad, CA), 1 ·MEM nonessential amino acids, 1mM L-glutamine, 0.1mM 2-mercaptoethanol, and 1 mM all-trans retinoic acid (Sigma Aldrich, St. Louis, MI). Cells were cultured in UM+ RA for 5 days with the medium changed daily. After this, the inserts were transferred onto vocal fold epithelial cells plated wells. The human vocal fold fibroblast cell line, 21T (passage 5–6), was used in this study. This primary cell line was developed from pathogen-free vocal folds obtained from a 21-year-old male donor and has been characterized previously.18 The protocol was approved by the Institutional Review Board of the University of Wisconsin–Madison. The apical and baso-lateral side of the insert were then flooded with flavinoid adenine dinucleotide (FAD) media. The media were composed of Ham's F-12/DMEM (3:1 ratio), FBS (2.5%), hydrocortisone (0.4 mg/mL), cholera toxin (8.4 ng/mL), insulin (5 mg/mL), adenine (24 mg/mL), EGF (10 ng/mL), penicillin (100 U/mL), and streptomycin (0.01 mg/mL). An ALI was created 2 days later by removing media from the apical side of the insert. Cultures were grown at the ALI for 19–21 days. Experiments were performed in triplicate.

3.4.2 Barrier Electrical Resistance Measurement

TEER was measured via EVOM voltohmeter with STX2 electrodes (World Precision Instruments), and all measurements were performed at 37°C to prevent fluctuations in TEER value due to temperature change. The resistance value of an empty filter coated with Matrigel was subtracted from each measurement.

3.4.3 Barrier permeability measurement

Sodium fluorescein (10 µM, Sigma) was diluted in FAD media, and 0.5 mL was added to the upper chamber of a 12-well Transwell® filter. Aliquots (200 µL) were extracted from the basolateral

chamber (1.5 mL) every 15 min over the course of 1 h and replaced by an equal volume of fresh medium. The rates of accumulation in the basolateral chamber, as well as that across an empty insert coated with Matrigel, were used to calculate the P_e value. During measurement, filters were incubated at 37°C on a rotating platform.

3.5 Figures

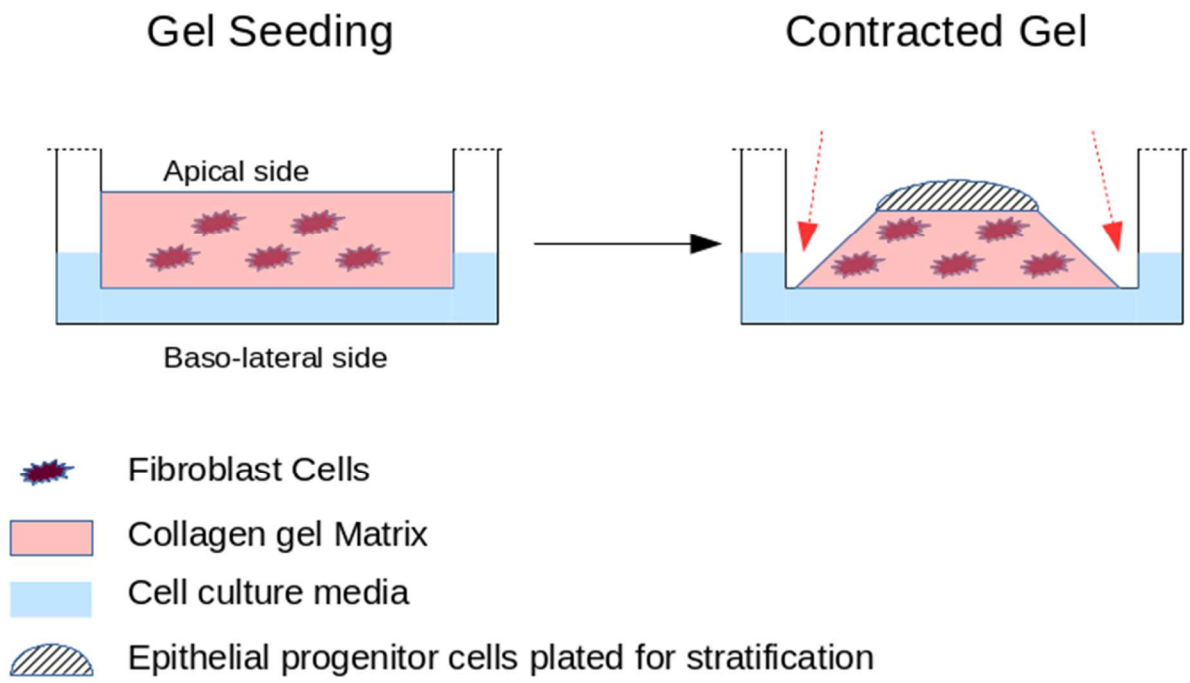

Figure 3.1: A diagram showing the challenges of performing barrier studies with the collagen gel system. When the gel is seeded on the apical side, it covers the entire apical surface. On further growth of the fibroblasts in the gel, it contracts into a roughly trapezoidal shape exposing gaps on the surface of the insert. Ions and dyes may thus flow freely in the apical and baso-lateral side disrupting barrier measurements.

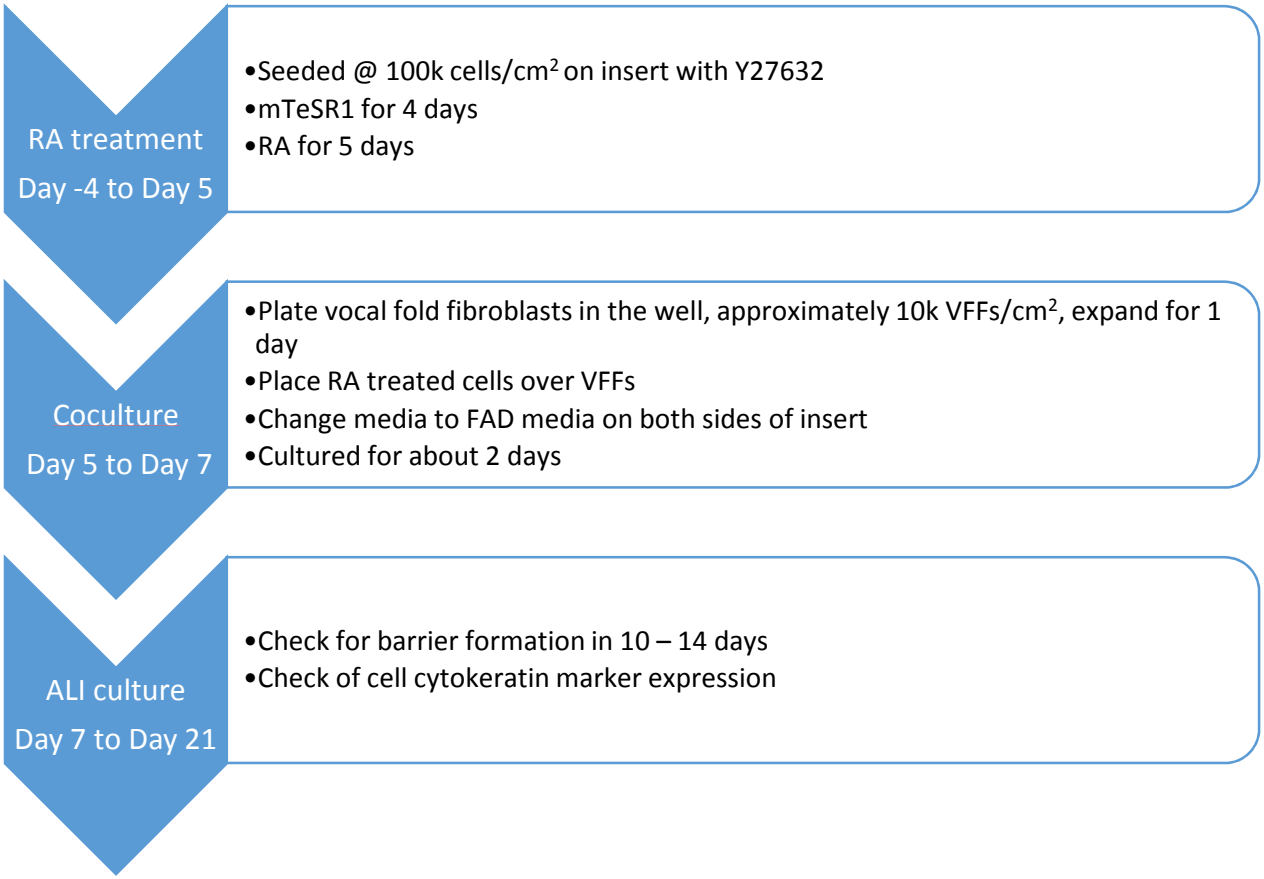

Figure 3.2: Schematic showing the differentiation scheme, based on the collagen gel scheme. Instead of performing RA treatment and then subculturing on a collagen-fibroblast gel, in this scheme, the RA differentiated cells are simply transferred over the vocal fold fibroblasts. The remaining steps of FAD for 2 days following the rise to the air liquid interface remains the same.

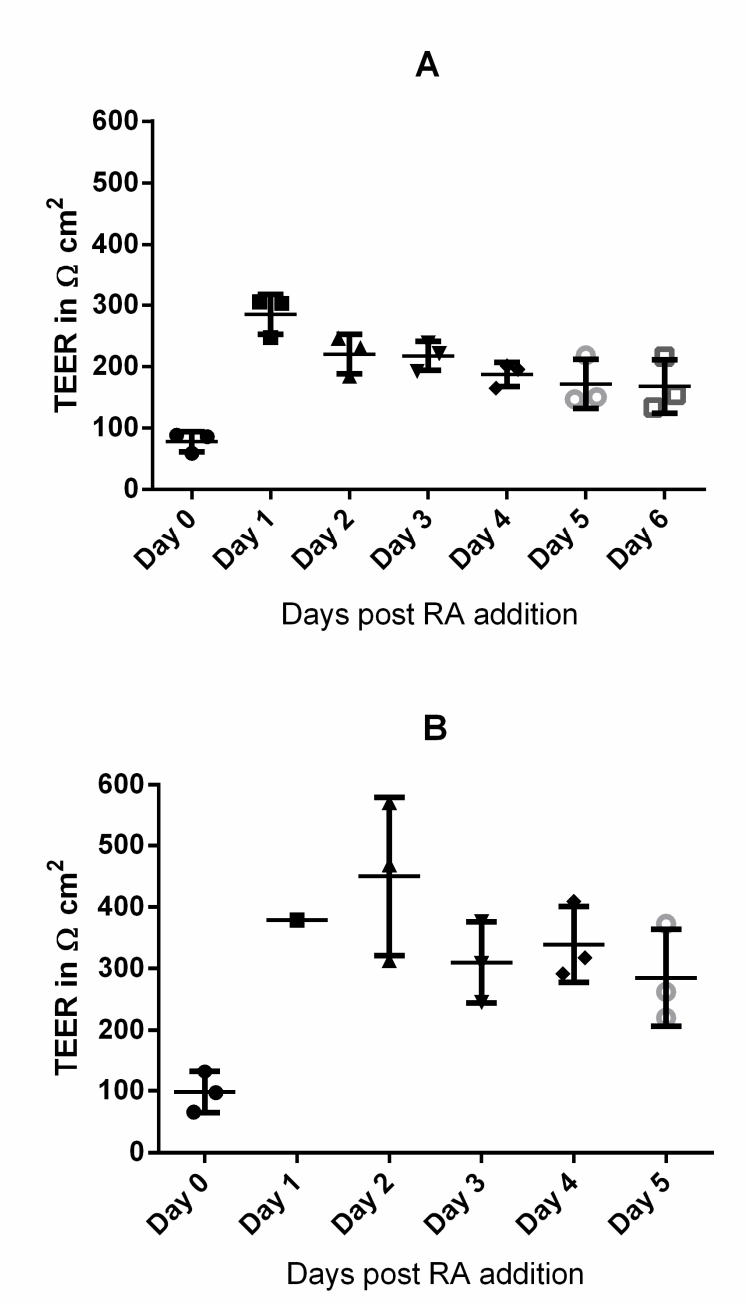

Figure 3.3: Transepithelial electrical resistance expressed in Ω cm^2 for cultures in which (A) 50k cells/cm^2 were seeded and (B) 100k cells/cm^2 were seeded and expanded for 4 days. The mean TEER is higher for the denser seeding condition.

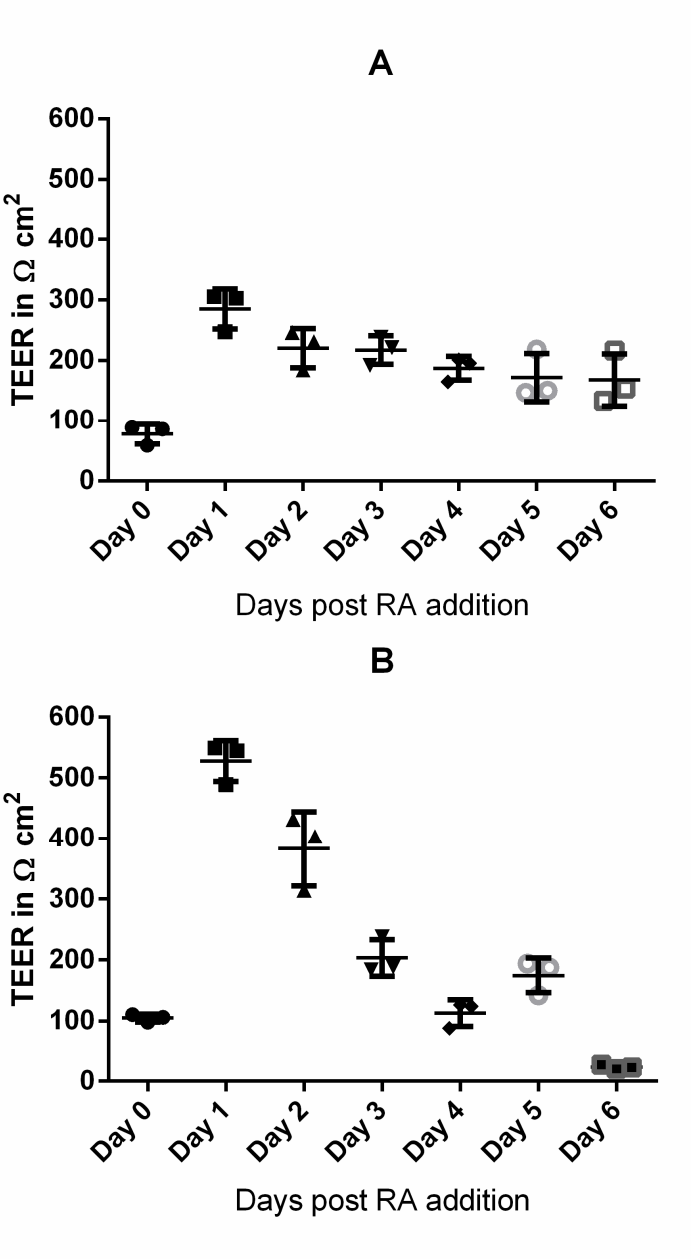

Figure 3.4: Transepithelial electrical resistance expressed in Ω cm^2 for cultures in which (A)3 µm pore size inserts were used and (B) 0.4 µm pore size inserts were used. The mean TEER is higher for the larger pore size condition.

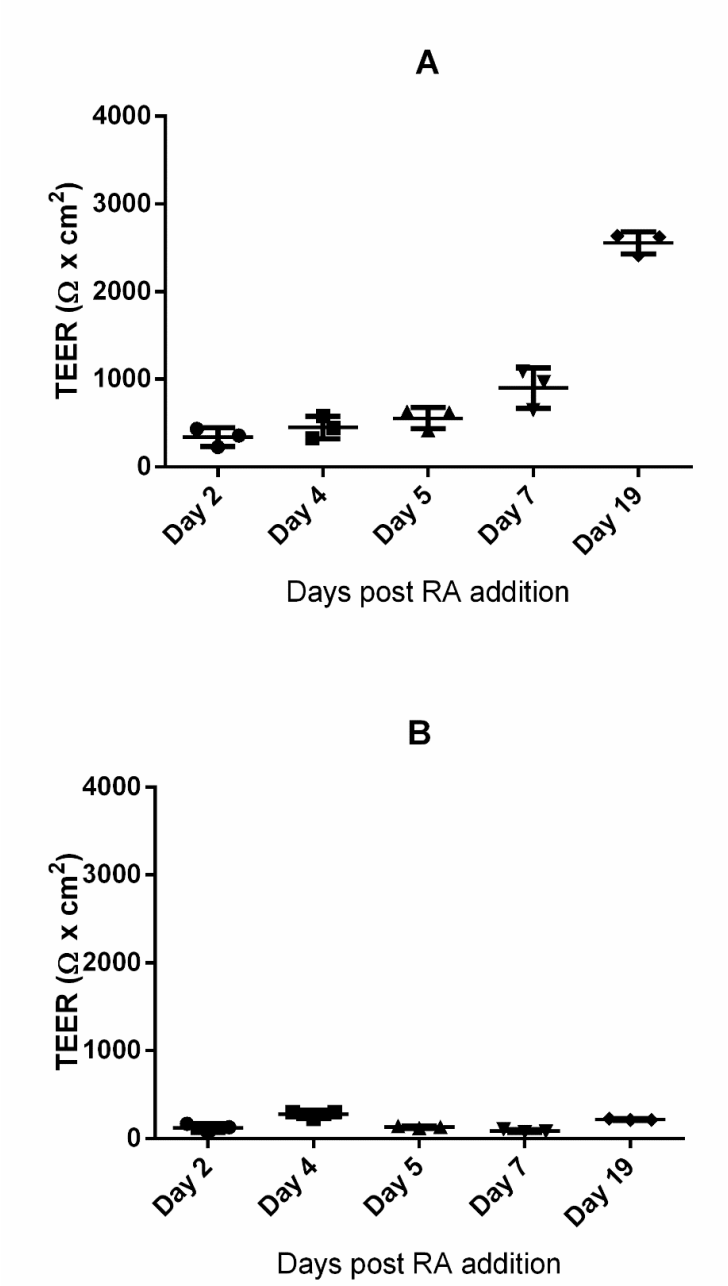

Figure 3.5: Transepithelial electrical resistance expressed in Ω cm^2 for cultures in which (A) polycarbonate 3 µm pore size inserts were used and (B) polyester 3 µm pore size inserts were used. The mean TEER is higher for the polycarbonate condition.

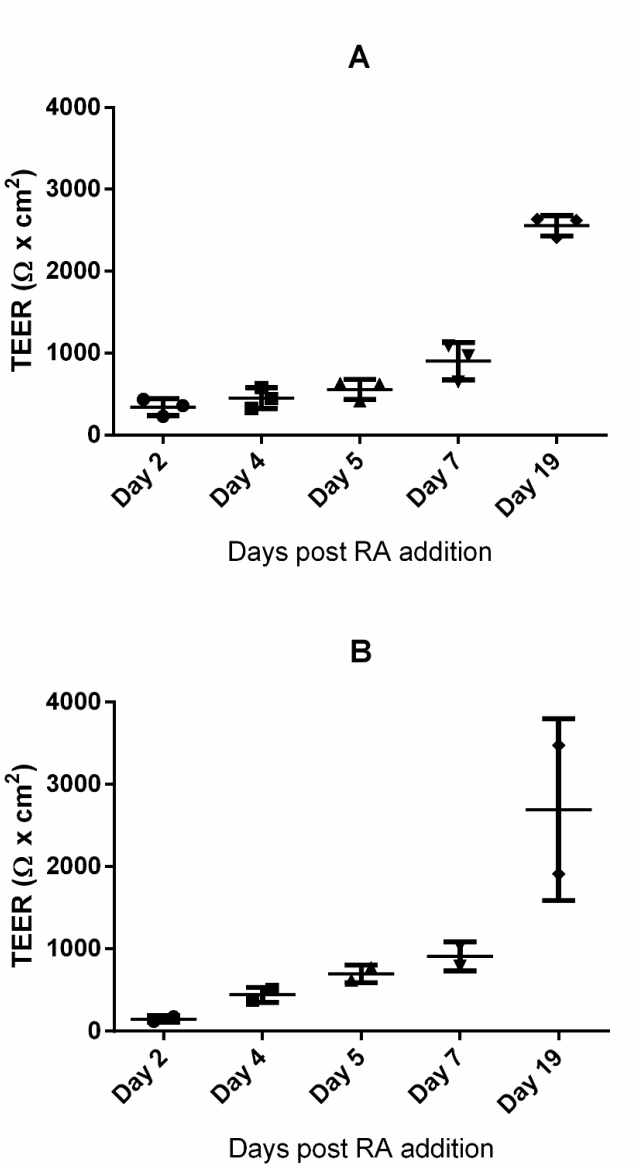

Figure 3.6: Transepithelial electrical resistance expressed in Ω cm2 for cultures in which (A) 1.2 cm diameter (12 well plate) polycarbonate 3 µm pore size inserts were used and (B) 4.5 cm diameter (6 well plate) polycarbonate 3 µm pore size inserts were used. The mean TEER are very similar indicating scalability.

Figure 3.7: Histology and hematoxylin and eosin staining for cells differentiated on 3 µm pore size polycarbonate insert, after stratification for 14 days. Scale bar is 200 µm.

3.6 References

1. Titze IR. The Human Instrument. Scientific American Jan2008. 2008;298(1):94. PubMed PMID: 27818310.

2. Hartnick CJ, Rehbar R, Prasad V. Development and maturation of the pediatric human vocal fold lamina propria. Laryngoscope. 2005;115(1):4-15. doi: 10.1097/01.mlg.0000150685.54893.e9. PubMed PMID: WOS:000226340700002.

3. Sivasankar M, Fisher KV. Oral breathing increases P-th and vocal effort by superficial drying of vocal fold mucosa. Journal of Voice. 2002;16(2):172-81. doi: 10.1016/s0892-1997(02)00087-5. PubMed PMID: WOS:000181346800002.

4. Sivasankar M, Erickson E, Schneider S, Hawes A. Phonatory Effects of Airway Dehydration: Preliminary Evidence for Impaired Compensation to Oral Breathing in Individuals With a History of Vocal Fatigue. Journal of Speech Language and Hearing Research. 2008;51(6):1494-506. doi: 10.1044/1092-4388(2008/07-0181). PubMed PMID: WOS:000261196100009.

5. Verdolini K, Min Y, Titze IR, Lemke J, Brown K, van Mersbergen M, et al. Biological mechanisms underlying voice changes due to dehydration. Journal of Speech Language and Hearing Research. 2002;45(2):268-81. doi: 10.1044/1092-4388(2002/021). PubMed PMID: WOS:000174886700004.

6. Gray SD. Cellular physiology of the vocal folds. Otolaryngologic Clinics of North America. 2000;33(4):679-+. doi: 10.1016/s0030-6665(05)70237-1. PubMed PMID: WOS:000089071300002.

7. Behrman A, Rutledge J, Hembree A, Sheridan S. Vocal hygiene education, voice production therapy, and the role of patient adherence: A treatment effectiveness study in women with phonotrauma. Journal of Speech Language and Hearing Research. 2008;51(2):350-66. doi: 10.1044/1092-4388(2008/026). PubMed PMID: WOS:000254529700004.

8. Gill GA, Buda A, Moorghen M, Dettmar PW, Pignatelli M. Characterisation of adherens and tight junctional molecules in normal animal larynx; Determining a suitable model for studying molecular abnormalities in human laryngopharyngeal reflux. Journal of Clinical Pathology. 2005;58(12):1265-70. doi: 10.1136/jcp.2004.016972. PubMed PMID: WOS:000233462100006.

9. Roy N, Merrill RM, Thibeault S, Parsa RA, Gray SD, Elaine S. Prevalence of voice disorders in teachers and the general population. Journal of Speech Language and Hearing Research. 2004;47(2):281-93. doi: 10.1044/1092-4388(2004/023). PubMed PMID: WOS:000232285300004.

10. Fisher KV, Telser A, Phillips JE, Yeates DB. Regulation of vocal fold transepithelial water fluxes. Journal of Applied Physiology. 2001;91(3):1401-11. PubMed PMID: WOS:000170552800050.

11. Arens C, Glanz H, Woenckhaus J, Hersemeyer K, Kraft M. Histologic assessment of epithelial thickness in early laryngeal cancer or precursor lesions and its impact on endoscopic

imaging. European Archives of Oto-Rhino-Laryngology. 2007;264(6):645-9. doi: 10.1007/s00405-007-0246-8. PubMed PMID: WOS:000246203000011.

12. Levendoski EE, Leydon C, Thibeault SL. Vocal Fold Epithelial Barrier in Health and Injury: A Research Review. Journal of Speech Language and Hearing Research. 2014;57(5):1679-91. doi: 10.1044/2014_jslhr-s-13-0283. PubMed PMID: WOS:000348200500008.

13. Leydon C, Selekman JA, Palecek S, Thibeault SL. Human Embryonic Stem Cell-Derived Epithelial Cells in a Novel In Vitro Model of Vocal Mucosa. Tissue Engineering Part A. 2013;19(19-20):2233-41. doi: 10.1089/ten.tea.2012.0744. PubMed PMID: WOS:000323933400015.

14. Leydon C, Bartlett RS, Roenneburg DA, Thibeault SL. Localization of Label-Retaining Cells in Murine Vocal Fold Epithelium. Journal of Speech Language and Hearing Research. 2011;54(4):1060-6. doi: 10.1044/1092-4388(2010/10-0267). PubMed PMID: WOS:000293380900006.

15. Savelli V, Rizzoli R, Rizzi E, Galanzi A, Buffa A, Rana R, et al. Cell kinetics of vocal fold epithelium in rats. Bollettino della Societa italiana di biologia sperimentale. 1991;67(12):1081-8. PubMed PMID: MEDLINE:1840800.

16. Knight DA, Holgate ST. The airway epithelium: Structural and functional properties in health and disease. Respirology. 2003;8(4):432-46. doi: 10.1046/j.1440-1843.2003.00493.x. PubMed PMID: WOS:000187227600003.

17. Suzuki T. Regulation of intestinal epithelial permeability by tight junctions. Cellular and Molecular Life Sciences. 2013;70(4):631-59. doi: 10.1007/s00018-012-1070-x. PubMed PMID: WOS:000314044900004.

18. Sivasankar M, Erickson E, Rosenblatt M, Branski RC. Hypertonic challenge to porcine vocal folds: Effects on epithelial barrier function. Otolaryngology-Head and Neck Surgery. 2010;142(1):79-84. doi: 10.1016/j.otohns.2009.09.011. PubMed PMID: WOS:000276574200014.

19. Li H, Sheppard DN, Hug MJ. Transepithelial electrical measurements with the Ussing chamber. Journal of cystic fibrosis : official journal of the European Cystic Fibrosis Society. 2004;3 Suppl 2:123-6. doi: 10.1016/j.jcf.2004.05.026. PubMed PMID: MEDLINE:15463943.

20. Hasegawa H, Fujita H, Katoh H, Aoki J, Nakamura K, Ichikawa A, et al. Opposite regulation of transepithelial electrical resistance and paracellular permeability by Rho in Madin-Darby canine kidney cells. Journal of Biological Chemistry. 1999;274(30):20982-8. doi: 10.1074/jbc.274.30.20982. PubMed PMID: WOS:000081613100037.

21. Balda MS, Whitney JA, Flores C, Gonzalez S, Cereijido M, Matter K. Functional dissociation of paracellular permeability and transepithelial electrical resistance and disruption of the apical-basolateral intramembrane diffusion barrier by expression of a mutant tight junction membrane protein. Journal of Cell Biology. 1996;134(4):1031-49. doi: 10.1083/jcb.134.4.1031. PubMed PMID: WOS:A1996VD43100018.

22. Woo P, Casper J, Colton R, Brewer D. DIAGNOSIS AND TREATMENT OF PERSISTENT DYSPHONIA AFTER LARYNGEAL SURGERY - A RETROSPECTIVE ANALYSIS OF 62 PATIENTS. Laryngoscope. 1994;104(9):1084-91. PubMed PMID: WOS:A1994PF21000007.

23. Chen X, Thibeault SL. Biocompatibility of a synthetic extracellular matrix on immortalized vocal fold fibroblasts in 3-D culture. Acta Biomaterialia. 2010;6(8):2940-8. doi: 10.1016/j.actbio.2010.01.032. PubMed PMID: WOS:000279583400009.

24. Metallo CM, Ji L, De Pablo JJ, Palecek SP. Retinoic acid and bone morphogenetic protein signaling synergize to efficiently direct epithelial differentiation of human embryonic stem cells. Stem Cells. 2008;26(2):372-80. doi: 10.1634/stemcells.2007-0501. PubMed PMID: WOS:000253372600009.

25. Metallo CM, Azarin SM, Moses LE, Ji L, de Pablo JJ, Palecek SP. Human Embryonic Stem Cell-Derived Keratinocytes Exhibit an Epidermal Transcription Program and Undergo Epithelial Morphogenesis in Engineered Tissue Constructs. Tissue Engineering Part A. 2010;16(1):213-23. doi: 10.1089/ten.tea.2009.0325. PubMed PMID: WOS:000273432300019.

26. Palencia L, Das A, Palecek SP, Thibeault SL, Leydon C. Epidermal growth factor mediated healing in stem cell-derived vocal fold mucosa. J Surg Res. 2015;197(1):32-8. doi: 10.1016/j.jss.2015.02.066. PubMed PMID: 25818979.

27. Petrova A, Celli A, Jacquet L, Dafou D, Crumrine D, Hupe M, et al. 3D In vitro model of a functional epidermal permeability barrier from human embryonic stem cells and induced pluripotent stem cells. Stem Cell Reports. 2014;2(5):675-89. doi: 10.1016/j.stemcr.2014.03.009. PubMed PMID: 24936454; PubMed Central PMCID: PMCPMC4050479.

28. Selekman JA, Grundl NJ, Kolz JM, Palecek SP. Efficient Generation of Functional Epithelial and Epidermal Cells from Human Pluripotent Stem Cells Under Defined Conditions. Tissue Engineering Part C-Methods. 2013;19(12):949-60. doi: 10.1089/ten.tec.2013.0011. PubMed PMID: WOS:000327304900005.

29. Lippmann ES, Azarin SM, Kay JE, Nessler RA, Wilson HK, Al-Ahmad A, et al. Derivation of blood-brain barrier endothelial cells from human pluripotent stem cells. Nature Biotechnology. 2012;30(8):783-91. doi: 10.1038/nbt.2247. PubMed PMID: WOS:000307416900022.

30. Kaiser ML, Rubinstein M, Vokes DE, Ridgway JM, Guo S, Gu M, et al. Laryngeal epithelial thickness: a comparison between optical coherence tomography and histology. Clinical Otolaryngology. 2009;34(5):460-6. PubMed PMID: WOS:000270176700006.

31. Zhang Q, Fisher K. Tight Junction-Related Barrier Contributes to the Electrophysiological Asymmetry across Vocal Fold Epithelium. Plos One. 2012;7(3). doi: 10.1371/journal.pone.0034017. PubMed PMID: WOS:000303836500080.

32. Welham NV, Yamashita M, Choi SH, Ling C. Cross-Sample Validation Provides Enhanced Proteome Coverage in Rat Vocal Fold Mucosa. Plos One. 2011;6(3). doi: 10.1371/journal.pone.0017754. PubMed PMID: WOS:000288513900021.

33. Welham NV, Chang Z, Smith LM, Frey BL. Proteomic analysis of a decellularized human vocal fold mucosa scaffold using 2D electrophoresis and high-resolution mass spectrometry. Biomaterials. 2013;34(3):669-76. doi: 10.1016/j.biomaterials.2012.09.050. PubMed PMID: WOS:000312759800007.

34. Welham NV, Ling C, Dawson JA, Kendziorski C, Thibeault SL, Yamashita M. Microarray-based characterization of differential gene expression during vocal fold wound healing in rats. Disease Models & Mechanisms. 2015;8(3):311-21. doi: 10.1242/dmm.018366. PubMed PMID: WOS:000352162300010.

35. Wilson HK, Canfield SG, Hjortness MK, Palecek SP, Shusta EV. Exploring the effects of cell seeding density on the differentiation of human pluripotent stem cells to brain microvascular endothelial cells. Fluids and barriers of the CNS. 2015;12:13-. doi: 10.1186/s12987-015-0007-9. PubMed PMID: MEDLINE:25994964.

36. Lungova V, Verheyden JM, Herriges J, Sun X, Thibeault SL. Ontogeny of the mouse vocal fold epithelium. Developmental Biology. 2015;399(2):263-82. doi: 10.1016/j.ydbio.2014.12.037. PubMed PMID: WOS:000351027200007.

4 Phenotypic changes in cells cultured on a superhydrophobic surface

4.1 Introduction

4.1.1 Interplay between surface topography and cellular behavior

Cellular behavior can be influenced by changing the topography of surfaces on which the cells are plated. Initial work on placing cancer cells on topographies that have features in the ~100 nm range was initially carried out by Wilkinson and coworkers[1], who placed osteosarcoma cells on ~100 nm ridges and observed differences in cell adhesion. In findings reviewed by Wilkinson and coworkers about a decade later [2], several insights were gained about the cause of these behaviors.

Initially, it was hypothesized that the changes occurring are not due to topography but due to the substrate material that the cell culture substrates were synthesized from. However, a review of the literature published by Paul Nealey and coworkers [3], indicated that “topographical cues, independent of biochemistry” had significant effects on cell behavior. Cells respond to altered topography by modulating morphology and migration characteristics [4]. These responses were caused by changes in the gene expression of cells that are plated on topographically altered surfaces [5]. The work by Choquet et al, indicated that matrix rigidity serves as a cue in the migration characteristics of cells. More recently, Leong and coworkers showed that there was nanotopography was more dominant in cytoskeletal organization than substrate stiffness [6].

All of the experiments described so far were done on hydrophilic surfaces promoting some degree of cell adhesion. Studies of cells on superhydrophobic surfaces are much more recent.

4.1.2 Generation of superhydrophobic surfaces

The term “superhydrophobic” is generally used to describe surfaces and interfaces exhibiting contact angles in excess of 150° [7-11], standard hydrophobic cell culture surfaces have contact angles around 110°. The low contact angle causes water droplets to form beads and roll off the surface rather than adhering to and spreading on the surface. These interfaces are completely resistant to wetting by aqueous media. The non-wetting nature of these surfaces is attributed to the combination of the presence and type of micro/nano scale roughness (~100 nm) and the hydrophobic surface functionality. As stated before, surface topography features in the ~100 nm size range have been shown to influence cell behavior.

Superhydrophobic surfaces can be generated through a variety of methods. These surfaces can be generated through coating of an etched surface with oxygen plasma [12], spin coating with fluorinated hydrocarbons [7] or poly-electrolyte multilayer assembly [13]. Lynn and coworkers [13] have pioneered the generation of superhydrophobic surfaces using poly-electrolyte multilayers generated using layer-by-layer assembly methods. The layer-by-layer electrostatic assembly technique is an inexpensive method of thin film manufacture via alternating adsorption of positively and negatively charged species from polar solutions [14]. Polymer organic and organic/inorganic thin films formed using this technique may contain a number of different functional groups, in this case, alkyl groups providing hydrophobic functionality.

Lynn and coworkers have shown that reactions between primary amine-functionalized polymers and azalactone functionalized polymers, specifically branched poly(ethyleneamine) PEI and poly(2-vinyl-4,4-dimethylazalactone)(PVDMA) can be used to fabricate cross-linked and amine

reactive multilayers[15]. Figure 4.1 shows the scheme of the reaction of PVDMA with a representative primary amine (Figure 4.1B) and a schematic showing post-fabrication functionalization of an azlactone-containing film (by reaction with a primary amine) (Figure 4.1C) [16]. The functionalization of the PEI with decylamine significantly increased the contact angle and created a superhydrophobic surface [17].

The functionalized PVDMA/PEI surface developed by the Lynn group [13], showed superhydrophobicity even when stored underwater for up to 6 weeks. This resilience made it an ideal substrate on which to attempt cell culture experiments lasting up to 48 hours. Superhydrophobic surfaces have been used in conjunction with cell culture, but not necessarily as a cell culture substrate since the early 90s.

4.1.3 Cell culture on superhydrophobic surfaces

Schakenraad and coworkers performed the first study to attempt cell culture on Teflon coated plastic did so with skin fibroblasts, and showed that on the superhydrophobic surface, there was low attachment of the fibroblasts [18]. These findings were later used by a number of groups to perform micropatterning studies. The concept of micropatterning was to create exclusion zones, where cells would not attach and thereby control the geography of areas in which the cells attached. Most of these studies utilized arrays with superhydrophobic (contact angle > 150°) and superhydrophilic regions (water contact angle <10°). Cells would preferentially attach to the superhydrophilic regions and proliferate within those regions [19-28].

The micropatterning strategy is based on the low attachment of proteins on the superhydrophobic surfaces demonstrated using fibronectin (an extracellular matrix protein) [29],

and several bacterial proteins [30]. However, a protein attachment resistant surface that has normal water contact angles could be used as a control for experiments performed using superhydrophobic surfaces. The use of this surface as a control demonstrated that the effects seen due to cell culture on superhydrophobic surfaces was due to its superhydrphobic nature, not the inability of cells to attach to a surface. The low attachment surface used in this study was a surface coated with poly(2-hydroxyethylmethacrylate) (Poly-HEMA) which was characterized as being a low protein absorbing polymer in the 1980s[31-34].

Several other studies utilized superhydrophobic surfaces to generate liquid marbles for encapsulating droplets of cells and studying the behavior of cell suspensions [35-37]. Liquid marbles are aqueous solutions bound within a sphere of a hydrophobic material. The materials used were breathable and allowed gaseous contact of the droplet allowing for cellular respiration. However, these were still not cells that are suspended entirely upon a superhydrophobic surface.

Two recent studies have characterized cells in created using superhydrophobic surfaces. The first used spherical droplets on a superhydrophobic surface to create a plastic mold with quasi-spherical droplets [38]. Within these molds, which were made up of a low attachment material, cancer cells were grown over extended periods and characterized. The second study used a switchable material, one that can switch between superhydrophobic and supherhydrophilic states, to create an anchored spherical droplet that was used for hanging drop culture [39]. This allowed for an almost-spherical hanging drop which could be used to make spherical cell aggregates. However, in none of these studies were cells grown in a droplet that is minimally

anchored to the substrate. Our study aims to use the functionalized PVDMA-PEI substrate to study cells grown in a droplet, on a superhydrophobic surface.

4.1.4 Aim of the current study

In this study it was demonstrated that cells can be viably grown in a droplet suspended on a superhydrophobic surface. It was observed that the cells were viable for days rather than hours. We further demonstrated that the cells grown on these surfaces were phenotypically different from cells grown either on adhesive surfaces or on surfaces that promote low cell attachment, but had hydrophobicity comparable to standard cell culture polystyrene. We also hypothesized on the transcriptional changes occurring within the cells grown on the superhydrophobic surface as opposed to the adhesive and the low attachment surfaces.

4.2 Results

4.2.1 Serum content affects the superhydrophobicity of the PVDMA/PEI substrate

The MCF-7 cells used in this study can be cultured in DMEM media supplemented with up to 10% fetal bovine serum (FBS). In order to test the substrate, droplets containing 1% serum and 10% serum were placed on the substrate for 24 hours at 37 °C. They were placed in a petri dish containing cell culture treated water to minimize evaporation of the media. It was noticed that the 10% FBS droplet had spread out across the substrate, indicating the loss of superhydrophobicity, with the 1% serum droplet maintained its intact spherical shape. Therefore experiments with this substrate needed to be conducted in 1% serum conditions (Figure 4.2).

Since the drop in serum concentration can affect cell behavior, the MCF-7 cells were pre-treated for 7 days in 1% serum condition prior to being put into suspension and transferred onto the droplet.

4.2.2 Viability

The viability of the cells in the droplet was measured after 12 hours, 24 hours and 48 hours in suspension. Four different density regimes were tested, ranging from 100 cells/µL to 5000 cells/µL. Cell viability was also tested for conditions in which the droplet was agitated for 24 & 48 hours at 140 rpm. The viability of the cells was compared to equivalent conditions of cell suspensions on poly-HEMA coated low adhesion surfaces.

Figure 4.3 shows the viability of the cells when kept on the substrate (Figure 4.3A) and a low attachment surface (Figure 4.3B) for 12 hours. Viability increased with increasing density and was about 80%. Figure 4.4 shows the viability over 24 hours of culture on the superhydrophobic substrate (Figure 4.4A) and the Low attachment surface (Figure 4.4B). Figure 4.5 shows the viability for 48 hours of culture, on the superhydrophobic surface. From Figure 4.5A, it was seen that there was a reduction in viability of the cells at lower densities with only ~26 - 36% of the cells surviving. However, on the low attachment surface (Figure 4.5B), there was a smaller reduction in viability in the high density condition. Since the 5000 cells/µL condition showed high viability across all time points on the superhydrophobic surface, it was chosen for further experiments.

Viability was also measured when the substrates were shaken at 130 rpm to induce motion of the droplet. Two densities were experimented with, 500 cells/µL and 5000 cells/µL for 24

shaking. Figure 4.6 shows that viability of shaken cells on both the superhydrophobic substrate and the low attachment control condition.

Having confirmed that the cells survived on the substrate for up to 2 days, the cytoskeletal organization of the cells was investigated. This would indicate if the cells were reorganizing their cytoskeletal structure when on the superhydrophobic substrates.

4.2.3 Morphology

Figure 4.7 shows the phalloidin staining results for cells on superhydrophobic surfaces (Figure 4.7A), on low attachment surfaces (Figure 4.7B) and for adherent cells (Figure 4.7C). Through this staining, it was evident that there were no stress fibers present in either the cells grown on the superhydrophobic surface or the low attachment surface. This diffuse presentation of actin was to be expected as there were no anchorage points present in the cells that were suspended in media. Through these images it also appeared that there was some clustering of cells present in the superhydrophobic substrate. The behavior of the cells when removed from this substrate was tested next.

4.2.4 Replating behavior

Cells treated in suspension conditions can often undergo a change in behavior when reintroduced to standard tissue culture treated polystyrene surfaces. The cells were kept in suspension either on the superhydrophobic substrate or the low attachment substrate for either 6, 12 or 24 hours and then transferred onto the tissue culture polystyrene at a density of about 20,000 cells/cm^2. Since the doubling time of the MCF-7 cell line is about 3 -4 days, the cell density for replating was assumed to be the same as that for cell seeding. The cells were then viewed 24 hours later. Figure

4.8 is a schematic explaining the procedure of the experiment. It was suspected that there would be differences in replating characteristics between the two conditions, therefore images were taken with and without the cell culture media. Suspended cells would not appear in the media removed conditions. Figure 4.9 shows the adherence of MCF-7 cells 24 hours after harvesting with Trypsin and placing onto tissue culture polystyrene. It established that these cells are not suspension conditioned.

Figure 4.10 shows cells after 6 hours of culture on tissue culture polystyrene following 6 hours of treatment on superhydrophobic surfaces with shaking at 130 rpm with media (A) and (B) after media removal. (C) & (D) are on superhydrophobic surface without shaking, (E) & (F) are on low attachment surfaces with shaking at 130 rpm and (G) and (H) are on low attachment surfaces without shaking. It was evident that regardless of the surface treatment, superhydrophobic or low attachment, a majority of the cells were able to replate onto the surface.

Figure 4.11 shows cells after 12 hours of culture on tissue culture polystyrene following 12 hours of treatment on superhydrophobic surfaces with shaking at 130 rpm with media (A) and (B) after media removal. (C) & (D) are on superhydrophobic surface without shaking, (E) & (F) are on low attachment surfaces with shaking at 130 rpm and (G) and (H) are on low attachment surfaces without shaking. Here differences started to emerge between the superhydrophobic conditions and the low attachment conditions. It was evident that there was low replating of cells on the superhydrophobic condition. While some colonies formed on the non-shaken condition (colony in image (D) showed some cytoskeletal structure, most of the cells remained in suspension.

Whereas for the low attachment condition, there was almost complete replating of cell aggregates onto the polystyrene.

Figure 4.12 shows cells after 24 hours of culture on tissue culture polystyrene following 24 hours of treatment on superhydrophobic surfaces with shaking at 130 rpm with media (A) and (B) after media removal. (C) & (D) are on superhydrophobic surface without shaking, (E) & (F) are on low attachment surfaces with shaking at 130 rpm and (G) and (H) are on low attachment surfaces without shaking. It was evident that there is low replating of cells on the superhydrophobic condition, and unlike the cells treated for 12 hours, no colonies formed on the non-shaken superhydrophobic condition. There was almost complete replating of cell aggregates onto the polystyrene for the low attachment condition.

4.3 Discussion

The change in the replating characteristics appeared to suggest a process of epithelial to mesenchymal transition (EMT) occurring within these cells. Epithelial cells form protective barriers that surround tissues and therefore are expected to form adherent sheets of cells in culture. Mesenchyme, however consist of cells that are expected to fill up cavities within the body, and therefore are capable of subsisting without the presence of an anchoring surface [40-43]. In MCF-7 cells EMT induction has occurred through quasi-3D culture [38] and through the engineering of EMT inducing protein overproduction within the cells [44]. In both of these processes, however, the cells took up to 7 days to show characteristics of mesenchymal cells, our replating experiments indicated that the transition was perhaps occurring in hours.

The 6 – 12 hour time window in which the transtition occured indicates that the cause of the transition was perhaps transcriptional, rather than signaling cascade induced. Changes induced through phosphorylation of proteins, typically occur in 1 – 2 hours. Reverse Transcriptase-Polymerase Chain Reaction (RT-PCR) analysis for E-Cadherin, N-Cadherin, Snail and TGFβ1 could elucidate the molecular mechanism driving the changes seen in the behavior of the cells. E-Cadherin is expected to reduce in the superhydrophobic culture condition, while the other three markers are expected to increase.

Should it be shown that there is EMT induction through cell culture over the superhydrophobic substrate, a future direction would be the investigation of this substrate in wound healing applications, as EMT followed by migration of skin cells along the wound bed are a principal component of the wound healing process[41, 45]. However, prior to testing with skin cells, the functionalization of the PEI should be investigated to make it more resistant to degradation by serum or serum albumin.

4.4 Conclusion

MCF-7 cells were plated on to a droplet suspended over a superhydrophobic surface consisting of decane functionalized PVDMA/PEI bilayers. In the presence of 100% humidity and 1% serum growth medium, the cells remained viable for up to 48 hours. Viability was correlated to density, where higher densities were more viable than lower densities. Across 48 hours of culture, 100 cells/µL suspensions were about 20% viable, while 5000 cells/µL were about 60% viable. When cells were cultured on superhydrophobic droplets for greater than 12 hours, they did not adhere to tissue culture treated surfaces for up to 24 hours, while cells cultured on low attachment

surfaces and adherent surfaces did. Cell suspension droplets cultured on superhydrophobic surface and shaken throughout the superhydrophobic surface treatment also remained viable, and did not adhere fully on to tissue culture treated surfaces after 6 hours of treatment.

In this chapter, a preliminary study on the properties of MCF-7 cells on superhydrophobic surfaces has been presented. Previous attempts of cell culture on superhydrophobic surfaces have not had the cells in a spherical droplet over the substrate. Here we show that the cells were able to survive without media replenishment for up to 48 hours on the surface. The variable space was successfully covered to establish the duration and density of cells that lead to maximum viability. In addition, while previous studies showed the suspended nature of the cells on these surfaces, they did not show data to indicate that the high contact angle of the superhydrophobic surface induces phenotypic changes. By comparing the phenotypic changes across superhydrophobic surfaces and non-adherent surfaces, it has been shown conclusively that the alteration in the behavior of the cells is due to the surface, rather than solely the inability of the cells to attach to a surface. Attempting this study with altered chemistry to address substrate degradation and attempts with greater number of cells to generate transcriptional data, could be possible steps forward. In this way, the changes can be attributed a mechanism, and the substrate itself can be used for further biological applications.

4.5 Material and Methods

4.5.1 Substrate manufacture

Solutions of PEI and azlactone-functionalized polymers (either PVDMA or PVDMATMR) were prepared in acetone or CH2Cl2 (20 mM with respect to the molecular weight of the polymer

repeat unit; the type of solvent used varied from experiment to experiment, see text). Films were fabricated layer-by-layer on the surfaces of CaCl2, sucrose, CuSO4, sugar cubes, and paper-based substrates using the following general protocol: (1) Substrates were immersed in a solution of PEI for 20 s. (2) Substrates were then removed and immersed, in succession, into two rinse solutions consisting of the appropriate pure solvent for 20 s. (3) Substrates were then immersed in a solution of PVDMA for 20 s. (4) Substrates were removed and rinsed again in the manner described under step 2. This cycle was repeated until the desired number of PEI/PVDMA layer pairs (or "bilayers"; typically 100) was deposited on the surface of the substrate. For the fabrication of films, polymer dipping solutions were replaced with fresh solutions after every 25 dipping cycles, and the rinse solvent was exchanged for fresh solvent after every 20 dipping cycles. Following the final rinse step, substrates were dried under a stream of filtered, compressed air and stored in a vacuum desiccator prior to use in experiments. All film fabrication procedures were performed at ambient room temperature.

4.5.2 Cell Culture

The human breast cancer cell line MCF-7 was obtained from American Type Culture Collection (ATCC, USA). The cells were cultured in complete media Dulbecco's modified eagle medium (DMEM) supplemented with glutamine and 10% (v/v) fetal bovine serum (FBS) at 37 °C in a 100% humidified incubator with 5% CO2. 7 days prior to the experiments, the cells were treated with 0.25% Trypsin/EDTA for 10 minutes and then split 1:4 and cultured in complete media Dulbecco's modified eagle medium (DMEM) supplemented with glutamine and 1% (v/v) fetal bovine serum (FBS), with changes in media occurring daily. For the experiment confluent cells were treated with 0.25% Trypsin/EDTA for 10 minutes, counted using a Nexcelon Auto T4 cell counter as per

manufacturer instructions, resuspended to the appropriate density and placed on the substrate for superhydrophobic cell culture experiments, or a 96 well plate well, coated with an ethanolic solution of 0.1% poly-HEMA(sigma) and dried.

The substrate was an aluminum hemisphere, coated with functionalized PVDMA/PEI and placed on a glass slide pasted onto a petri dish. The petri dish was filled with water to provide a local 100% humid atmosphere to limit evaporation of cell culture media from the droplet.

4.5.3 Viability measurements

Cells were treated with Trypan Blue (Invitrogen) according to manufacturer's instructions and viability measurements were obtained from Cellometer Auto T4 (Nexcelom Bioscience LLC, Lawrence, MA, USA). The image cytometer utilizes a bright-field (BR) light microscopy optical setup for image cytometric analysis. Each cell line was pipetted into the disposable counting chamber and bright-field images were captured for image analysis, where the system measured the color of the cells and converted the results to corresponding live/dead count.

4.5.4 Immunostaining

Cells with 4% formaldehyde for 20 minutes at room temperature by adding 4% formaldehyde in PBS in excess directly to the culture droplet. The fixed cell suspension was spun down and resuspended in deionized water and smeared over a microscope slide coated with poly-L-lysine (>70 kDa) and dried. It was washed until crystals were no longer visible on the slide. The cell spot was then surrounded with a hydrophobic barrier (Vectashield pen). The spot was then incubated with Alexa 594 conjugated Phalloidin (Invitrogen) at a 1:100 dilution overnight. It was washed, counterstained with nuclear stain Hoechst(Invitrogen) and imaged.

4.6 Figures

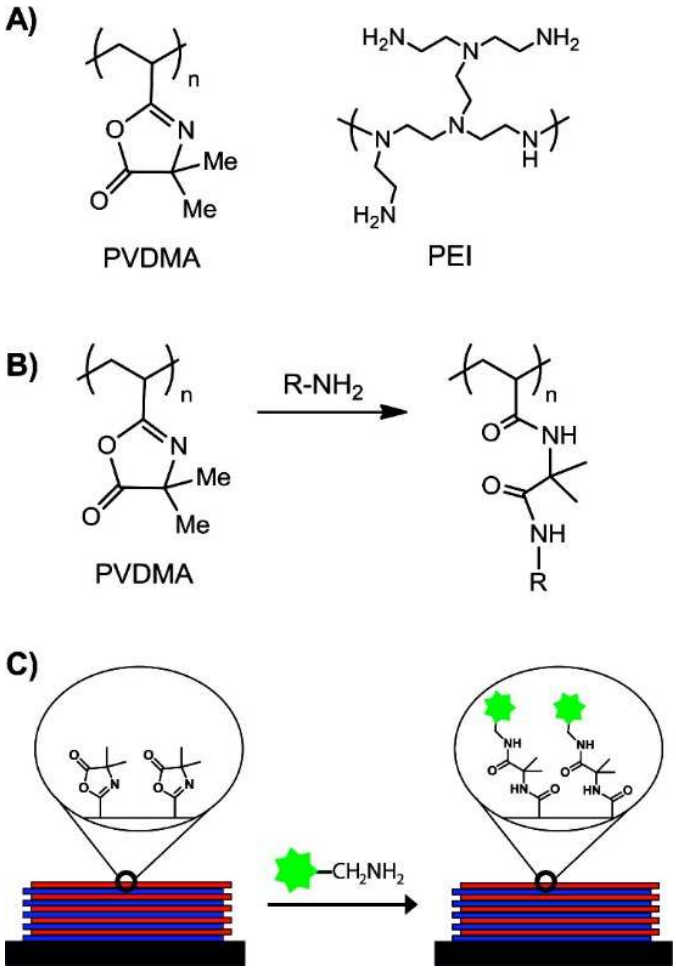

Figure 4.1: (A) Structures of branched poly(ethyleneimine) (PEI) and the azlactone-containing polymer poly(2-vinly-4,4-dimethyl azlactone)(PVMDA) used for the covalent/reactive assembly of the polymer multilayers in this study. (B) Reaction of the azlactone ring of PVDMA with primary amine functionality results in the formation of an amide/amide-type linkage. (C) Schematic showing functionalization of an azlactone-containing PEI/PVDMA film by post-fabrication treatment with a primary amine-containing nucleophile. Adapted from Broderick and Manna et al[16].

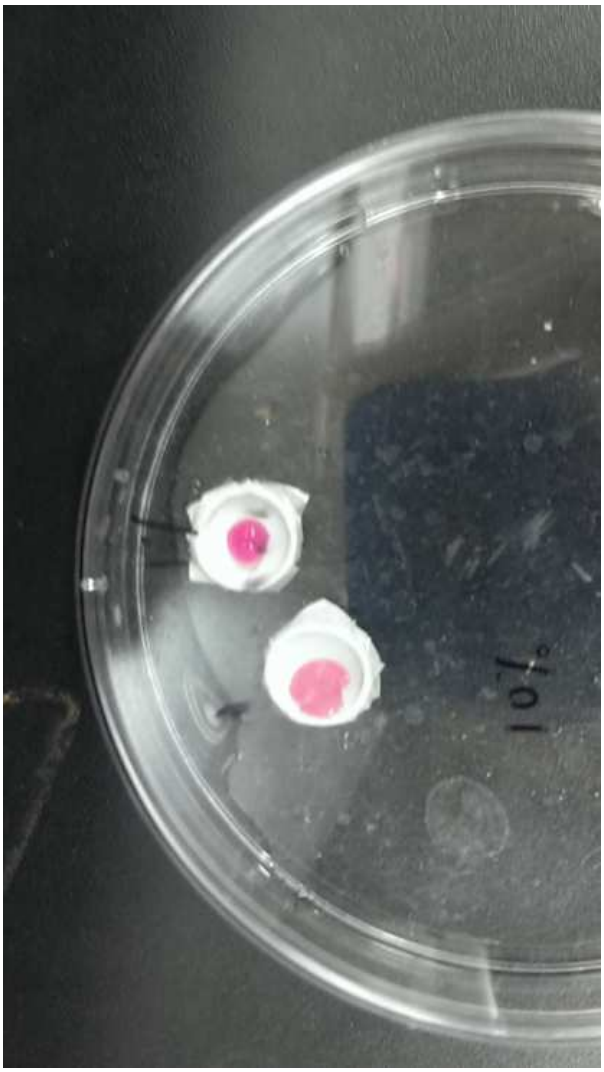

Figure 4.2: Droplets maintained for 24 hours at high humidity at 37 °C. Top droplet is DMEM + 1% FBS, while bottom droplet is DMEM + 10% FBS. The top droplet shows the spherical property expected from aqueous droplets on a superhydrophobic surface, while the bottom droplet shows degradation of the superhydrophobicity of the substrate

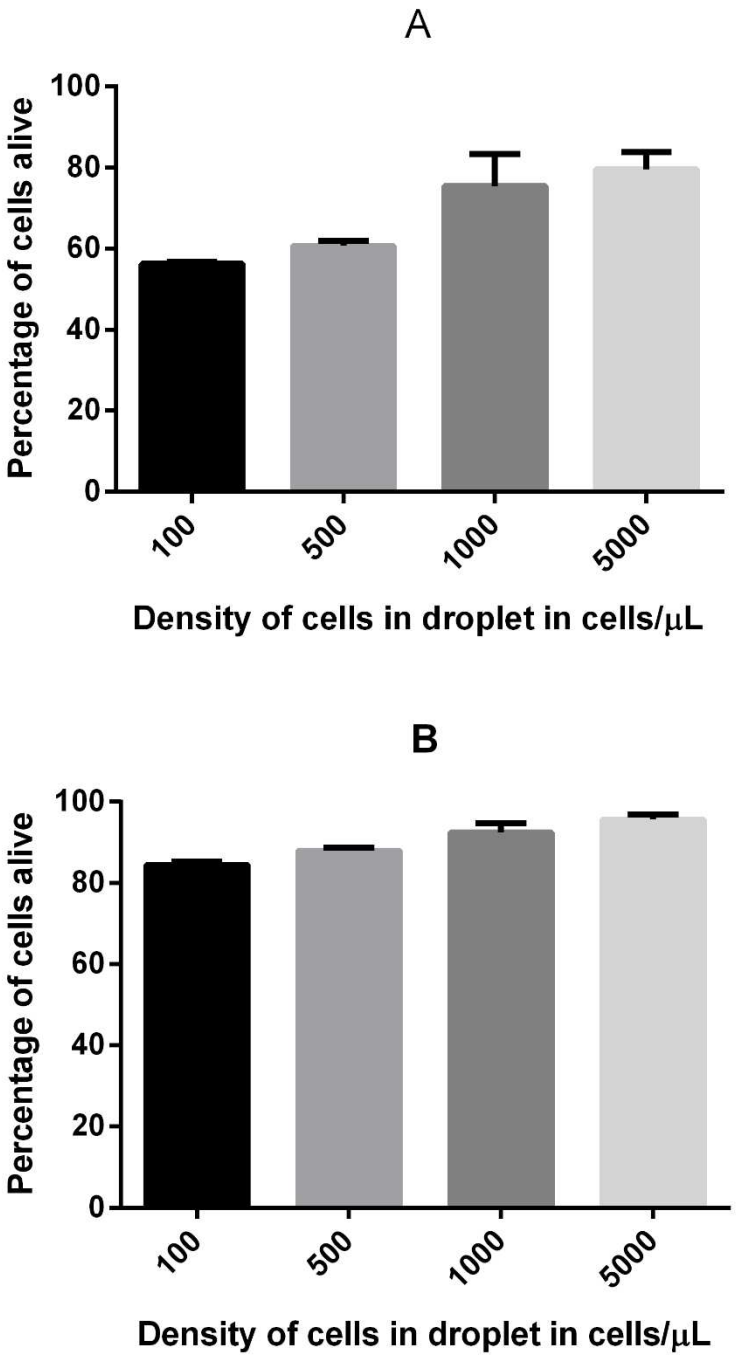

Figure 4.3: Bar graphs showing the viability of MCF-7 cells suspended on (A) superhydrophobic surfaces and (B) low attachment surfaces for 12 hours without shaking.

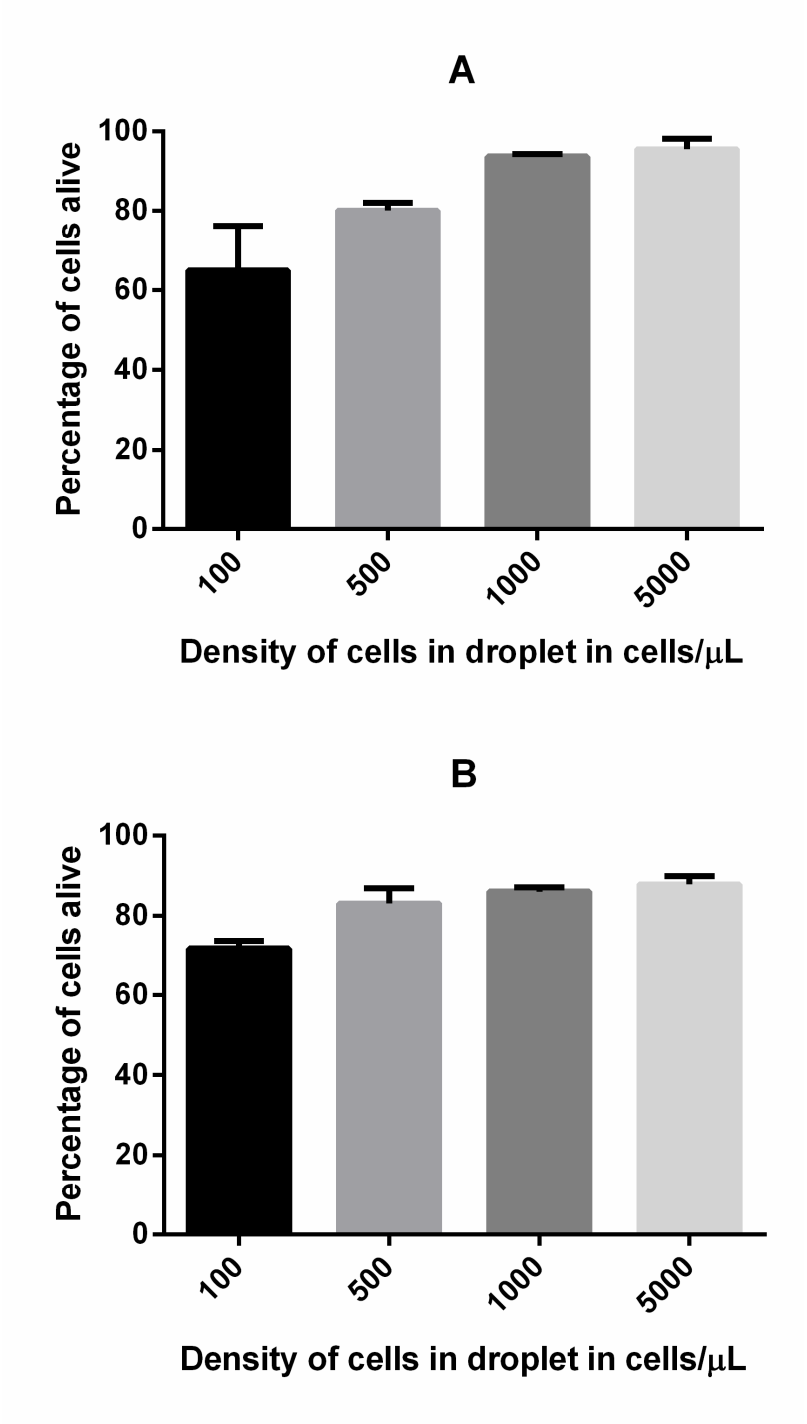

Figure 4.4: Bar graphs showing the viability of MCF-7 cells suspended on (A) superhydrophobic surfaces and (B) low attachment surfaces for 24 hours without shaking.

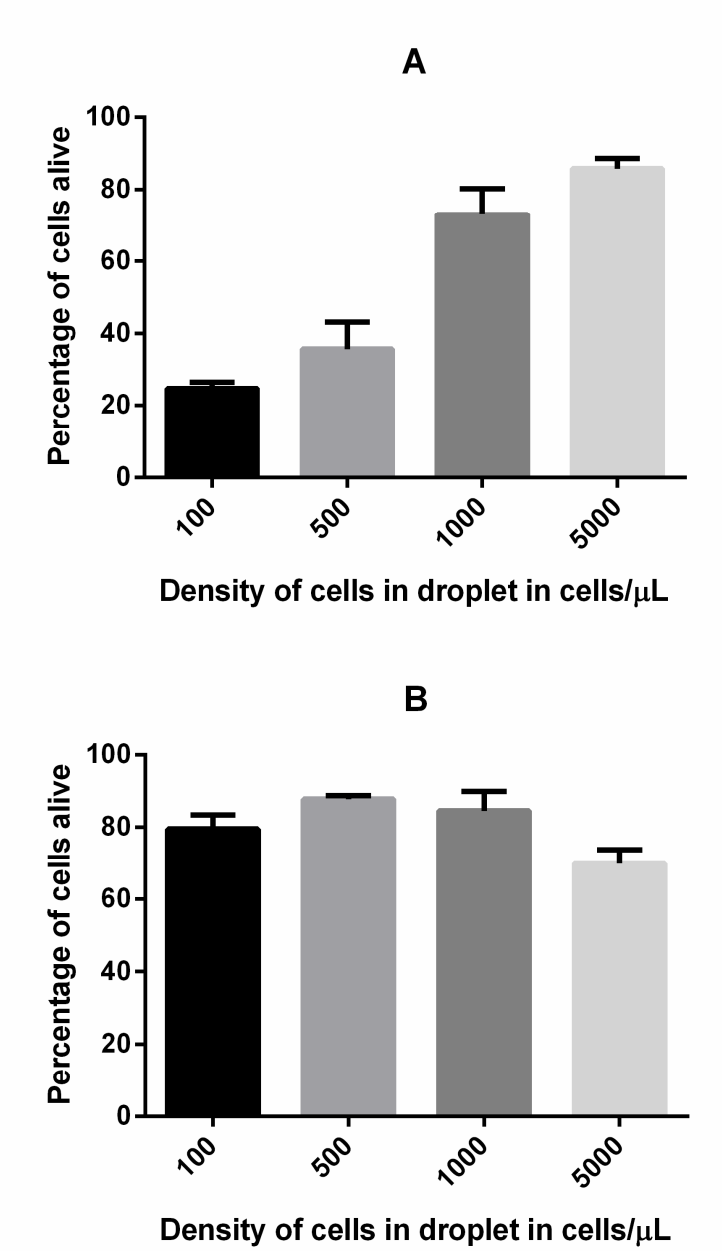

Figure 4.5: Bar graphs showing the viability of MCF-7 cells suspended on (A) superhydrophobic surfaces and (B) low attachment surfaces for 48 hours without shaking.

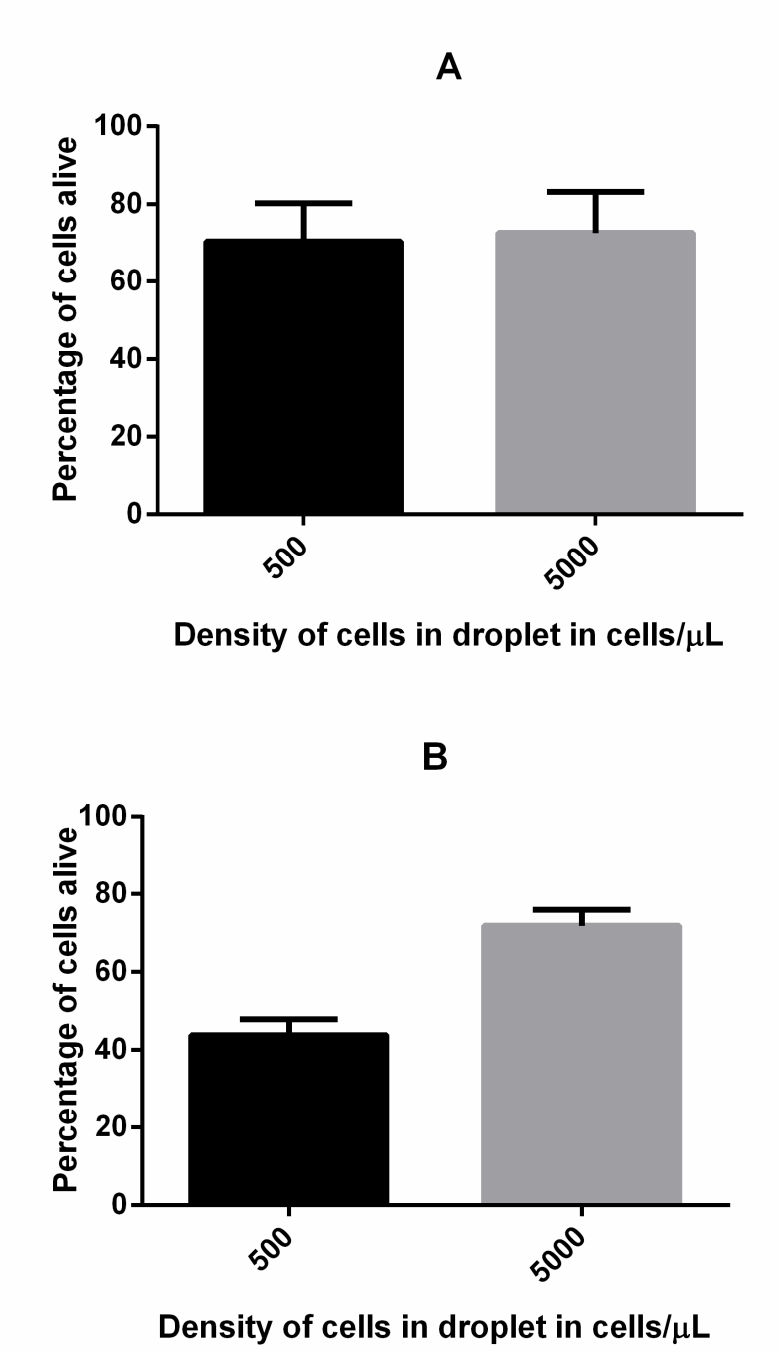

Figure 4.6: Bar graphs showing the viability of MCF-7 cells suspended on (A) superhydrophobic surfaces and (B) low attachment surfaces for 24 hours while being shaken at 130 rpm.

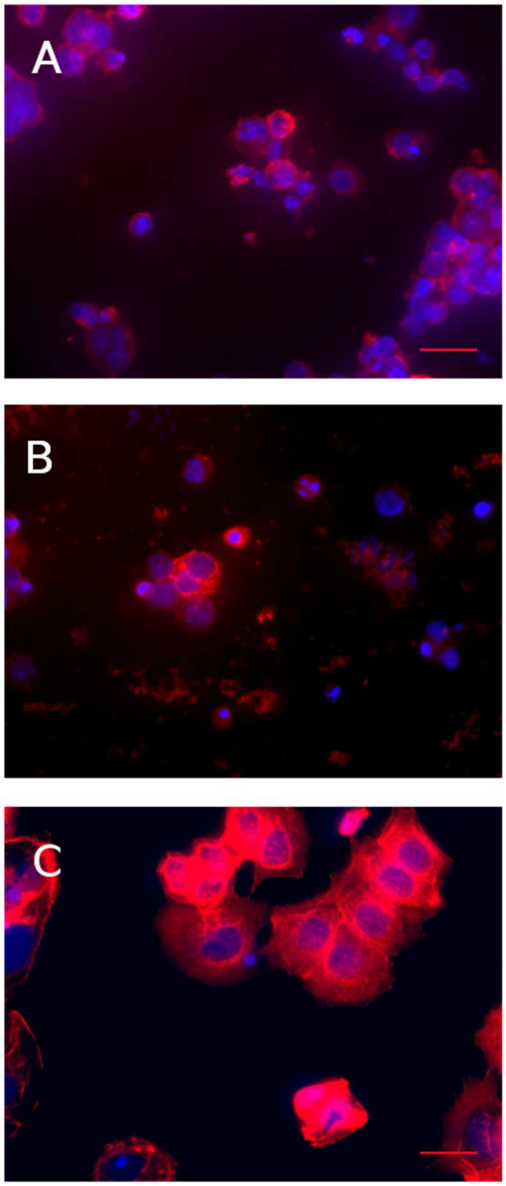

Figure 4.7: Phalloidin-Alexa 594 stained cells grown on (A) superhydrophobic surface and (B) low attachment surface for 24 hours, showing diffuse actin presentation and a lack of stress fibres. Cells in panel (C) were cultured on adherent tissue culture polystyrene and show distinct stress fibres and localized actin. Nuclei indicated in blue, phalloidin in red, scale bars are 50 µm

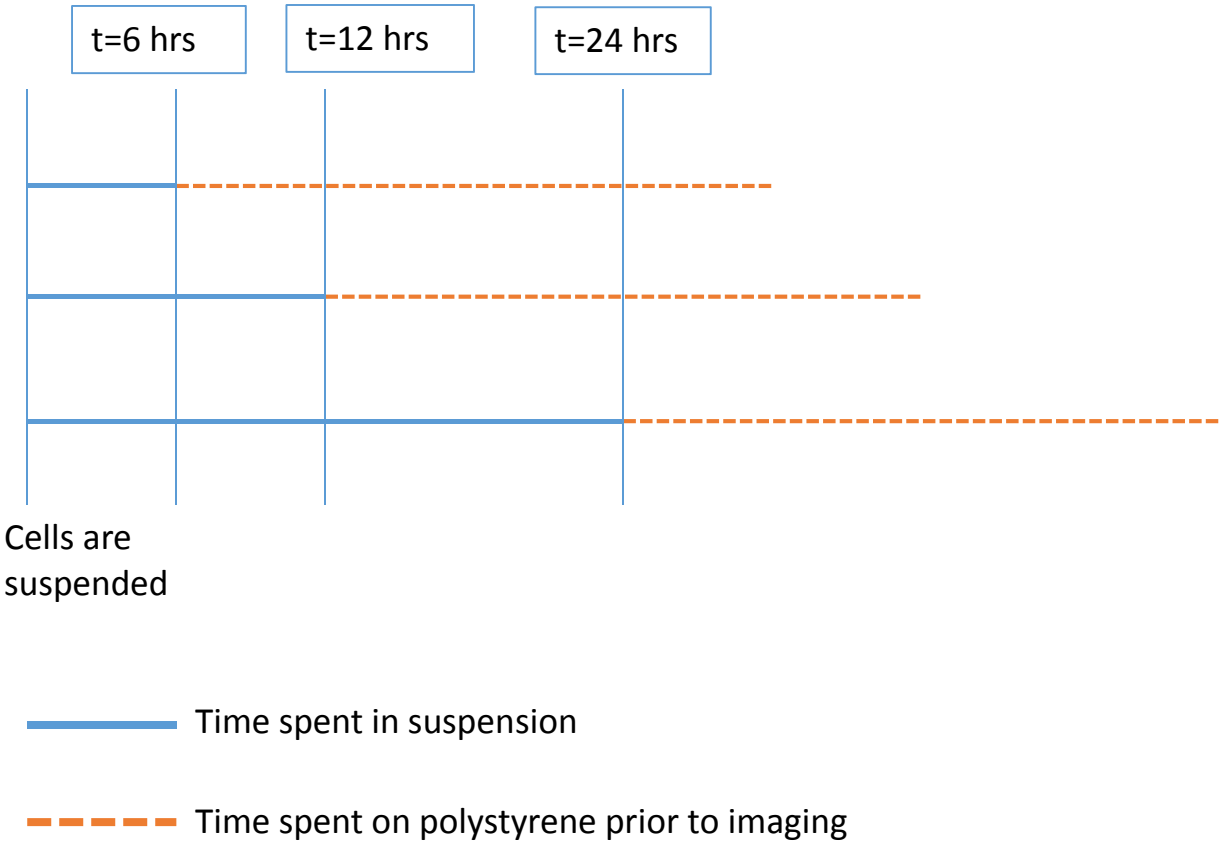

Figure 4.8: Schematic showing the setup of the replating experiments. Cells are maintained both on superhydrophobic surfaces and low attachment surfaces for 6, 12 or 24 hours, followed by replating onto polystyrene for 24 hours after which images are taken and replating characteristics are studied

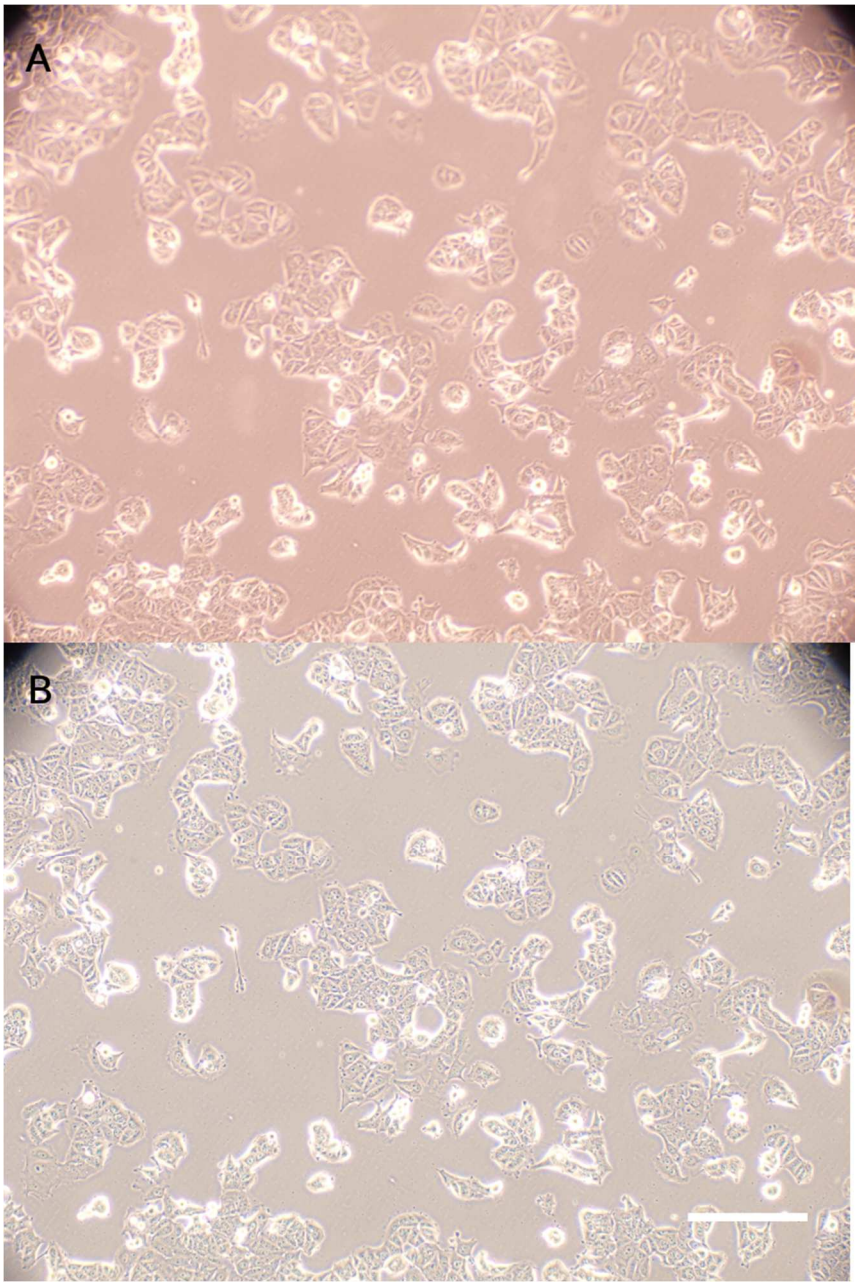

Figure 4.9: Images showing adherent cells after 24 hours of growth on polystyrene surfaces (A) before and (B) after removal of media showing the adherence of cells on the surface. Scale bar is 250 µm.

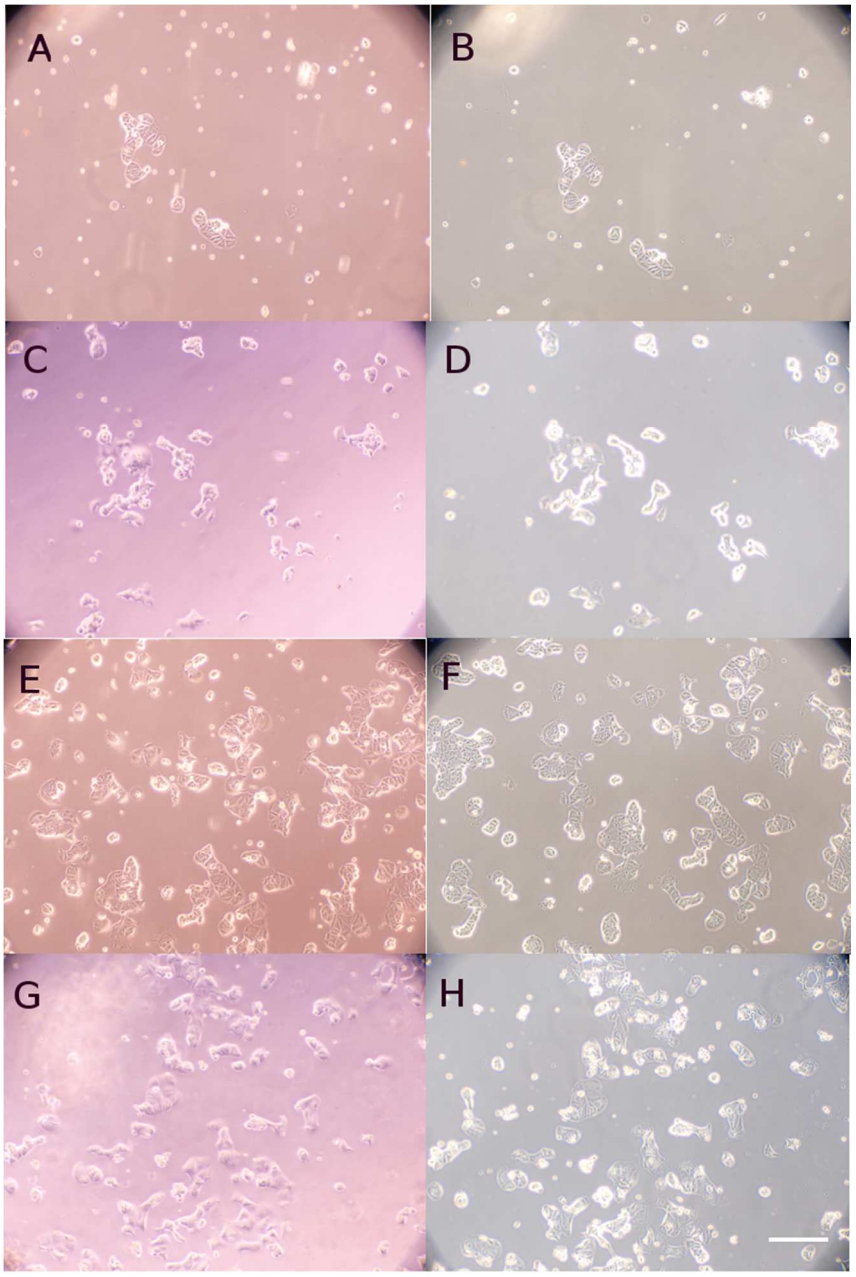

Figure 4.10: Images showing cells after 24 hours of culture on tissue culture polystyrene following 6 hours of treatment on superhydrophobic surfaces with shaking at 130 rpm with media (A) and (B) after media removal. (C) & (D) are on superhydrophobic surface without shaking, (E) & (F) are on low attachment surfaces with shaking at 130 rpm and (G) and (H) are on low attachment surfaces without shaking. Scale bar is 250 µm.

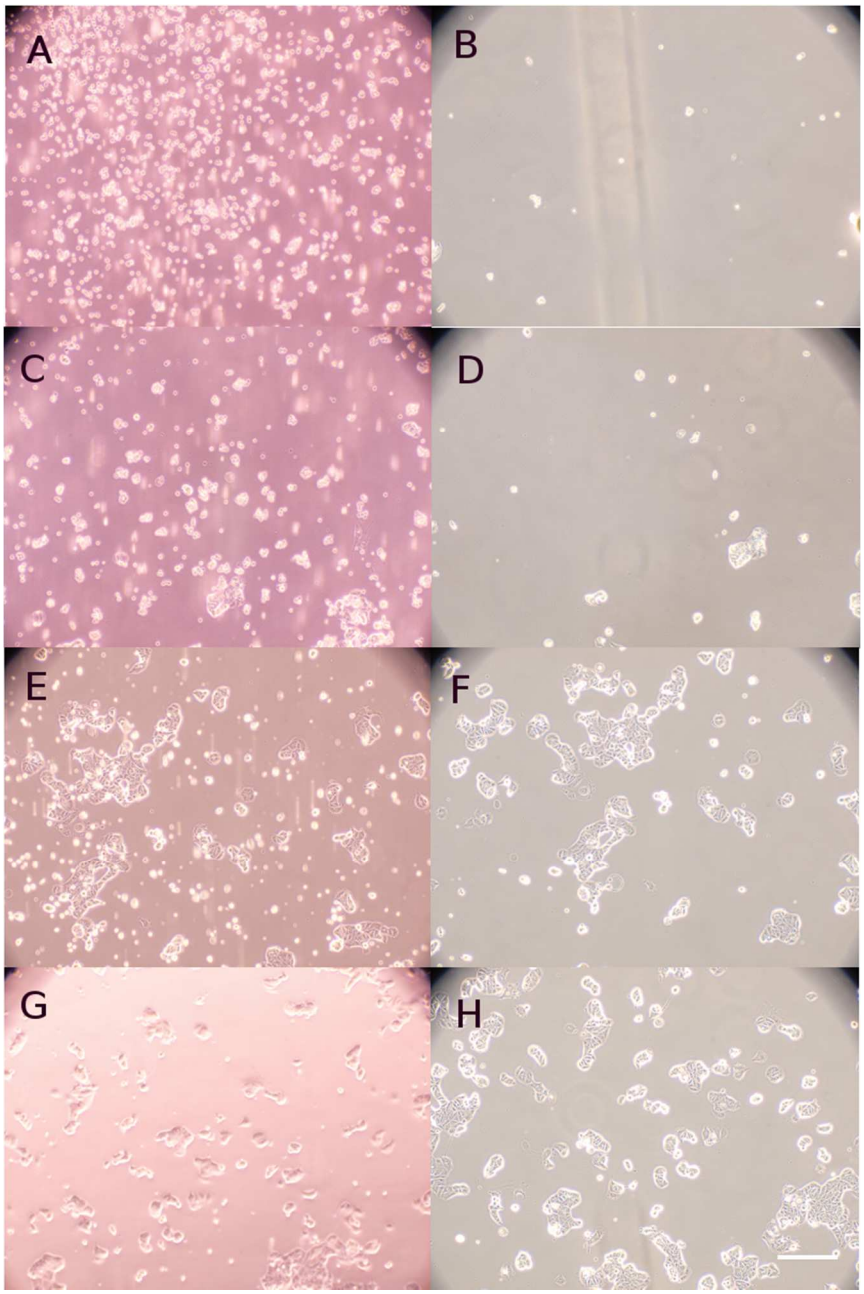

Figure 4.11: Images showing cells after 24 hours of culture on tissue culture polystyrene following 12 hours of treatment on superhydrophobic surfaces with shaking at 130 rpm with media (A) and (B) after media removal. (C) & (D) are on superhydrophobic surface without shaking, (E) & (F) are on low attachment surfaces with shaking at 130 rpm and (G) and (H) are on low attachment surfaces without shaking. Scale bar is 250 µm.

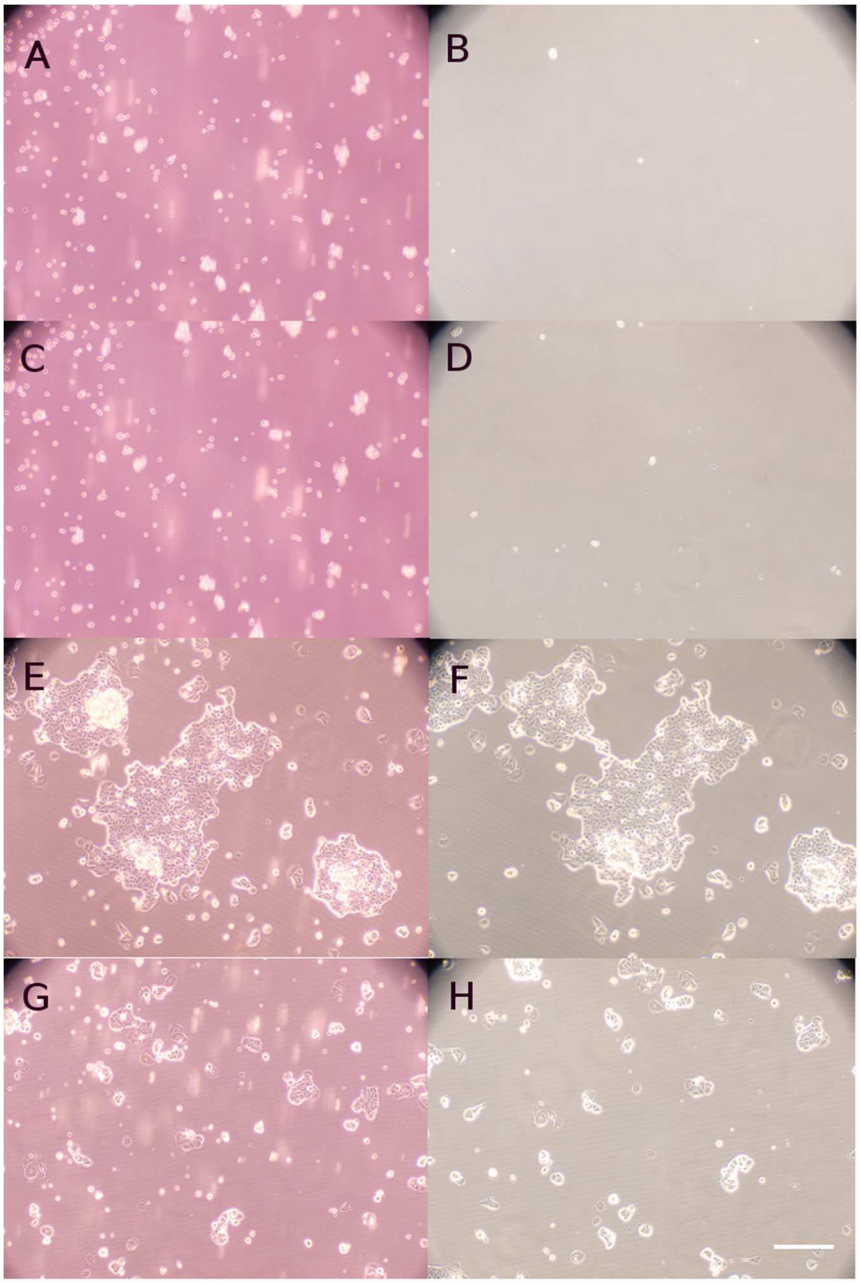

Figure 4.12: Images showing cells after 24 hours of culture on tissue culture polystyrene following 12 hours of treatment on superhydrophobic surfaces with shaking at 130 rpm with media (A) and (B) after media removal. (C) & (D) are on superhydrophobic surface without shaking, (E) & (F) are on low attachment surfaces with shaking at 130 rpm and (G) and (H) are on low attachment surfaces without shaking. Scale bar is 250 µm.

4.7 References

1. Clark P, Connolly P, Curtis ASG, Dow JAT, Wilkinson CDW. TOPOGRAPHICAL CONTROL OF CELL BEHAVIOR .1. SIMPLE STEP CUES. Development. 1987;99(3):439-48. PubMed PMID: WOS:A1987G384800014.

2. Curtis A, Wilkinson C. Topographical control of cells. Biomaterials. 1997;18(24):1573-83. doi: 10.1016/s0142-9612(97)00144-0. PubMed PMID: WOS:000073168100001.

3. Flemming RG, Murphy CJ, Abrams GA, Goodman SL, Nealey PF. Effects of synthetic micro- and nano-structured surfaces on cell behavior. Biomaterials. 1999;20(6):573-88. doi: 10.1016/s0142-9612(98)00209-9. PubMed PMID: WOS:000079177800009.

4. Carnegie JA, Cabaca O. EXTRACELLULAR-MATRIX COMPOSITION AND RESILIENCE - 2 PARAMETERS THAT INFLUENCE THE INVITRO MIGRATION AND MORPHOLOGY OF RAT INNER CELL MASS-DERIVED CELLS. Biology of Reproduction. 1993;48(2):287-99. doi: 10.1095/biolreprod48.2.287. PubMed PMID: WOS:A1993KG53800009.

5. Choquet D, Felsenfeld DP, Sheetz MP. Extracellular matrix rigidity causes strengthening of integrin-cytoskeleton linkages. Cell. 1997;88(1):39-48. doi: 10.1016/s0092-8674(00)81856-5. PubMed PMID: WOS:A1997WC56900007.

6. Yim EKF, Darling EM, Kulangara K, Guilak F, Leong KW. Nanotopography-induced changes in focal adhesions, cytoskeletal organization, and mechanical properties of human mesenchymal stem cells. Biomaterials. 2010;31(6):1299-306. doi: 10.1016/j.biomaterials.2009.10.037. PubMed PMID: WOS:000273985100032.

7. Li X-M, Reinhoudt D, Crego-Calama M. What do we need for a superhydrophobic surface? A review on the recent progress in the preparation of superhydrophobic surfaces. Chemical Society Reviews. 2007;36(8):1350-68. doi: 10.1039/b602486f. PubMed PMID: WOS:000247933900011.

8. Roach P, Shirtcliffe NJ, Newton MI. Progess in superhydrophobic surface development. Soft Matter. 2008;4(2):224-40. doi: 10.1039/b712575p. PubMed PMID: WOS:000252553600004.

9. Zhang X, Shi F, Niu J, Jiang Y, Wang Z. Superhydrophobic surfaces: from structural control to functional application. Journal of Materials Chemistry. 2008;18(6):621-33. doi: 10.1039/b711226b. PubMed PMID: WOS:000252831200002.

10. Nosonovsky M, Bhushan B. Superhydrophobic surfaces and emerging applications: Non-adhesion, energy, green engineering. Current Opinion in Colloid & Interface Science. 2009;14(4):270-80. doi: 10.1016/j.cocis.2009.05.004. PubMed PMID: WOS:000268353800006.

11. Crick CR, Parkin IP. Preparation and Characterisation of Super-Hydrophobic Surfaces. Chemistry-a European Journal. 2010;16(12):3568-88. doi: 10.1002/chem.200903335. PubMed PMID: WOS:000276327300001.

12. Shiu JY, Whang WT, Chen PL. Superhydrophobic Coatings for Microdevices. Journal of Adhesion Science and Technology. 2008;22(15):1883-91. doi: 10.1163/156856108x320032. PubMed PMID: WOS:000262393500006.

13. Buck ME, Schwartz SC, Lynn DM. Superhydrophobic Thin Films Fabricated by Reactive Layer-by-Layer Assembly of Azlactone-Functionalized Polymers. Chemistry of Materials. 2010;22(23):6319-27. doi: 10.1021/cm102115e. PubMed PMID: WOS:000284975100017.

14. Hammond PT. Form and function in multilayer assembly: New applications at the nanoscale. Advanced Materials. 2004;16(15):1271-93. doi: 10.1002/adma.200400760. PubMed PMID: WOS:000223696000004.

15. Manna U, Broderick AH, Lynn DM. Chemical Patterning and Physical Refinement of Reactive Superhydrophobic Surfaces. Advanced Materials. 2012;24(31):4291-+. doi: 10.1002/adma.201200903. PubMed PMID: WOS:000307163000009.

16. Broderick AH, Manna U, Lynn DM. Covalent Layer-by-Layer Assembly of Water-Permeable and Water-Impermeable Polymer Multilayers on Highly Water-Soluble and Water-Sensitive Substrates. Chemistry of Materials. 2012;24(10):1786-95. doi: 10.1021/cm300307g. PubMed PMID: WOS:000304237500011.

17. Buck ME, Zhang J, Lynn DM. Layer-by-layer assembly of reactive ultrathin films mediated by click-type reactions of poly(2-alkenyl azlactone)s. Advanced Materials. 2007;19(22):3951-+. doi: 10.1002/adma.200700822. PubMed PMID: WOS:000251383900035.

18. Busscher HJ, Stokroos I, Golverdingen JG, Schakenraad JM. ADHESION AND SPREADING OF HUMAN FIBROBLASTS ON SUPERHYDROPHOBIC FEP-TEFLON. Cells and Materials. 1991;1(3):243-9. PubMed PMID: WOS:A1991GK71300006.

19. Ishizaki T, Saito N, Takai O. Correlation of Cell Adhesive Behaviors on Superhydrophobic, Superhydrophilic, and Micropatterned Superhydrophobic/Superhydrophilic Surfaces to Their Surface Chemistry. Langmuir. 2010;26(11):8147-54. doi: 10.1021/la904447c. PubMed PMID: WOS:000277928100066.

20. Piret G, Galopin E, Coffinier Y, Boukherroub R, Legrand D, Slomianny C. Culture of mammalian cells on patterned superhydrophilic/superhydrophobic silicon nanowire arrays. Soft Matter. 2011;7(18):8642-9. doi: 10.1039/c1sm05838j. PubMed PMID: WOS:000294447600096.

21. Oliveira SM, Song WL, Alves NM, Mano JF. Chemical modification of bioinspired superhydrophobic polystyrene surfaces to control cell attachment/proliferation. Soft Matter. 2011;7(19):8932-41. doi: 10.1039/c1sm05943b. PubMed PMID: WOS:000295085700033.

22. Oliveira MB, Salgado CL, Song WL, Mano JF. Combinatorial On-Chip Study of Miniaturized 3D Porous Scaffolds Using a Patterned Superhydrophobic Platform. Small. 2013;9(5):768-78. doi: 10.1002/smll.201201436. PubMed PMID: WOS:000315769700018.

23. Oliveira MB, Neto AI, Correia CR, Rial-Hermida MI, Alvarez-Lorenzo C, Mano JF. Superhydrophobic Chips for Cell Spheroids High-Throughput Generation and Drug Screening. Acs Applied Materials & Interfaces. 2014;6(12):9488-95. doi: 10.1021/am5018607. PubMed PMID: WOS:000338184500070.

24. Salgado CL, Oliveira MB, Mano JF. Combinatorial cell-3D biomaterials cytocompatibility screening for tissue engineering using bioinspired superhydrophobic substrates. Integrative Biology. 2012;4(3):318-27. doi: 10.1039/c2ib00170e. PubMed PMID: WOS:000300827100009.

25. Ueda E, Geyer FL, Nedashkivska V, Levkin PA. Droplet Microarray: facile formation of arrays of microdroplets and hydrogel micropads for cell screening applications. Lab on a Chip. 2012;12(24):5218-24. doi: 10.1039/c2lc40921f. PubMed PMID: WOS:000311964700014.

26. Huang QL, Lin LX, Yang Y, Hu R, Vogler EA, Lin CJ. Role of trapped air in the formation of cell-and-protein micropatterns on superhydrophobic/superhydrophilic microtemplated surfaces. Biomaterials. 2012;33(33):8213-20. doi: 10.1016/j.biomaterials.2012.08.017. PubMed PMID: WOS:000310401000003.

27. Marcon L, Addad A, Coffinier Y, Boukherroub R. Cell micropatterning on superhydrophobic diamond nanowires. Acta Biomaterialia. 2013;9(1):4585-91. doi: 10.1016/j.actbio.2012.08.026. PubMed PMID: WOS:000313376900012.

28. Lin LX, Zheng DJ, Huang QL, Song R, Yang Y, Lin CJ. Construction of Transparent Superhydrophilic-Superhydrophobic Micropatterns for High-Throughput Living Cell Imaging. Science of Advanced Materials. 2013;5(5):494-8. doi: 10.1166/sam.2013.1479. PubMed PMID: WOS:000322604700009.

29. Ballester-Beltran J, Rico P, Moratal D, Song WL, Mano JF, Salmeron-Sanchez M. Role of superhydrophobicity in the biological activity of fibronectin at the cell-material interface. Soft Matter. 2011;7(22):10803-11. doi: 10.1039/c1sm06102j. PubMed PMID: WOS:000296388300039.

30. Loo CY, Young PM, Lee WH, Cavaliere R, Whitchurch CB, Rohanizadeh R. Superhydrophobic, nanotextured polyvinyl chloride films for delaying Pseudomonas aeruginosa attachment to intubation tubes and medical plastics. Acta Biomaterialia. 2012;8(5):1881-90. doi: 10.1016/j.actbio.2012.01.015. PubMed PMID: WOS:000302989700022.

31. Ishihara K, Nomura H, Mihara T, Kurita K, Iwasaki Y, Nakabayashi N. Why do phospholipid polymers reduce protein adsorption? Journal of Biomedical Materials Research. 1998;39(2):323-30. doi: 10.1002/(sici)1097-4636(199802)39:2<323::aid-jbm21>3.0.co;2-c. PubMed PMID: WOS:000071461400021.

32. Minett TW, Tighe BJ, Lydon MJ, Rees DA. REQUIREMENTS FOR CELL SPREADING ON POLYHEMA COATED CULTURE SUBSTRATES. Cell Biology International Reports. 1984;8(2):151-9. doi: 10.1016/0309-1651(84)90082-1. PubMed PMID: WOS:A1984SJ79300008.

33. Benzeev A, Farmer SR, Penman S. PROTEIN-SYNTHESIS REQUIRES CELL-SURFACE CONTACT WHILE NUCLEAR EVENTS RESPOND TO CELL-SHAPE IN ANCHORAGE-DEPENDENT FIBROBLASTS. Cell. 1980;21(2):365-72. doi: 10.1016/0092-8674(80)90473-0. PubMed PMID: WOS:A1980KF77000006.

34. Folkman J, Moscona A. ROLE OF CELL-SHAPE IN GROWTH-CONTROL. Nature. 1978;273(5661):345-9. doi: 10.1038/273345a0. PubMed PMID: WOS:A1978FA76400023.

35. Tian JF, Fu N, Chen XD, Shen W. Respirable liquid marble for the cultivation of microorganisms. Colloids and Surfaces B-Biointerfaces. 2013;106:187-90. doi: 10.1016/j.colsurfb.2013.01.016. PubMed PMID: WOS:000317441800027.

36. Song WL, Oliveira MB, Sher P, Gil S, Noobrega JM, Mano JF. Bioinspired methodology for preparing magnetic responsive chitosan beads to be integrated in a tubular bioreactor for biomedical applications. Biomedical Materials. 2013;8(4). doi: 10.1088/1748-6041/8/4/045008. PubMed PMID: WOS:000322167700011.

37. Sarvi F, Jain K, Arbatan T, Verma PJ, Hourigan K, Thompson MC, et al. Cardiogenesis of Embryonic Stem Cells with Liquid Marble Micro-Bioreactor. Advanced Healthcare Materials. 2015;4(1). doi: 10.1002/adhm.201400138. PubMed PMID: WOS:000347540100010.

38. Liu TQ, Winter M, Thierry B. Quasi-spherical microwells on superhydrophobic substrates for long term culture of multicellular spheroids and high throughput assays. Biomaterials. 2014;35(23):6060-8. doi: 10.1016/j.biomaterials.2014.04.047. PubMed PMID: WOS:000337212200008.

39. Seo J, Lee JS, Lee K, Kim D, Yang K, Shin S, et al. Switchable Water-Adhesive, Superhydrophobic Palladium-Layered Silicon Nanowires Potentiate the Angiogenic Efficacy of Human Stem Cell Spheroids. Advanced Materials. 2014;26(41):7043-+. doi: 10.1002/adma.201402273. PubMed PMID: WOS:000344782900006.

40. Mani SA, Guo W, Liao MJ, Eaton EN, Ayyanan A, Zhou AY, et al. The epithelial-mesenchymal transition generates cells with properties of stem cells. Cell. 2008;133(4):704-15. doi: 10.1016/j.cell.2008.03.027. PubMed PMID: WOS:000255903300024.

41. Kalluri R, Weinberg RA. The basics of epithelial-mesenchymal transition. Journal of Clinical Investigation. 2009;119(6):1420-8. doi: 10.1172/jci39104. PubMed PMID: WOS:000266601000006.

42. Lee JM, Dedhar S, Kalluri R, Thompson EW. The epithelial-mesenchymal transition: new insights in signaling, development, and disease. Journal of Cell Biology. 2006;172(7):973-81. doi: 10.1083/jcb.200601018. PubMed PMID: WOS:000236304600005.

43. Cano A, Perez-Moreno MA, Rodrigo I, Locascio A, Blanco MJ, del Barrio MG, et al. The transcription factor Snail controls epithelial-mesenchymal transitions by repressing E-cadherin expression. Nature Cell Biology. 2000;2(2):76-83. doi: 10.1038/35000025. PubMed PMID: WOS:000085148500011.

44. Tezcan O, Gunduz U. Vimentin silencing effect on invasive and migration characteristics of doxorubicin resistant MCF-7 cells. Biomedicine & Pharmacotherapy. 2014;68(3):357-64. doi: 10.1016/j.biopha.2014.01.006. PubMed PMID: WOS:000335395400015.

45. Schiller M, Javelaud D, Mauviel A. TGF-beta-induced SMAD signaling and gene regulation: consequences for extracellular matrix remodeling and wound healing. Journal of Dermatological Science. 2004;35(2):83-92. doi: 10.1016/j.jdermsci.2003.12.006. PubMed PMID: WOS:000223089600001.

5 Conclusions

5.1 Summary of findings

Human pluripotent stem cells represent a powerful tool for regenerative medicine. They can be differentiated into almost any cell type in the human body and have unlimited self-renewal capacity *in vitro*. Differentiating these cells is achieved through the recapitulation of protein signaling pathways that are activated through development. However, the use of hPSCs for regenerative medicine implies knowledge transfer from embryology and protein signaling studies (typically done in cancer cell lines) to hPSCs. The first project presented in the thesis used the differentiation capability of hPSCs to develop protein signaling insight and identified additional points of control of the Wnt signaling pathway.

Prior to this work, it was established that Wnt activation in hPSCs caused the mesodermal and endodermal differentiation of hPSCs. Canonical Wnt signaling, which occurs primarily through β-catenin, occurs through site-specific phosphorylation of β-catenin, which then determines if the β-catenin is available for signaling or for destruction. The studies focusing on hPSC differentiation on Wnt activation, however, did not investigate the state of β-catenin phosphorylation in differentiating hPSCs. This knowledge gap is filled with the work in this thesis. Through an investigation into the Wnt pathway in hPSCs, additional points of control of Wnt pathway were uncovered, and a new layout of the pathway was developed focused on the phosphorylation of β-catenin. Finally, a mathematical framework was laid out to model the Wnt pathway in hPSCs, and hopefully, with minimal modification, other systems as well.

It was established that treatment of hPSCs with GSK3 inhibitor CHIR caused the differentiation of hPSCs from a Nanog positive population to a Brachyury positive mesendodermal progenitor population in 50 hours. The differentiation principally occurred between 20 and 30 hours after the addition of CHIR. The differentiation was not stochastic in nature, all of the cells uniformly transitioned from one state to the other. Nanog was significantly reduced only 40 hours after CHIR addition. Total β-catenin levels did not significantly rise post CHIR addition. This was thought to be due to the high level of β-catenin normally present in confluent cells, and these experiments were performed near confluent densities.

However, phosphorylated β-catenin levels showed significant trends on CHIR addition. While cells initially showed low levels of GSK3β phosphorylated β-catenin (Phospho-β-catenin Ser33/Ser37/Thr41, tagged for ubiquitination and destruction by the proteosome), the levels of Phospho-β-catenin Ser33/Ser37/Thr41 rose significantly after 40 hours of treatment with DMSO. Adding CHIR caused no significant rise of this species up to 50 hours after CHIR addition, thereby indicating successful GSK3β inhibition. CK1α phosphorylated β-catenin (Phospho-β-catenin Thre41/Ser45, tagged for entry into the destruction complex) showed significant elevation 20 hours after the addition of CHIR. This was rationalized through the analysis of the equilibria of CK1α phosphorylation and GSK3β phosphorylation. Inhibition of GSK3β caused an accumulation of the reactant species for GSK3β phosphorylation, Phospho-β-catenin Thr41/Ser45. Transcriptionally active forms of β-catenin showed interesting dynamics as well.

PKA and Akt phosphorylated β-catenin, Phospho-β-catenin Ser552 showed a significant reduction from zero hour levels after 20 hours of CHIR addition. In contrast, PKA phosphorylated β-catenin

Phospho-β-catenin Ser675, showed a significant increase 20 hours after CHIR addition and remained significantly above baseline zero hour levels throughout the differentiation time. This spatial correlation was then related to the onset of Brachyury expression, which occurred 30 hours after CHIR addition. On immunostaining analysis, Brachyury and Phospho-β-catenin Ser675 were found to also be spatially colocalized, leading to the hypothesis that Phospho-β-catenin Ser675 is responsible for Brachyury expression.

The hypothesis was tested by treating cells with both CHIR and several PKA inhibitors. Western blotting demonstrated that treatment with both CHIR and PKA inhibition led to a reduction of Brachyury expression, and an absence of Brachyury with high doses of PKA inhibitors. The inhibition seemed to be dose dependent, however, this trend was not verified through the use of replicates. This inhibition of differentiation was verified through immunostaining.

These findings led to envisioning the Wnt pathway as a series of phosphorylation events and transcription events. The model layout proposed focused on the β-catenin phosphorylation events and allowed for multiple outcomes through Wnt signaling. The phosphorylation events were modeled as Michaelis Menten equilibria, cellular protein synthesis events were modeled as zero order reactions and protein destruction events were modeled as first order reactions. The mathematical layout can be parameterized to provide quantitative and qualitative insight into the pathway. While hPSCs served as a tool in this project to develop insight into the dynamics of β-catenin and the Wnt signaling pathway, hPSCs can also serve as a tool for the study of hard to isolate somatic tissues.

Vocal fold epithelia are a tightly packed stratified layer of cells that serve to act as a barrier to protect the vocal folds from chemical injury. However, the isolation of vocal fold epithelial tissue from animal cadavers for the study of barrier phenotypes remains challenging, and often precludes the study of active mechanisms of barrier maintenance due to the limited viability of *ex vivo* vocal fold epithelial tissue. Differentiation of this tissue *in vitro* could alleviate the limited viability problem.

Work done by the Palecek and Thibeault labs led to the development of a vocal fold epithelia differentiation protocol using a fibroblast embedded collagen gel scaffold for the plating and stratification of hPSC derived epithelial progenitors. However, this *in vitro* derived tissue could not be made confluent on a Transwell®® inserts for easy measurement of barrier characteristics. Work presented in this thesis developed a protocol for the differentiation of hPSCs to vocal fold epithelia on Transwell® inserts. Initial seeding density, insert material and insert porosity were optimized based on electrical barriers observed. Finally it was shown that the barrier formed had very low permeability (8.14 ± 1.95 nm/s) to Sodium Fluorescein. Previous studies used dextran to measure permeability, and dextran is much larger than Sodium Fluorescein. Therefore, tissues with limited permeability to Fluorescein will also be impermeable to dextran. Through the optimization of several parameters, a scalable system for the measurement of vocal fold epithelia barrier characteristics was developed.

Finally, chapter 4 of this thesis details a study done on the culture of cells on a superhydrophobic surface. Previous work had indicated that the micro and nano scale topology of the cell culture surface led to the changes in the behavior of the cells. However, no studies had demonstrated

these changes by growing cells within a droplet on a superhydrophobic surface. Previous studies had used superhydrophobicity to either create exclusion zones for cells, or for the creation of unique cell culture geometries. There had been no comparison between cells grown on a surface with a high contact angle and a standard contact angle. The standard contact angle control was a protein-resisting coating that prevented cells from attaching onto the surface. It was observed that at high densities cells remained viable on the superhydrophobic surface. They showed little cytoskeletal organization after 24 hours of incubation on the superhydrophobic surface, as expected. Treatment of the cells on the surface for longer than 12 hours led to the cells resisting plating back onto cell culture polystyrene on removal from the surface. Thus the culture of cells on a superhydrophobic surface led to phenotypic changes within the cells.

5.2 Future Recommendations

5.2.1 Wnt and Protein Kinase A interaction

This work established a platform for studying Wnt signaling through the inhibition of GSK3β and another kinase, PKA. The outcome of inhibiting both kinases indicated a possible role of PKA in aiding hPSC differentiation, which had previously not been discussed. However, Wnt activation causes phenotypes in many other systems, and in those, the PKA-Wnt relationship can be further explored through the qualitative and quantitative tools established in this work.

5.2.1.1 Colon cancer cell growth

Wnt is implicated in the proliferation of many cell types, notably colon cancer cell lines [1]. Several colon cancer cell lines express a truncated form of adenomatous polyposis coli (APC)

protein[2] which prevent the formation of the destruction complex, causing Wnt signaling to remain turned on constitutively; other cell lines like the SW480, lack the Ser45 residue[3], preventing entry into the destruction complex. Therefore in these cells there are mechanisms that act to permanently increase the levels of β-catenin.

In this work, we have shown that despite mechanisms (GSK3β) that increase β-catenin levels, through the inhibition of PKA, we could prevent standard Wnt activation outcomes in hPSCs. Similarly, PKA inhibitors could be tested out to see if they prevent the growth or limit the growth of colon cancers and colon cancer cell lines with β-catenin stabilization mutations. In these systems, it might even be possible that Akt inhibition could reduce Wnt activation outcomes. Through the use of a potent Akt inhibitor MK2206[4, 5], it could be possible to jointly agonize and antagonize the Wnt and PI3K pathways to observe effects on hPSCs or cancer cells without genetic alterations to these cells. These could lead to better therapeutic approaches for several cancer phenotypes in which either Wnt along with PKA or PI3K/Akt are involved. Finally, the process of epithelial to mesenchymal transition, critical in the progression of cancer [6] can be investigated using this framework.

One of the critical steps in the EMT process is the loss of E-cadherin expression and gain of N-cadherin expression[7, 8], often in concert with Wnt activation along with other pathways including PI3K. This work provides a mathematical tool for analyzing that interaction and possibly making *in silico* predictions that may be tested *in vitro*. In the model, Nanog represents the state of the cell when Wnt signaling is not activated, while, Brachyury represents the state of the cell after the activation of Wnt signaling. Substituting Nanog and Brachyury for E-cadherin and N-

cadherin would allow the model to be used on a wider variety of cell types. However, prior to the use of the model in a wider variety of cell types, it must be adequately parameterized.

5.2.1.2 Parameterization of the mathematical model

The current model is not adequately parameterized. The phosphorylated β-catenin data is too noisy to adequately decipher unique trends, possibly due to the high cellular density of the system being studied. It has been shown before that confluent cells have higher cytoplasmic and nuclear β-catenin than sub-confluent cells [9, 10]. Since the model can conceptually be used to analyze cancer cell phenotypes, perhaps these provide a better, slower growing alternative for the measurement of phosphorylated β-catenin levels. In addition, using a slower growing system (yet analyzing a time long enough for the establishment of Wnt dependent phenotypes, unlike previous Wnt modeling studies [11]) could lead to simpler modeling and the exclusion of density dependence on the model. However, some ideas may be tested for the inclusion of density dependence within the model framework.

Cell density directly affects the levels of the von Hippel-Lindau tumor suppressor protein (VHL) [12], a key component of the E3 ubiquitin ligase system [13] that destroys several proteins, including β-catenin within the cell. The interaction between Wnt and von Hippel-Lindau tumor suppressor protein has also been previously characterized [14], and shows the VHL gene as a downstream target of Wnt signaling. It has also been established that ubiquitination rates are higher in cells having lower quantities of VHL [15]. From these data, we can hypothesize that as the cells grow, the VHL protein is excluded from the nucleus. The cytoplasmic accumulation of the VHL protein product inhibits the action of the E3 ubiquitin ligase system, and therefore the

ubiquitination and destruction of β-catenin. The higher amounts of VHL translated as a downstream product of Wnt signaling would further reduce the ubiquitination rate as the cultures became dense. Mathematically, the rate of destruction of Phospho-β-catenin Ser33/Se37/Thr41 mathematical expression, shown in Equation 17, would be modified using a density dependent term, causing the rate of re4 to reduce as density increases, as shown in Equation 18. In addition density, ρ, would also be represented as a product of Wnt signaling the way Nanog and Brachyury are represented. These expressions would include the cell growth in the model, and prevent rapid equilibration of the model on the timescale of chemical kinase inhibition. The differentiation of hPSCs is a dynamic non-equilibrated system, and these expressions will reflect that and improve the current model.

5.2.1.3 Profiling of mouse and human pluripotent stem cell differences

Wnt activation has dramatically different effects on mouse embryonic stem cells [16] and human embryonic stem cells [17]. While CHIR is part of a combination of 3 enzyme inhibitors to keep mESCs pluripotent [16], it acts as a differentiating agent in hPSCs as demonstrated in this work. In both systems, PI3K-Akt signaling is implicated in the maintenance of pluripotency [18]. However, the role of PKA in undifferentiated cells is undefined.

It can be hypothesized that mESCs have lower levels of phosphorylated PKA than hESCs. Therefore, on the addition of CHIR, there is lesser PKA phoshphorylated β-catenin in the mESCs, and therefore lesser differentiation. However, as shown in this work, in hPSCs, the perhaps higher amounts of active phosphorylated PKA cause differentiation on CHIR addition. This hypothesis could be tested by activating PKA through the use of small molecule FMP-API-I[19] in mESCs.

Should this hypothesis remain valid, PKA activation in mESCs should induce similar behavior on Wnt activation and lead to differentiation, rather than pluripotency maintenance.

5.2.2 Vocal fold epithelia differentiation on Transwell® inserts

In this work, a scalable platform was created for the characterization of barrier phenotypes in vocal fold epithelial cells. The cells showed a stratified thickness less than *in vitro* tissue, but displayed several barrier phenotypes. The thickness of the tissue was perhaps related to the lack of collagen in the extracellular matrix that the tissue was grown on. Other works have also shown the importance of collagen in the formation of a stratified epithelial tissue [20]. Therefore, experiments may be attempted where collagen is added as an extracellular matrix layer on top of epithelial progenitors prior to stratification initiation. The strategy of sandwiching cells between extracellular matrix proteins has been performed before for other differentiation protocols [21], including a cardiac differentiation.

The true potential of this protocol lies in its scalability. The previous collagen gel embedded protocol could not be effectively scaled up or scaled down, and was constrained to be done in a 4.5 cm^2 format. However, the protocol detailed in this work was effectively scaled down from a 4.5 cm^2 format to a 1.12 cm^2 format, and can be scaled down further to smaller, higher throughput formats without much difficulty. This scale down has been performed successfully for other tissue such as hPSC derived blood brain barrier cells [22].

Scaling down the protocol allows for quantitative injury measurements, and the measurement of the chemical injury of vocal folds. An experiment could be set up assaying various concentrations of air pollutants diluted in cell culture media and exposed to the differentiated

tissue for a certain duration of time. Electrical resistance and permeability can be measured to estimate the extent of epithelial injury caused by the pollutant. While using a collagen-gel matrix tissue, the injury can only be inspected visually and the number of test conditions are limited by size (6 conditions in a standard cell culture plate). Using the system developed in this work, 24 – 48 conditions can be set up in a standard cell culture plate. In addition, non-visual injuries, such as the inactivation of active transport mechanisms can be measured using this system.

The histology of the tissue derived on inserts is challenging, however, the inserts are light permeable. Through limited testing, confocal visualization of immunostained proteins could perhaps be used to assay marker expression on the insert.

5.2.3 Cell culture on superhydrophobic surfaces

In this work, it was demonstrated that cells can survive in a droplet of media suspended on a superhydrophobic surface for up to 48 hours. It was further shown that treatment with the surface alters surface adherence phenotype of the cells cultured on the surface. The study can be improved through an investigation of the molecular mechanisms underlying these phenotypic changes. Both reverse-transcriptase polymerase chain reaction RT-PCR assays and further immunostaining of the cells can reveal key pathways being altered by the surface chemistry. The surface chemistry may also be improved through the testing of alternative functionalization to make the surface resistant to degradation by serum proteins or serum albumin. This would allow for the use of this surface in more biologically orientated experiments.

5.3 Conclusions

This work identified knowledge gaps in the process of Wnt induced hPSC differentiation and closed some of those gaps, discovering new points of control of the Wnt pathway and suggesting a new layout and mathematical framework for understanding the Wnt pathway. It identified the lack of a suitable system for the characterization of barrier phenotypes of vocal fold epithelia (one primary function of this tissue). A new system was developed for the derivation of this tissue type and the high barrier functionality of these cells was characterized. Finally, this work identified the lack of data for the effects of cell culture on a superhydrophobic surface and worked with a novel surface and demonstrated phenotypic changes induced by the surface. Therefore, three unique gaps of knowledge were identified and filled through the work presented in this thesis.

5.4 Equations

Equation 17: Equation for re4, the first order ubiquitination and destruction of Phospho-β-catenin Ser33/Ser37/Thr41, the species s11 represents Phospho-β-catenin Ser33/Ser37/Thr41

$$v_4 = k_4 * (s11)$$

Equation 18: Equation for re4, the first order ubiquitination and destruction of Phospho-β-catenin Ser33/Ser37/Thr41, the species s11 represents Phospho-β-catenin Ser33/Ser37/Thr41, modified by the density dependent term with $k_{4\rho}$ indicating the density dependent rate constant, and ρ and ρ_0 representing current and initial density respectively

$$v_4 = \frac{k_4 * (s11)}{1 + k_{4\rho} * (\rho - \rho_0)}$$

5.5 References

1. Klaus A, Birchmeier W. Wnt signalling and its impact on development and cancer. Nature Reviews Cancer. 2008;8(5):387-98. doi: 10.1038/nrc2389. PubMed PMID: WOS:000255264700018.

2. Cho K-H, Baek S, Sung M-H. Wnt pathway mutations selected by optimal beta-catenin signaling for tumorigenesis. Febs Letters. 2006;580(15):3665-70. doi: 10.1016/j.febslet.2006.05.053. PubMed PMID: WOS:000238691600015.

3. Harada N, Tamai Y, Ishikawa T, Sauer B, Takaku K, Oshima M, et al. Intestinal polyposis in mice with a dominant stable mutation of the beta-catenin gene. Embo Journal. 1999;18(21):5931-42. doi: 10.1093/emboj/18.21.5931. PubMed PMID: WOS:000083599900014.

4. Pal I, Mandal M. PI3K and Akt as molecular targets for cancer therapy: current clinical outcomes. Acta Pharmacologica Sinica. 2012;33(12):1441-58. doi: 10.1038/aps.2012.72. PubMed PMID: WOS:000312003500001.

5. Liu R, Liu D, Trink E, Bojdani E, Ning G, Xing M. The Akt-Specific Inhibitor MK2206 Selectively Inhibits Thyroid Cancer Cells Harboring Mutations That Can Activate the PI3K/Akt Pathway. Journal of Clinical Endocrinology & Metabolism. 2011;96(4):E577-E85. doi: 10.1210/jc.2010-2644. PubMed PMID: WOS:000289242800001.

6. Mani SA, Guo W, Liao MJ, Eaton EN, Ayyanan A, Zhou AY, et al. The epithelial-mesenchymal transition generates cells with properties of stem cells. Cell. 2008;133(4):704-15. doi: 10.1016/j.cell.2008.03.027. PubMed PMID: WOS:000255903300024.

7. Kalluri R, Weinberg RA. The basics of epithelial-mesenchymal transition. Journal of Clinical Investigation. 2009;119(6):1420-8. doi: 10.1172/jci39104. PubMed PMID: WOS:000266601000006.

8. Schmalhofer O, Brabletz S, Brabletz T. E-cadherin, beta-catenin, and ZEB1 in malignant progression of cancer. Cancer and Metastasis Reviews. 2009;28(1-2):151-66. doi: 10.1007/s10555-008-9179-y. PubMed PMID: WOS:000264476600013.

9. Steel MD, Puddicombe SM, Hamilton LM, Powell RM, Holloway JW, Holgate ST, et al. beta-Catenin/T-cell factor-mediated transcription is modulated by cell density in human bronchial epithelial cells. International Journal of Biochemistry & Cell Biology. 2005;37(6):1281-95. doi: 10.1016/j.biocel.2004.12.010. PubMed PMID: WOS:000228373300014.

10. Dietrich C, Scherwat J, Faust D, Oesch F. Subcellular localization of beta-catenin is regulated by cell density. Biochemical and Biophysical Research Communications. 2002;292(1):195-9. doi: 10.1006/bbrc.2002.6625. PubMed PMID: WOS:000174591900030.

11. Hernandez AR, Klein AM, Kirschner MW. Kinetic Responses of beta-Catenin Specify the Sites of Wnt Control. Science. 2012;338(6112):1337-40. doi: 10.1126/science.1228734. PubMed PMID: WOS:000311991200065.

12. Lee S, Chen DYT, Humphrey JS, Gnarra JR, Linehan WM, Klausner RD. Nuclear cytoplasmic localization of the von Hippel-Lindau tumor suppressor gene product is determined by cell

density. Proceedings of the National Academy of Sciences of the United States of America. 1996;93(5):1770-5. doi: 10.1073/pnas.93.5.1770. PubMed PMID: WOS:A1996TY96400007.

13. Jaakkola P, Mole DR, Tian YM, Wilson MI, Gielbert J, Gaskell SJ, et al. Targeting of HIF-alpha to the von Hippel-Lindau ubiquitylation complex by O-2-regulated prolyl hydroxylation. Science. 2001;292(5516):468-72. doi: 10.1126/science.1059796. PubMed PMID: WOS:000168187300036.

14. Giles RH, Lolkema MP, Snijckers CM, Belderbos M, van der Groep P, Mans DA, et al. Interplay between VHL/HIF1 alpha and Wnt/beta-catenin pathways during colorectal tumorigenesis. Oncogene. 2006;25(21):3065-70. doi: 10.1038/sj.onc.1209330. PubMed PMID: WOS:000237950800011.

15. Gorospe M, Egan JM, Zbar B, Lerman M, Geil L, Kuzmin I, et al. Protective function of von Hippel-Lindau protein against impaired protein processing in renal carcinoma cells. Molecular and Cellular Biology. 1999;19(2):1289-300. PubMed PMID: WOS:000078140900032.

16. Sato N, Meijer L, Skaltsounis L, Greengard P, Brivanlou AH. Maintenance of pluripotency in human and mouse embryonic stem cells through activation of Wnt signaling by a pharmacological GSK-3-specific inhibitor. Nature Medicine. 2004;10(1):55-63. doi: 10.1038/nm979. PubMed PMID: WOS:000187743600039.

17. Dravid G, Ye ZH, Hammond H, Chen GB, Pyle A, Donovan P, et al. Defining the role of Wnt/beta-catenin signaling in the survival, proliferation, and self-renewal of human embryonic stem cells. Stem Cells. 2005;23(10):1489-501. doi: 10.1634/stemcells.2005-0034. PubMed PMID: WOS:000233708700008.

18. Niwa H, Ogawa K, Shimosato D, Adachi K. A parallel circuit of LIF signalling pathways maintains pluripotency of mouse ES cells. Nature. 2009;460(7251):118-22. doi: 10.1038/nature08113. PubMed PMID: WOS:000267545200041.

19. Christian F, Szaszak M, Friedl S, Drewianka S, Lorenz D, Goncalves A, et al. Small Molecule AKAP-Protein Kinase A (PKA) Interaction Disruptors That Activate PKA Interfere with Compartmentalized cAMP Signaling in Cardiac Myocytes. Journal of Biological Chemistry. 2011;286(11):9079-96. doi: 10.1074/jbc.M110.160614. PubMed PMID: WOS:000288247700039.

20. Ling C, Raasch JL, Welham NV. E-Cadherin and Transglutaminase-1 Epithelial Barrier Restoration Precedes Type IV Collagen Basement Membrane Reconstruction following Vocal Fold Mucosal Injury. Cells Tissues Organs. 2011;193(3):158-69. doi: 10.1159/000318605. PubMed PMID: WOS:000287660900003.

21. Zhang J, Klos M, Wilson GF, Herman AM, Lian X, Raval KK, et al. Extracellular Matrix Promotes Highly Efficient Cardiac Differentiation of Human Pluripotent Stem Cells The Matrix Sandwich Method. Circulation Research. 2012;111(9):1125-U78. doi: 10.1161/circresaha.112.273144. PubMed PMID: WOS:000309961700007.

22. Wilson HK, Canfield SG, Hjortness MK, Palecek SP, Shusta EV. Exploring the effects of cell seeding density on the differentiation of human pluripotent stem cells to brain microvascular endothelial cells. Fluids and barriers of the CNS. 2015;12:13-. doi: 10.1186/s12987-015-0007-9. PubMed PMID: MEDLINE:25994964.